



## Cite as

Nano-Micro Lett.  
(2021) 13:143Received: 31 March 2021  
Accepted: 11 May 2021  
© The Author(s) 2021

# Applications of 2D-Layered Palladium Diselenide and Its van der Waals Heterostructures in Electronics and Optoelectronics

Yanhao Wang<sup>1</sup>, Jinbo Pang<sup>7</sup> ✉, Qilin Cheng<sup>7</sup>, Lin Han<sup>1</sup> ✉, Yufen Li<sup>7</sup>, Xue Meng<sup>1</sup>, Bergoi Ibarlucea<sup>12,13,14,15</sup>, Hongbin Zhao<sup>10</sup>, Feng Yang<sup>9</sup>, Haiyun Liu<sup>7</sup>, Hong Liu<sup>7,8</sup> ✉, Weijia Zhou<sup>7</sup>, Xiao Wang<sup>11</sup>, Mark H. Rummeli<sup>2,3,4,5,6</sup>, Yu Zhang<sup>1</sup> ✉, Gianarelio Cuniberti<sup>12,13,14,15</sup>

## HIGHLIGHTS

- The structure–property relationship of PdSe<sub>2</sub> is discussed, i.e., layer number vs. tunable bandgap, pentagonal structure vs. anisotropy-based polarized light detection.
- The synthesis approaches of PdSe<sub>2</sub> are thoroughly compared, including bottom-up methods such as chemical vapor transport for bulk crystals, chemical vapor deposition for thin films and single-crystal domains, selenization of Pd films. Besides, top-down strategies are discussed, covering the mechanical exfoliation of bulk crystals, plasma thinning, and vacuum annealing as well as phase transition.
- The emerging devices of PdSe<sub>2</sub> and its van der Waals heterostructures have been delivered such as metal/semiconductor contact, Schottky junction transistors, field-effect transistors, photodetectors, *p–n* junction-based rectifiers, polarized light detector, and infrared image sensors.
- Future opportunities of PdSe<sub>2</sub>-based van der Waals heterostructures are given including logic gate-based digital circuits, RF-integrated circuits, Internet of Things, and theoretical calculation as well as big data for materials science.

Yanhao Wang and Jinbo Pang contributed equally to this work.

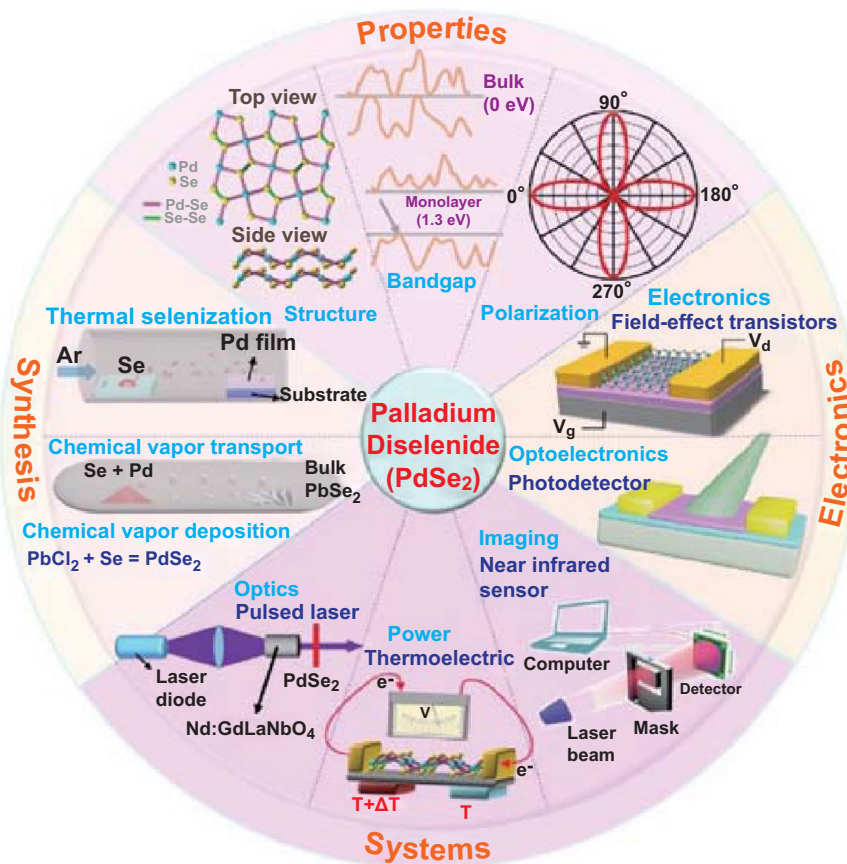
✉ Jinbo Pang, ifc\_pangjb@ujn.edu.cn; jinbo.pang@hotmail.com; Lin Han, hanlin@sdu.edu.cn; Hong Liu, hongliu@sdu.edu.cn; Yu Zhang, yuzhang@sdu.edu.cn

<sup>1</sup> Institute of Marine Science and Technology, Shandong University, Qingdao 266237, People's Republic of China<sup>2</sup> College of Energy Soochow Institute for Energy and Materials Innovations, Soochow University, Suzhou 215006, People's Republic of China<sup>3</sup> Key Laboratory of Advanced Carbon Materials and Wearable Energy Technologies of Jiangsu Province, Soochow University, Suzhou 215006, People's Republic of China<sup>4</sup> Centre of Polymer and Carbon Materials, Polish Academy of Sciences, M. Curie Skłodowskiej 34, 41-819 Zabrze, Poland<sup>5</sup> Institute for Complex Materials, IFW Dresden 20 Helmholtz Strasse, 01069 Dresden, Germany<sup>6</sup> Institute of Environmental Technology VŠB-Technical University of Ostrava, 17. listopadu 15, Ostrava 708 33, Czech Republic<sup>7</sup> Collaborative Innovation Center of Technology and Equipment for Biological Diagnosis and Therapy in Universities of Shandong, Institute for Advanced Interdisciplinary Research (iAIR), University of Jinan, Shandong, Jinan 250022, People's Republic of China<sup>8</sup> State Key Laboratory of Crystal Materials, Center of Bio and Micro/Nano Functional Materials, Shandong University, 27 Shandan Road, Jinan 250100, People's Republic of China<sup>9</sup> Department of Chemistry, Guangdong Provincial Key Laboratory of Catalytic Chemistry, Southern University of Science and Technology, Shenzhen, Guangdong 518055, People's Republic of China<sup>10</sup> State Key Laboratory of Advanced Materials for Smart Sensing, GRINM Group Co. Ltd., Xinwai Street 2, Beijing 100088, People's Republic of China<sup>11</sup> Shenzhen Institutes of Advanced Technology, Chinese Academy of Sciences, 1068 Xueyuan Avenue, Shenzhen University Town, Shenzhen 518055, People's Republic of China<sup>12</sup> Institute for Materials Science and Max Bergmann Center of Biomaterials, Technische Universität Dresden, 01069 Dresden, Germany<sup>13</sup> Center for Advancing Electronics Dresden, Technische Universität Dresden, 01069 Dresden, Germany<sup>14</sup> Dresden Center for Computational Materials Science, Technische Universität Dresden, 01062 Dresden, Germany<sup>15</sup> Dresden Center for Intelligent Materials (GCL DCIM), Technische Universität Dresden, 01062 Dresden, Germany

Published online: 14 June 2021



**ABSTRACT** The rapid development of two-dimensional (2D) transition-metal dichalcogenides has been possible owing to their special structures and remarkable properties. In particular, palladium diselenide ( $\text{PdSe}_2$ ) with a novel pentagonal structure and unique physical characteristics have recently attracted extensive research interest. Consequently, tremendous research progress has been achieved regarding the physics, chemistry, and electronics of  $\text{PdSe}_2$ . Accordingly, in this review, we recapitulate and summarize the most recent research on  $\text{PdSe}_2$ , including its structure, properties, synthesis, and applications. First, a mechanical exfoliation method to obtain  $\text{PdSe}_2$  nanosheets is introduced, and large-area synthesis strategies are explained with respect to chemical vapor deposition and metal selenization. Next, the electronic and optoelectronic properties of  $\text{PdSe}_2$  and related heterostructures, such as field-effect transistors, photodetectors, sensors, and thermoelectric devices, are discussed. Subsequently, the integration of systems into infrared image sensors on the basis of  $\text{PdSe}_2$  van der Waals heterostructures is explored. Finally, future opportunities are highlighted to serve as a general guide for physicists, chemists, materials scientists, and engineers. Therefore, this comprehensive review may shed light on the research conducted by the 2D material community.



**KEYWORDS** Palladium diselenide; nTMDC; Synthesis; Field-effect transistors; Photodetectors; Sensors

## 1 Introduction

Significant research has been conducted on two-dimensional (2D) materials, including conductors (graphene) [1], semiconductors ( $\text{MoS}_2$ ), superconductors ( $\text{NbSe}_2$ ), and insulators (h-BN). The family of 2D-layered materials, possessing unique structures and extraordinary physical and chemical properties, has been continuously expanded with the addition of members such as transition-metal dichalcogenides (TMDCs) [2], phosphorene, borophene, and MXenes. These 2D materials have been widely employed in biomedical engineering [3], electronics and optoelectronics, photonics, optics, and related devices. Besides, 2D materials have boosted the field of smart sensing such as gas sensors [4].

They exhibit significant potential in devices such as photo-detectors and photovoltaic cells; this is attributed to their distinct resonance absorption in the visible to near-infrared spectrum.

The family of TMDCs is an important component of 2D materials with a general formula of  $\text{MX}_2$ , where M is a transition element and X is a chalcogen element. According to the International Union of Pure and Applied Chemistry (IUPAC) [5], transition elements generally comprise those from group 3 to group 12. TMDCs exhibit remarkable properties such as tunable bandgap, stability in air, and good charge transport, which is of great significance to the development of modern technology. Currently, more commonly discussed TMDCs are group-6 TMDCs [6], which

primarily include MoS<sub>2</sub>, MoSe<sub>2</sub>, MoTe<sub>2</sub>, WS<sub>2</sub>, WSe<sub>2</sub>, and WTe<sub>2</sub>. Recently, 2D TMDCs and their heterojunction have attracted more and more research interest in the field of broadband photodetectors due to their excellent electronic and optoelectronic properties and show broadband photodetection from UV to IR [7]. In fact, TMDCs have retained significant research value for fundamental physics and device applications.

### 1.1 Emerging Noble Transition-Metal Dichalcogenides

Dichalcogenides of group-10 transition metals MX<sub>2</sub> (M = Pd, Pt, X = S, Se, Te) have recently received increased research attention owing to their novel properties. They are often referred to as noble transition-metal dichalcogenides (nTMDCs) because all the metal elements in group 10 are noble metals [8]. Here, nTMDCs [9] primarily refer to PtS<sub>2</sub>, PdS<sub>2</sub>, PtSe<sub>2</sub>, and PdSe<sub>2</sub>, and they show a significant intrinsic nature resulting from rich *d*-electron content. Besides,

PtTe<sub>2</sub>-based photodetectors demonstrate an air stable and high performance in MIR photodetection up to 10.6 μm [10].

The fundamental properties of the selected nTMDCs are listed in Table 1. The nTMDCs are, however, yet to be fully understood; therefore, there is much scope for research in this area.

Before introducing the PdSe<sub>2</sub>, we first look at the properties of other nTMDCs. PtS<sub>2</sub> exhibits very strong inter-layer interactions and layer-dependent indirect bandgaps ranging from 1.6 (monolayer) to 0.25 (bulk) eV. In recent years, few-layer PtS<sub>2</sub> has become a promising material for field-effect transistors (FETs) with high mobility and on/off ratios. Furthermore, PtS<sub>2</sub>-based devices have demonstrated excellent performance with respect to photodetection and sensing. Similarly, 2D PtSe<sub>2</sub> shows prominent layer-dependent properties, and the bandgap of monolayer PtSe<sub>2</sub> is 1.2 eV, while that of bulk PtSe<sub>2</sub> is zero. The carrier mobility of few-layer PtSe<sub>2</sub> can theoretically exceed 10<sup>3</sup> cm<sup>2</sup> V<sup>-1</sup> s<sup>-1</sup>, and very high stability in air is demonstrated [11]. Few-layered PtSe<sub>2</sub> has been utilized in a

**Table 1** The basic properties of the noble transition-metal dichalcogenides group

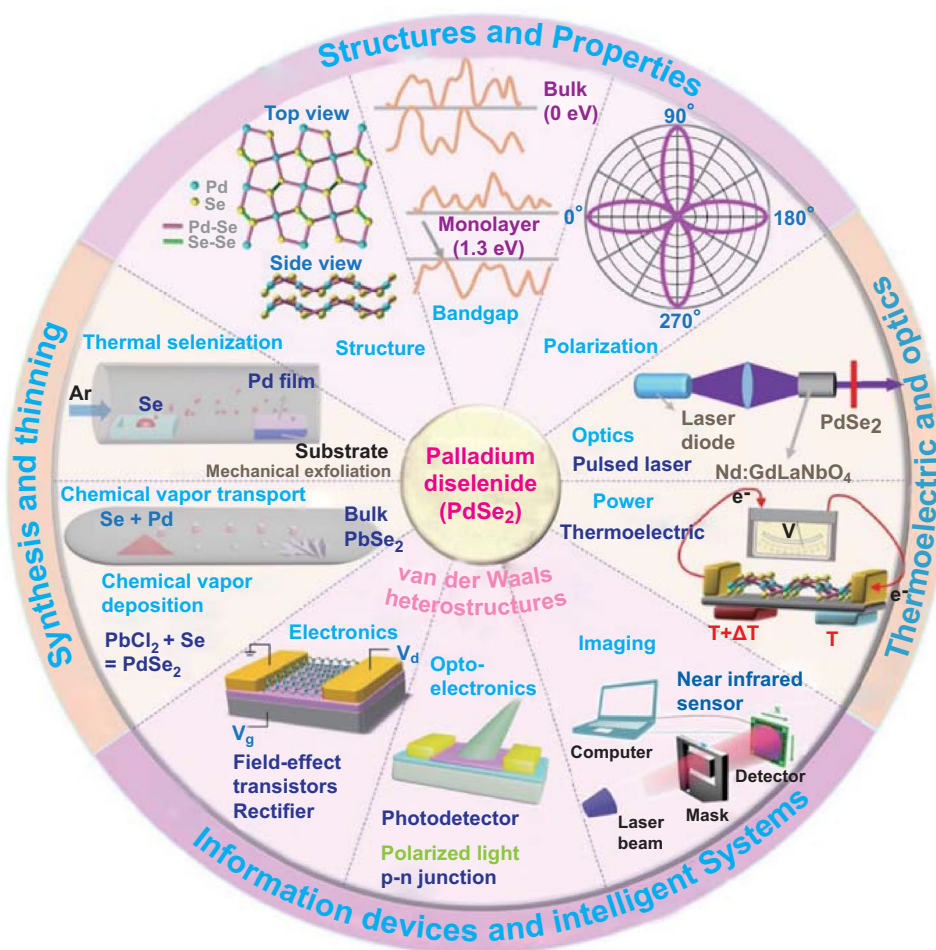
Material types	Phase	Bandgap	Lattice parameters	Lattice structure	Crystal system	Space group	References
PdSe <sub>2</sub>	Marcasite	0 eV (bulk) 1.33 eV (1L)	<i>a</i> = 5.74 Å; <i>b</i> = 5.92 Å; <i>c</i> = 7.69 Å	Pentagonal	Orthorhombic	Pbca [61]	[35]
PdSe <sub>2</sub>	Marcasite		<i>a</i> = 5.79 Å; <i>b</i> = 5.95 Å; <i>c</i> = 8.59 Å	Pentagonal	Orthorhombic	Pbca [61]	[132]
PdSe <sub>2</sub>	1 T	0 eV (≥ 2L) 0.778 eV (1L)	<i>a</i> = 3.73 Å; <i>b</i> = 4.79 Å	n.a	Hexagonal		[133]
PdSe <sub>2</sub>	2H	n.a	<i>a</i> = 3.58 Å; <i>c</i> = 10.90 Å	n.a	Hexagonal		[133]
PdSe <sub>2</sub>	Pyrite	n.a	<i>a</i> = 5.74 Å; <i>b</i> = 5.86 Å; <i>c</i> = 7.53 Å	n.a	Orthorhombic		[133]
PdSe <sub>2</sub>	Marcasite	n.a	<i>a</i> = 5.06 Å; <i>b</i> = 6.12 Å; <i>c</i> = 3.89 Å	n.a	Orthorhombic		[133]
PdS <sub>2</sub>	Marcasite		<i>a</i> = 5.50 Å; <i>b</i> = 5.59 Å; <i>c</i> = 8.61 Å	pentagonal	Orthorhombic	Pbca [61]	[134]
PdS <sub>2</sub>	1 T	0 eV (≥ 2L) 1.1 eV (1L)	<i>a</i> = 3.068 Å	n.a	Hexagonal	Pbca [61]	[14]
PdS <sub>2</sub>	2H	n.a	<i>a</i> = 3.82 Å; <i>c</i> = 9.33 Å	n.a	Hexagonal	n.a	[133]
PdS <sub>2</sub>	Pyrite	0 eV (Bulk) 1.399 eV (1L)	<i>a</i> = 5.45 Å; <i>b</i> = 5.53 Å; <i>c</i> = 7.20 Å	n.a	Orthorhombic	n.a	[133]
PdS <sub>2</sub>	Marcasite	n.a	<i>a</i> = 4.78 Å; <i>b</i> = 5.67 Å; <i>c</i> = 3.79 Å	n.a	Orthorhombic	n.a	[133]
PdTe <sub>2</sub>	Merenskyite	n.a	n.a	n.a	Trigonal	P-3m1 [164]	[135]
PdTe <sub>2</sub>	1 T	n.a	<i>a</i> = <i>b</i> = 4.0365 Å; <i>c</i> = 5.1262 Å	n.a	Hexagonal		[136]
PdTe <sub>2</sub>	2H	n.a	<i>a</i> = 3.83 Å; <i>c</i> = 11.60 Å	n.a	Hexagonal		[133]
PdTe <sub>2</sub>	Pyrite	0 eV (≥ 1L)	<i>a</i> = <i>b</i> = <i>c</i> = 6.54 Å	n.a	Orthorhombic		[133]
PdTe <sub>2</sub>	Marcasite	n.a	<i>a</i> = 5.40 Å; <i>b</i> = 6.65 Å; <i>c</i> = 4.10 Å	n.a	Orthorhombic		[133]
PtSe <sub>2</sub>	1 T	0 eV (bulk) 1.17 eV (1L)	<i>a</i> = <i>b</i> = 3.73 Å; <i>c</i> = 5.08 Å	Octahedral crystal	Hexagonal		[11]
PtS <sub>2</sub>	1 T	0.25 eV (bulk) 1.6 eV (1L)	<i>a</i> = <i>b</i> = 3.54 Å; <i>c</i> = 5.04 Å	Octahedral coordination structure	Hexagonal		[30]

variety of applications, such as FETs and photodetectors.  $\text{PtSe}_2$  shows good potential in piezoelectric devices, saturable absorbers, and electrochemical energy conversion. The structure of  $\text{PdS}_2$  comprises a pentagonal network, which includes two Pd atoms and three S atoms distributed on the atomic plane [12]. Monolayer  $\text{PdS}_2$  has two stable structures: one is a standard 1 T structure and the other involves a bulk-like geometry [13]. Through predictions and calculations, monolayer  $\text{PdS}_2$  has been determined to possess a semiconducting feature with a bandgap of approximately 1.1 eV, while bilayer  $\text{PdS}_2$  possesses a semimetallic feature [14]. Through first-principle calculations, a few-layer  $\text{PdS}_2$  has been predicted theoretically with good electronic and optoelectronic properties. However, few experimental synthesis studies have been reported in this regard. Thus far, there remain good opportunities for the material optimization and device applications of

$\text{PdS}_2$ . But  $\text{PdS}_2$  pentagonal structure is not thermodynamically stable, which limits its applications. Hence,  $\text{PdSe}_2$  becomes of importance for exploiting the polarization properties and related optoelectronic applications.

## 1.2 Importance of $\text{PdSe}_2$

$\text{PdSe}_2$  exhibits unique physical properties such as high carrier mobility, tunable bandgaps, and magnetic transport.  $\text{PdSe}_2$  has become a popular 2D material owing to its good stability [15], layer-dependent bandgap, and in-plane optical anisotropy [16].  $\text{PdSe}_2$  (Scheme 1) has been integrated into electronic [17], thermoelectric, optical [18], and optoelectronic devices [19]. The diverse polymorphisms of  $\text{PdSe}_2$  provide the platform for investigating the topological states and the applications of quantum information devices [20].



**Scheme 1**  $\text{PdSe}_2$  and its heterostructures for electronic, optic, and optoelectronic devices and systems

PdSe<sub>2</sub>-based van der Waals heterostructures (vdWHs) have been widely incorporated in current rectifier, polarized light photodetector, and infrared image sensor applications. First, the direct synthesis of PdSe<sub>2</sub>-based vdWHs has been investigated via deposition of PdSe<sub>2</sub> over other 2D materials such as graphene [21], MoS<sub>2</sub> [22], MoSe<sub>2</sub> [23], GeSe [24], and SnSe<sub>2</sub>. The stacking with arrayed nanomaterials gives rise to heterostructure devices such as ZnO nanorods and Si nanowires [25]. A perovskite [26] heterostructure can be formed with PdSe<sub>2</sub> using a self-powered image sensor.

In this review, we discuss the most recent developments with regard to PdSe<sub>2</sub> and its vdWHs, including approaches for its synthesis and its application in electronics, optoelectronics, and optics. We believe that this comprehensive contribution may attract the attention of research communities as well as industrial engineers interested in PdSe<sub>2</sub> material development and device integration.

## 2 Structure and Properties of PdSe<sub>2</sub>

This section introduces in detail the crystalline structure, electronic structure, energy band, vibrational phonon modes, and phase transition of PdSe<sub>2</sub>, which are the bases of its application in various fields.

### 2.1 Crystal Structure

As a 2D-puckered pentagonal material, PdSe<sub>2</sub> possesses orthorhombic lattices and a low symmetry, and it was identified as the first TMDC with a pentagonal structure [27]. The crystalline structure of PdSe<sub>2</sub> has been studied from as early as 1952 [28], owing to which a good foundation for current research has been laid. Most recently, 2D materials with pentagonal structures have attracted much research attention. Examples include penta-graphene, penta-PdS<sub>2</sub> [12], penta-SnS<sub>2</sub>, penta-silicene, and penta-germanene. The structures of these pentagonal materials differ from most hexagonal structures in 2D materials with high symmetry. They can still possess a relatively low symmetry in regular corrugated modes. Therefore, unique physical properties emerge with pentagonal structures, leading to novel electronic applications.

Figure 1a shows the top and side views of the monolayer PdSe<sub>2</sub> structure; it can be clearly seen that the one-unit cell contains four Pd atoms and eight Se atoms (top plane). In

one PdSe<sub>2</sub> layer, the two Se atoms cross the Pd layer in the form of a Se–Se dumbbell (bottom plane).

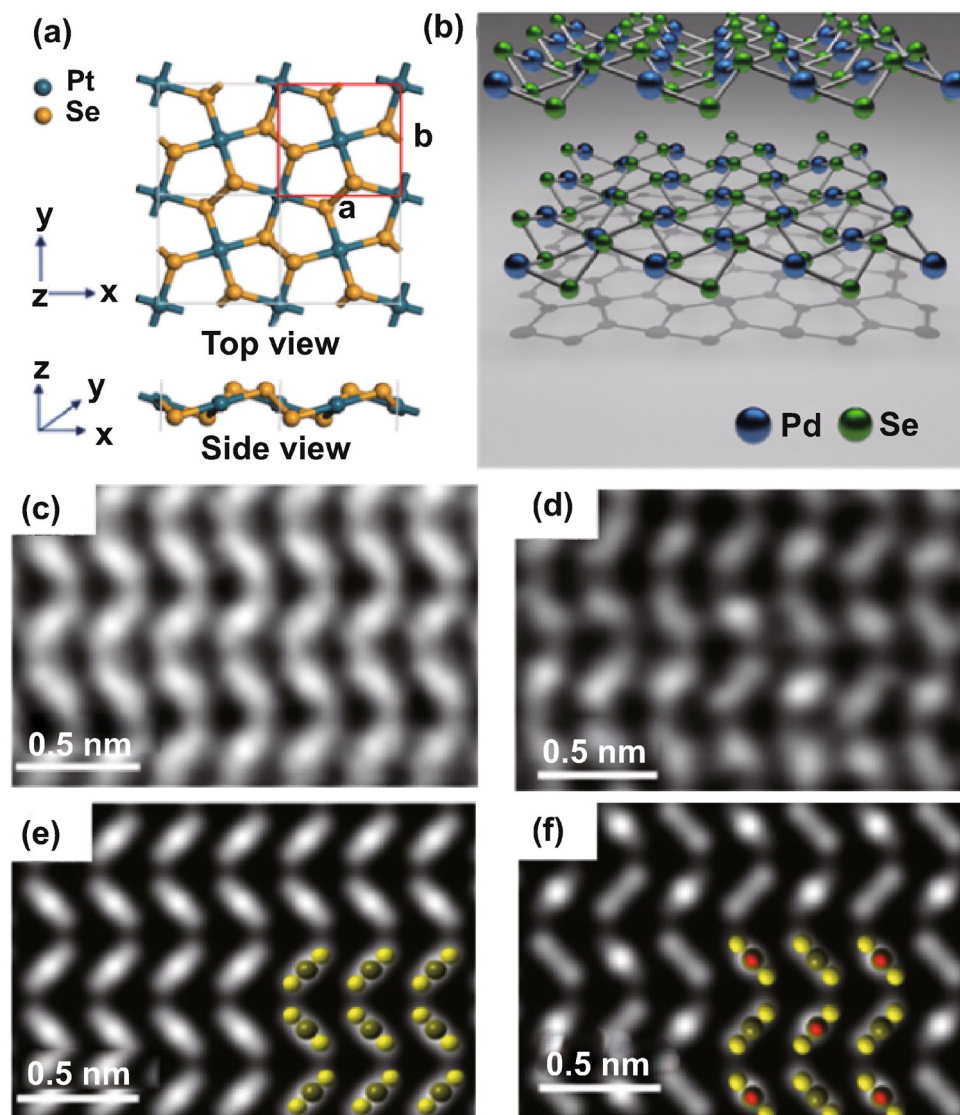
The uncommon layered structure is composed entirely of pentagonal rings, in which each Pd atom binds to four Se atoms, and two adjacent Se atoms form a covalent bond in one layer [23]. Hence, there exists no dangling bond in one PdSe<sub>2</sub> layer, and these layers interact via van der Waals forces, resulting in excellent stability in air. The lattice parameters *a*, *b*, and *c* are, respectively, 5.75, 5.87, and 7.69 Å for PdSe<sub>2</sub>. Each layer of PdSe<sub>2</sub> crystal has a vertical puckering height of 1.6 Å, where Pd atoms exhibit an unusual planar tetra-coordination [15].

Figure 1b shows the corresponding three-dimensional (3D) schematic of a monolayer PdSe<sub>2</sub> structure from a projected top view and side view [15], which is similar to that of black phosphorus (BP).

Figure 1c, d exhibits the annular dark-field (ADF) image of the PdSe<sub>2</sub> crystals, as generated via scanning transmission electron microscopy (STEM), as well as the corresponding image simulations (Fig. 1e, f) [15]. This approach can well prevent the formation of the disordered region of PdSe<sub>2</sub> flakes due to the transfer process onto the TEM grid. As can be seen, owing to the difference in symmetry, the even and odd layers of PdSe<sub>2</sub> flakes can give rise to a variation in the ADF images. Nonetheless, these patterns are in good agreement with the corresponding image simulations [15]. Moreover, the STEM images verify the puckered structure with waved Pd–Se layers of PdSe<sub>2</sub>.

The morphology and structure of PdSe<sub>2</sub> have shown satisfactory property–structure correlation. Indeed, the anisotropic orientation of the PdSe<sub>2</sub> domains results in polarized light detection [29]. The strain engineering influences the phonon response, which demonstrates its potential in the field of flexible electronics. Defect engineering such as vacancies could affect the air stability of the PdSe<sub>2</sub> transistor as well as the Ohmic contact. The phase transition mechanism should be investigated for a better understanding, and more new phases of PdSe<sub>2</sub> can be exploited for further applications. The high-pressure induced phase of PdSe<sub>2</sub> renders a photovoltaic material. The hexagonal T phase of PdSe<sub>2</sub> resulted in a high-efficiency solar cell. The pyrite phase PdSe<sub>2</sub> exhibits superconductivity induced by high pressure.

Bulk PdSe<sub>2</sub> crystals display D<sub>2h</sub> point group symmetry and *Pbca* space group symmetry [28]. The pentagonal PdSe<sub>2</sub> belongs to the phase of marcasite in the crystal system of



**Fig. 1** Atomic structure of PdSe<sub>2</sub>. **a** Top view and side view of penta-PdSe<sub>2</sub> monolayers, where a unit cell is marked using a red line. The blue and yellow spheres represent the Pd and Se atoms, respectively. Reprinted with permission from Ref. [199]. Copyright 2015, Royal Society of Chemistry. **b** 3D crystallographic structure of puckerd pentagonal PdSe<sub>2</sub>. **c, d** Z-contrast STEM images of PdSe<sub>2</sub> crystal structure with even and odd numbers of layers. **e, f** Corresponding simulated images of PdSe<sub>2</sub> crystals with even and odd numbers of layers. Insets in **e, f** display atomic models of the corresponding STEM images. Reprinted with permission from Ref. [15]. Copyright 2017, American Chemistry Society

orthorhombic [27]. By comparison, thin PdSe<sub>2</sub> flakes with an odd number of layers are allocated to space group  $P2_1/c$  (No. 14) and point group  $C_{2h}$  ( $2/m$ ), which possess inversion symmetry, while thin PdSe<sub>2</sub> flakes with an even number of layers are allocated to space group  $Pca2_1$  (No. 29) and point group  $C_{2v}$  ( $mm2$ ), which do not possess inversion symmetry [15].

## 2.2 Electron Orbital Properties

The conventional hexagonal structures are featured with isotropy, e.g., MoS<sub>2</sub>. The symmetrical hexagons lead to weak interlayer interaction due to the  $d^4sp$  hybridization in TMDCs [20]. Here, the Mo and W elements are in lack of  $d$  orbital electrons. Besides, the  $d$  orbital of Pt atom and

$p_z$  orbital of S atom are hybridized into  $d^2sp^3$  type, which accounts for the strong interlayer interaction in  $\text{PtS}_2$  [30].

But the hybridization between Pd and Se orbitals is complicated in  $\text{PdSe}_2$ . First, one need to understand the electron configuration of these two elements. The Pd metal has a fully occupied  $d$  orbital with electron configuration of  $[\text{Kr}]4d^{10}$ . And the Se is a  $p$ -block element, with an electron configuration of  $[\text{Ar}]3d^{10}4s^24p^4$ . In a single-layer  $\text{PdSe}_2$ , one Pd atom is coordinated to four Se atoms, forming a square-planar structure [31]. Quite often, the  $\text{Pd}^{2+}$  results in the  $d^8$  configuration such as  $\text{PdCl}_2$ . Therefore, the  $\text{PdSe}_2$  possesses a phase of marcasite analogous to the  $\text{FeS}_2$  [27]. The weak hybridization occurs between the  $4d_z^2$  orbitals of Pd atom and  $4p_z/3d_z^2$  orbitals of Se atom, which led to the low symmetry [31].

The hybridization of Pd 4d orbit and Se 4p orbit has resulted in the covalent bond in  $\text{PdSe}_2$  [32]. The bands near Fermi level are contributed by the  $p$  orbitals of Se element. The conduction band minimum and valence band maximum of monolayer  $\text{PdSe}_2$  have stemmed from the  $p$  states of Se and  $d$  states of Pd. The spin-orbital coupling does not influence the electronic structure of monolayer  $\text{PdSe}_2$  [33]. But, with increasing the layer number, the interlayer coupling becomes strong and decreases the bandgap of bilayer and trilayer  $\text{PdSe}_2$  compared with monolayer  $\text{PdSe}_2$  [32]. Besides, the stacking types determine the bandgap of  $\text{PdSe}_2$ , e.g., the AA and AB stacking for bilayer  $\text{PdSe}_2$  and the AAA, ABA, and ABB stacking for trilayer  $\text{PdSe}_2$  [32].

Indeed, the pentagonal  $\text{PdSe}_2$  is analogous to other puckered 2D materials, i.e., phosphorene and silicene, which feature with anisotropy [15]. The buckling of puckered 2D materials lead to a strong spin-orbital coupling between adjacent two layers, which is accounted for the topological quantum phase transition.

With the doping of transition-metal atoms such as Cr and Mn, new energy levels were introduced into the band structure of  $\text{PdSe}_2$  [34], which decrease its bandgap and introduce new spin nondegenerate states. These spin states around the Fermi level could cause the spin polarization.

After knowing the electron orbital theory, we now come to discuss the band structure of  $\text{PdSe}_2$ .

### 2.3 Electronic Band Structure

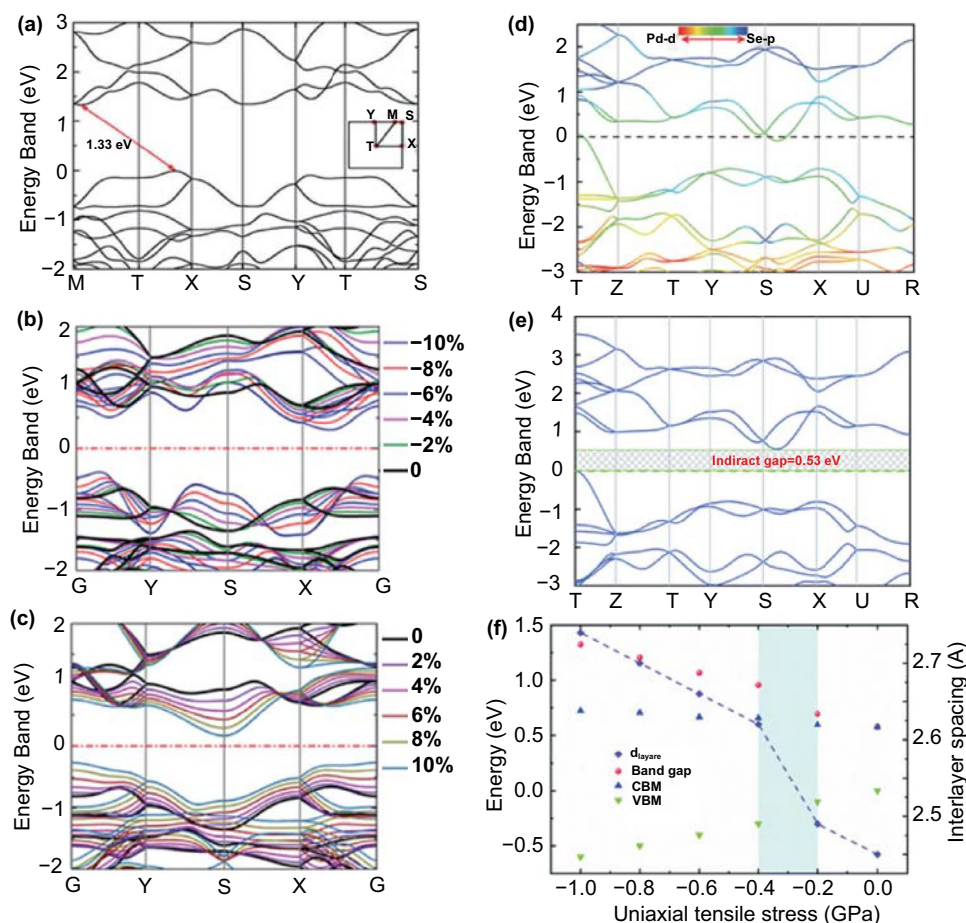
This section discusses the electronic energy band structures and density of states (DOSs) of  $\text{PdSe}_2$ . Similar to that of most layered TMDCs, the indirect bandgap of  $\text{PdSe}_2$  largely depends on the number of layers.

The bandgap of  $\text{PdSe}_2$  has been calculated [33] via the approaches of generalized gradient approximation (GGA), density functional theory (DFT) of Perdew, Burke, and Ernzerhof (PBE). Here, the bandgap of  $\text{PdSe}_2$  is defined as the energy difference between the valence band (VB) and the conduction band (CB). The indirect bandgap of monolayer  $\text{PdSe}_2$  with semiconducting characteristics is 1.33 eV (Fig. 2a), and this decreases with the increase in the number of  $\text{PdSe}_2$  layers until the bulk  $\text{PdSe}_2$  has no bandgap (0 eV) with semimetallic characteristics (Fig. 2d).

In the cases of TMDCs and phosphorene, the valence band maximum (VBM) and conduction band minimum (CBM) are located along the high-symmetry lines. However, in the electronic structure of  $\text{PdSe}_2$  [35], VBM is located between the high-symmetry  $\Gamma$  and X, while the CBM is located between M and  $\Gamma$  (Fig. 2a).

Meanwhile, the effects of strain, particularly biaxial strains, have been investigated on the electronic and optical properties of  $\text{PdSe}_2$  [36]. Figure 2b, c shows the evolution of the monolayer  $\text{PdSe}_2$  energy bands under compressive and tensile strains, respectively. The black line represents the energy band of  $\text{PdSe}_2$  in the unstrained state, while the other colors represent the energy bands of  $\text{PdSe}_2$  in the various strained states. The compressive and tensile strains decrease the CBM and increase the VBM of monolayer  $\text{PdSe}_2$ , and the VBM and CBM rise to a maximum value for compressive or tensile strains of  $-10\%$ , leading to the minimum bandgap of monolayer  $\text{PdSe}_2$  [35]. Moreover, under compressive strain along the  $x$ -direction, the monolayer  $\text{PdSe}_2$  shows a negative Poisson's ratio, possibly resulting from the Se-Se bond [37].

Figure 2d shows the energy band of bulk  $\text{PdSe}_2$ , where the electronic structure shows a negative indirect bandgap with semimetallic characteristics at the DFT level. However, VB and CB are not entangled around the Fermi level [33]. A semimetallic feature of bulk  $\text{PdSe}_2$  can be observed through



**Fig. 2** **a** Electronic band structure of monolayer PdSe<sub>2</sub> with no strain. Reprinted with permission from Ref. [35]. Copyright 2018, Royal Society of Chemistry. Electronic band structure of monolayer PdSe<sub>2</sub> with symmetrical biaxial **b** compressive, and **c** tensile strains. Reprinted with permission from Ref. [36]. Copyright 2018, American Chemistry Society. **d** Electronic band structure of bulk PdSe<sub>2</sub>, where the Fermi level is set to zero. The red and blue regions represent the contributions from Pd 4d and Se 4p states, respectively. **e** Electronic band structure of bulk PdSe<sub>2</sub> under a tensile stress of 1.0 GPa. **f** Bandgap, CBM, VBM, and interlayer spacing ( $d_{\text{layers}}$ ) of bulk PdSe<sub>2</sub> as a function of the uniaxial tensile stress, where the blue region presents the rapid increase of  $d_{\text{layers}}$ . Reprinted with permission from Ref. [33]. Copyright 2019, Royal Society of Chemistry

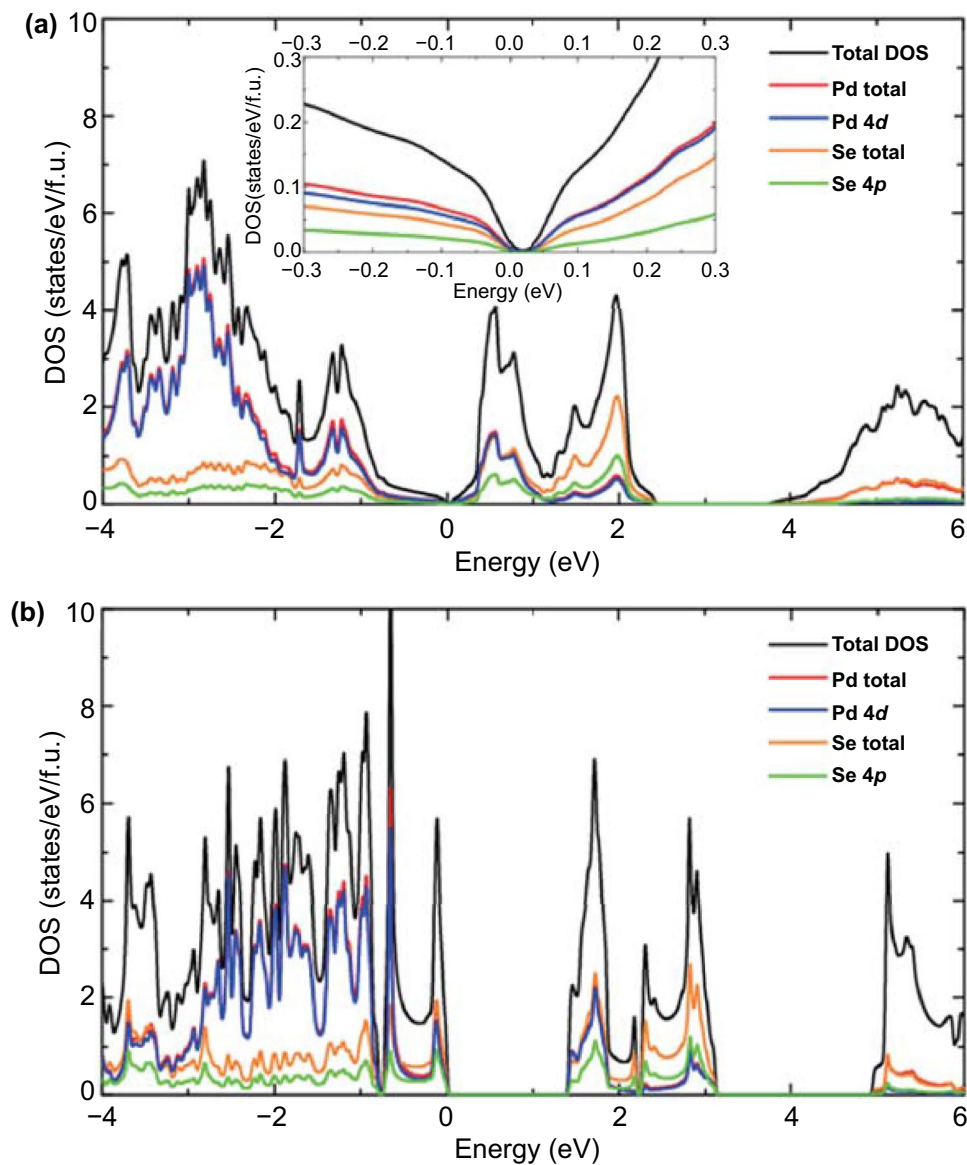
ultraviolet photoemission spectroscopy [26] and optical absorption [25]. However, bulk PdSe<sub>2</sub> exhibits semiconducting characteristics from resistivity experiments [38]. Hence, further research is necessary to understand the bandgap of bulk PdSe<sub>2</sub> better owing to this contradiction.

Figure 2e reveals the electronic band structure of bulk PdSe<sub>2</sub> calculated via DFT under the tensile stress of -1.0 GPa, whereby a bandgap of 0.48 eV is observed. When uniaxial tensile stress is applied to bulk PdSe<sub>2</sub> along the out-of-plane direction, the lattice parameter  $c$  and interlayer distance increase [33]. In orthorhombic PdSe<sub>2</sub>, the bandgap is positively correlated with the interlayer distance, indicating that the interlayer interaction has a significant influence on

the electronic structure. Figure 2f shows the interlayer spacing ( $d_{\text{layers}}$ ) and bandgap of bulk PdSe<sub>2</sub> as a function of the uniaxial tensile stress. As the interlayer spacing increases, VBM decreases dramatically, while CBM increases slightly, resulting in an increase in the bandgap of bulk PdSe<sub>2</sub>.

Figure 3 depicts the electronic DOSs for both bulk and monolayer PdSe<sub>2</sub> calculated in denser  $k$  meshes with values of  $23 \times 23 \times 17$  and  $40 \times 40 \times 1$ , respectively [27]. In the inset of Fig. 3a, the bandgap of bulk PdSe<sub>2</sub> is 0.03 eV, while that of monolayer PdSe<sub>2</sub> is approximately 1.43 eV (Fig. 3b). These values are slightly higher than the bandgap values obtained through the traditional GGA-PBE functional, indicating an underestimation of the bandgap





**Fig. 3** Calculated density of states of **a** bulk PdSe<sub>2</sub> and **b** monolayer PdSe<sub>2</sub>. “DOS” denotes the density of states. Reproduced with permission from Ref. [27]. Copyright 2015, AIP Publishing LLC

value. This uncertainty of the bandgap may be because PdSe<sub>2</sub> has a high number of defects and in-plane anisotropic absorption properties.

In each layer, covalent bonding results in a distinct hybridization between the Pd 4d and Se 4p states. The projected DOSs show that the Pd 4d and Se 4p states contribute the most to the VBM and CBM, and the more substantial contribution of Pd 4d orbitals to the total DOSs increases at an energy below -1 eV [27].

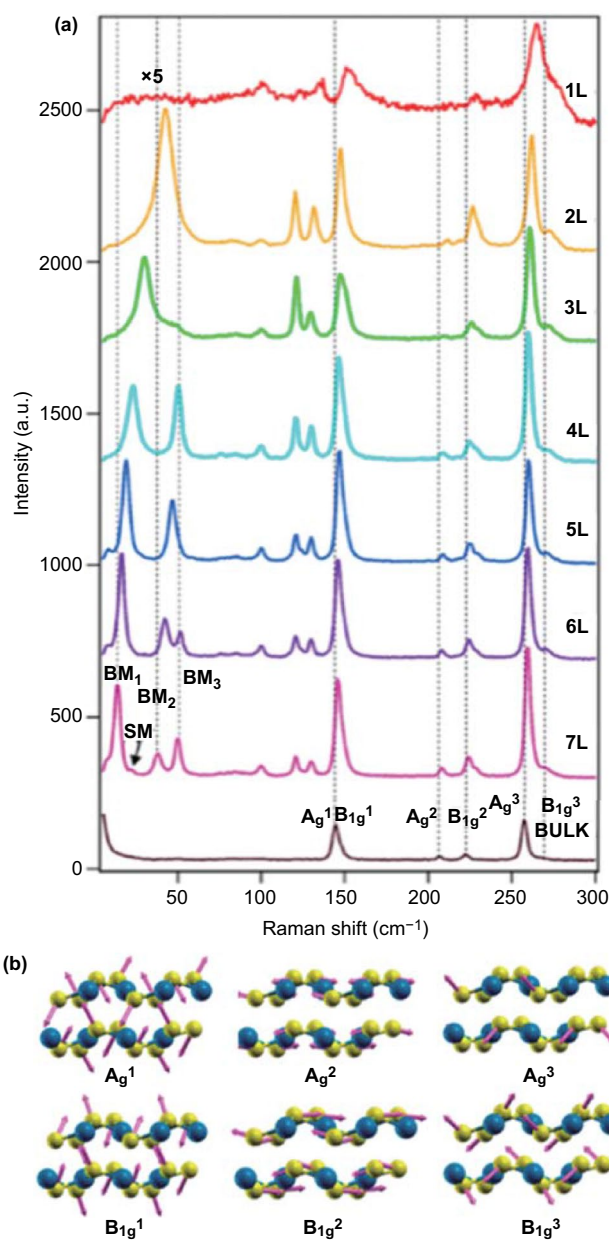
## 2.4 Vibrational Phonon Modes

Raman spectroscopy, which is a critical technique for 2D material characterization, was utilized to investigate the PdSe<sub>2</sub> structure. In the Raman spectra of PdSe<sub>2</sub>, the peak position and intensity are shown to change anomalously with different numbers of PdSe<sub>2</sub> layers, resulting from the electronic hybridization and strong interlayer coupling in the PdSe<sub>2</sub> crystal [15].

To provide a better understanding, Fig. 4a shows the Raman spectra of PdSe<sub>2</sub> samples from monolayer to bulk, which demonstrates the evolution of the PdSe<sub>2</sub> vibrational modes. There are four obvious peaks in the high-frequency (HF) Raman spectra region (100–300 cm<sup>-1</sup>), including six atomic vibrational modes [15]. The six peaks are at 144.3, 146.9, 206.7, 222.7, 257.8, and 268.6 cm<sup>-1</sup>, and the corresponding A<sub>g</sub><sup>1</sup>, B<sub>1g</sub><sup>1</sup>, A<sub>g</sub><sup>2</sup>, B<sub>1g</sub><sup>2</sup>, A<sub>g</sub><sup>3</sup>, and B<sub>1g</sub><sup>3</sup> phonon modes of PdSe<sub>2</sub> are marked with dotted lines in Fig. 4a. As the number of PdSe<sub>2</sub> layers increases, the major peaks show a red shift, with the B<sub>1g</sub><sup>1</sup> peak changing the most and the A<sub>g</sub><sup>3</sup> peak changing the least. The main reasons for this are the in-plane lattice constant variations and the strong interlayer coupling of PdSe<sub>2</sub>, which causes abnormal shifts and a broad bandgap [15].

Figure 4b shows six atomic vibrational models, where the purple arrows represent the relative movements between the Pd and Se atoms. Among all the vibrational modes of PdSe<sub>2</sub>, the vibrations of Se–Se atoms are predominant. Indeed, the Se–Se bond presents a much stronger vibration intensity than that of the Pd–Se bond [39]. Moreover, there are three peaks in the low-wavenumber region (approximately at 101, 121, and 130 cm<sup>-1</sup>) owing to variations in the symmetry. As the number of PdSe<sub>2</sub> layers decreases, the space group transforms from *Pbca* to *Pca2*<sub>1</sub>, leading to the emergence of the B<sub>1g</sub><sup>3</sup> mode and new peaks (268.6 cm<sup>-1</sup>) in few-layer PdSe<sub>2</sub>.

Low-frequency (LF) Raman spectroscopy (< 100 cm<sup>-1</sup>) was used to study the layer characteristics of PdSe<sub>2</sub> further. As the two primary LF features, the breathing and shear modes pertain to the interlayer vibrational modes, and they depend on the relative motion perpendicular and parallel to the atomic layers, respectively. The breathing modes (BM<sub>1</sub>, BM<sub>2</sub>, and BM<sub>3</sub>) and shear modes (SM) are marked in Fig. 4a. For PdSe<sub>2</sub>, the intralayer covalent bonds along with the vibrational directions of adjacent atomic layers determine the intensities of the LF vibrational modes. Moreover, the interlayer vibrational modes display high intensities in few-layered PdSe<sub>2</sub> flakes, even overtop the intralayer modes (HF features), which reflects the strong interlayer coupling of PdSe<sub>2</sub>. With the increase in the layer number of PdSe<sub>2</sub>, the LF Raman spectra exhibited a distinct red shift for the branches of the breathing modes. Such a shift was more pronounced than that of Raman peaks in the HF region. The full-width half-maximum (FWHM) of BM<sub>1</sub> narrowed from 12 cm<sup>-1</sup> (2 L) to 2.5 cm<sup>-1</sup> (7 L) owing to the reduced phonon scattering rate in thicker



**Fig. 4** Vibrational properties of PdSe<sub>2</sub>. **a** Raman spectra of PdSe<sub>2</sub> flakes of different layer number from monolayer to bulk. **b** Six major vibrational modes of PdSe<sub>2</sub>, which are labeled as A<sub>1g</sub>, B<sub>1g</sub>, A<sub>2g</sub>, B<sub>2g</sub>, A<sub>3g</sub>, and B<sub>3g</sub>. Reprinted with permission from Ref. [39]. Copyright 2020, American Chemistry Society

PdSe<sub>2</sub> flakes [18]. Thus, the number of PdSe<sub>2</sub> layers can be precisely determined via Raman spectroscopy.

As mentioned above, PdSe<sub>2</sub> presents relatively low symmetry owing to its puckered pentagonal structure, which exists in a few other TMDCs except PdSe<sub>2</sub>. Thus, PdSe<sub>2</sub> exhibits a unique anisotropy property, and the Raman

scattering features of PdSe<sub>2</sub> have been recently conducted to study the vibrational anisotropy [40].

## 2.5 Polarization Properties

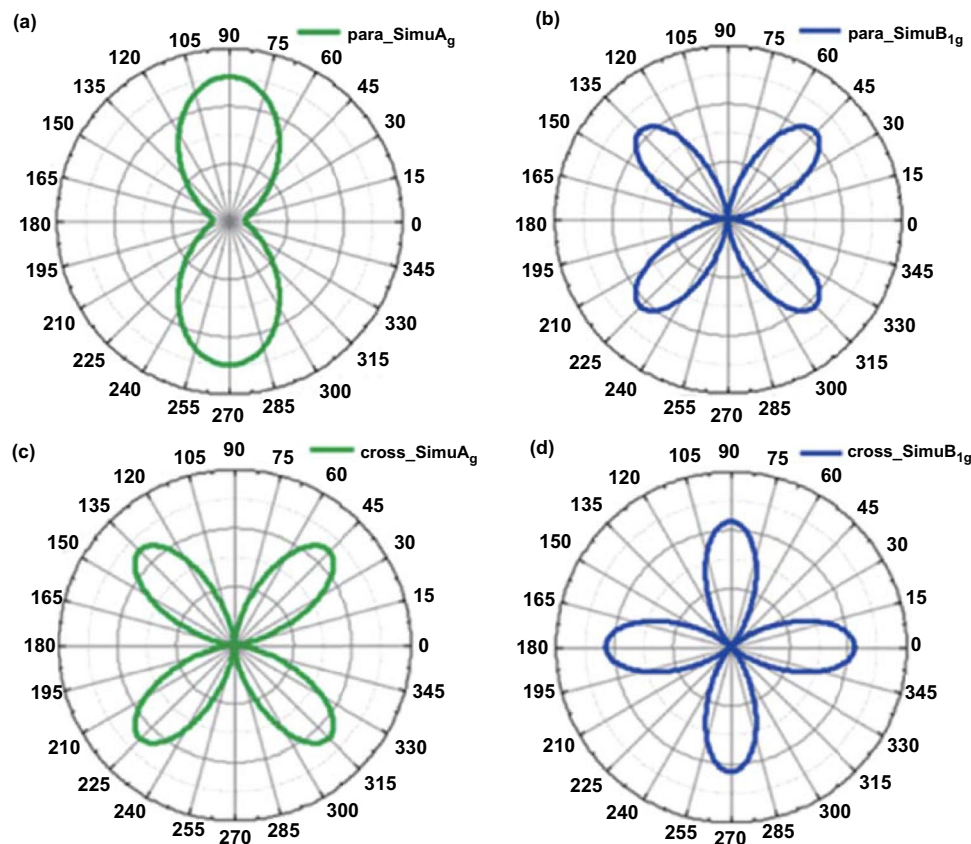
Compared with 2D TMDCs, PdSe<sub>2</sub> possesses unique optoelectronic polarization properties because of anisotropy [16, 40], which is a great advantage for detecting polarized light. The PdSe<sub>2</sub> has an appropriate bandgap (1.1 eV) and excellent optical absorption at the near-infrared range [40].

To date, PdSe<sub>2</sub> remains the only choice for polarization investigation among the noble metal dichalcogenides. Indeed, the pentagonal PdS<sub>2</sub> may possess the photoelectric properties analogous to the PdSe<sub>2</sub>. But 2D PdS<sub>2</sub> investigation remains the theoretical calculation [13] and has yet been successfully prepared in experiments. This is probably because of the thermodynamic instability of marcasite PdS<sub>2</sub> in the air [14].

Therefore, the application of PdSe<sub>2</sub> exhibits high promise in the applications of optoelectronics and electronics.

Polarization-resolved Raman measurements and theoretical calculations were employed to systematically investigate the anisotropic optical properties [39]. Figure 5a, b shows the Raman intensity simulations of the A<sub>g</sub> and B<sub>1g</sub> modes versus the polarization angle in 3 L PdSe<sub>2</sub> under parallel polarization configuration. The A<sub>g</sub> modes reveal a period of 180°, and the B<sub>1g</sub> modes reveal a period of 90° in the parallel configuration.

Figure 5c, d presents the Raman intensity of both modes under parallel polarization configuration. Indeed, the A<sub>g</sub> and B<sub>1g</sub> modes both reveal a period of 90° under the cross configuration. The LF Raman peaks possess A<sub>g</sub> or B<sub>1g</sub> symmetry because the LF modes follow the group theory, similar to the HF modes, and the breathing modes and shear modes possess A<sub>g</sub> and B<sub>1g</sub> symmetry, respectively.



**Fig. 5** Polarization Raman intensities of PdSe<sub>2</sub>. The Raman intensity of A<sub>g</sub> mode (a) and B<sub>1g</sub> mode (b) under the parallel configuration with the simulation of the anisotropic modes. Raman intensity of A<sub>g</sub> mode (c) and B<sub>1g</sub> mode (d) under cross configuration of polarization Raman test. The layer number of PdSe<sub>2</sub> is 3 for polarization Raman test. Reprinted with permission from Ref. [39]. Copyright 2020, American Chemistry Society

## 2.6 Optical Absorption Properties

The anisotropic features of PdSe<sub>2</sub> can be verified based on its optical absorption. Figure 6a shows the optical absorbance of 1–3 L PdSe<sub>2</sub> flakes at measurement angles of 0° and 90°, where an interesting orthogonal crossover is observed at around 470 nm [39]. Owing to the decrease in the bandgap, the increase in the number of PdSe<sub>2</sub> layers leads to a slight red shift of the intersection point after 600 nm.

Figure 6b shows the variation in PdSe<sub>2</sub> absorption with the polarization angle for a systematic investigation of the anisotropic characteristics. Almost all the absorption spectra of PdSe<sub>2</sub> intersect at 472 nm when the polarization angle varies from -90° to 90°.

## 2.7 Photoelectronic Properties

Based on the optical absorption of PdSe<sub>2</sub>, the photoreponse of 2D PdSe<sub>2</sub> was investigated. The spatially resolved photocurrent mapping was collected for the few-layer PdSe<sub>2</sub> devices [41]. Figure 4g shows a stable photocurrent of the device under 1060-nm illumination at two metal-PdSe<sub>2</sub> junctions without any applied voltage.

To further study the photocurrent generation mechanisms, gate-dependent scanning photocurrent measurements were taken (Fig. 7a, b). Besides, the photocurrent could be tuned from positive to negative when regulating

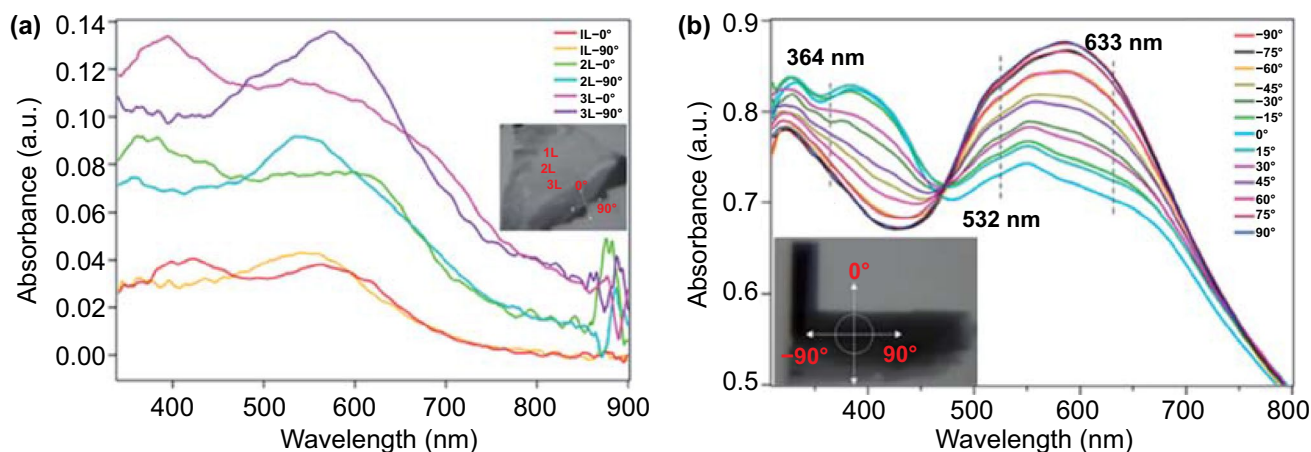
the drain–source voltage from 150 to -150 mV (Fig. 7c). The photocurrent mapping could be applied in the image sensing.

A strong photocurrent resonance peak emerges at 1060 nm, which may be due to an indirect optical transition. Due to the potential barriers created by the Fermi level alignment, a built-in electric field separates the photogenerated electron–hole pairs in the PdSe<sub>2</sub> device [41].

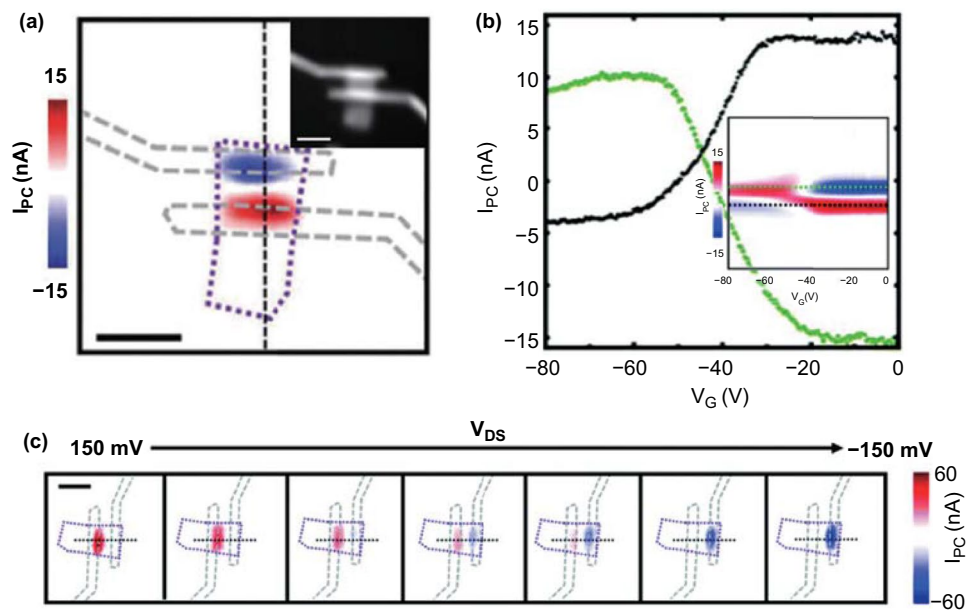
## 2.8 Thermoelectric Properties

Over the past decade, thermoelectric devices have attracted much attention because they can directly convert thermal energy into electrical energy. Because the bond saturation significantly enhances the thermal energy transport in 2D pentagonal materials, a unique feature is that PdSe<sub>2</sub> possesses good thermoelectric properties. In particular, monolayer PdSe<sub>2</sub> can be applied as a promising high-performance thermoelectric material in the future owing to its high Seebeck coefficient ( $> 200 \mu\text{V K}^{-1}$ ) [27]. For few-layer PdSe<sub>2</sub>, the energies of CB and VB were found to be convergent during a systematic investigation of its lattice structure and electronic properties, which indicates the significant thermoelectric properties of PdSe<sub>2</sub> [42].

Figure 8a shows the electron transport coefficient of PdSe<sub>2</sub> based on the constant relaxation time approximations of the Boltzmann theory [39]. Clearly, when the



**Fig. 6** Polarized optical absorption of PdSe<sub>2</sub>. **a** Absorbance of 1–3 L PdSe<sub>2</sub> along the *x*-axis (90°) and *y*-axis (0°). Inset: Optical micrograph of the PdSe<sub>2</sub> flakes of different thicknesses. **b** Polarization-resolved absorption spectra of bulk PdSe<sub>2</sub> within 300–800 nm spectra, with the measured angle from -90 to 90° in increments of 15°. Inset: Optical micrograph of the PdSe<sub>2</sub> sample. Reprinted with permission from Ref. [39]. Copyright 2020, American Chemistry Society



**Fig. 7** Photoelectric current mapping of PdSe<sub>2</sub>. **a** Scanning photocurrent images of the PdSe<sub>2</sub> device under 1060-nm illumination with  $V_G = V_{DS} = 0$  V, where the scale bar represents 5  $\mu\text{m}$ . Inset: Reflection image of corresponding device with scale bar of 5  $\mu\text{m}$ . **b** Photocurrents along the green and black dashed lines. Inset: Photocurrent signals as a function of gate voltage along the black dashed line in **a**. **c** Scanning photocurrent images of the PdSe<sub>2</sub> device in **a** with  $V_{DS}$  from  $-150$  to  $150$  mV, where the scale bar represents 5  $\mu\text{m}$ . Reprinted with permission from Ref. [41]. Copyright 2019, Royal Society of Chemistry

doped carrier concentration increased, the conductivity ( $\sigma$ ) increased, while the Seebeck coefficient decreased. For monolayer PdSe<sub>2</sub>, the Seebeck coefficient can reach  $660 \mu\text{V K}^{-1}$ , which is comparable to that of some reported 2D materials [43]. The  $S$  for  $p$ -type doping is more asymmetric than that for  $n$ -type doping, and this provides the possibility for the design of transverse thermoelectric devices. Figure 8a proves that the power factor (PF)  $S^2\sigma$  possesses distinct anisotropy, and this results from the large anisotropy of  $\sigma$  and  $S$ .

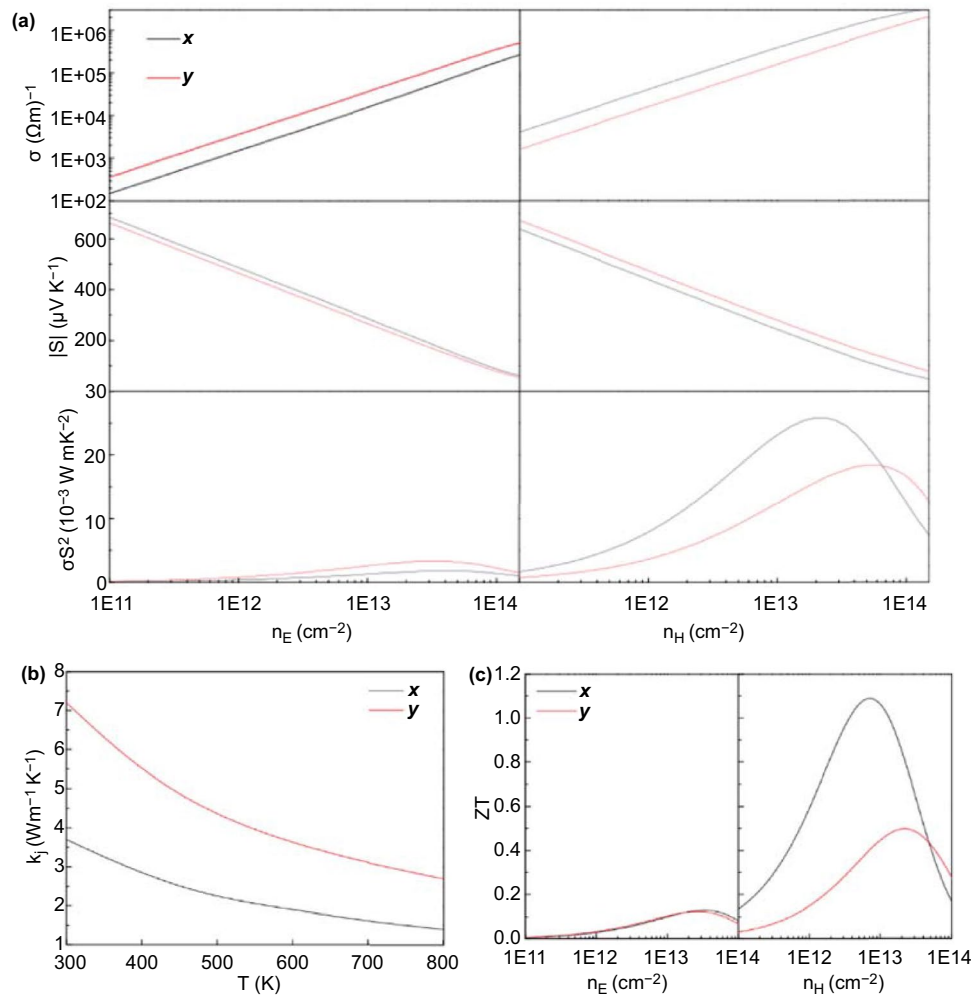
Figure 8b shows the calculation of the lattice thermal conductivity  $\kappa_l$  through the phonon Boltzmann transport equation and DFT. The lattice thermal conductivity of PdSe<sub>2</sub> is much lower than that of monolayer MoS<sub>2</sub> and GX<sub>2</sub> [44], and it exhibits a large directional anisotropy. Figure 8c displays the relationship between the dimensionless figure of merit (ZT) value of the doped monolayer PdSe<sub>2</sub> and the carrier concentration at room temperature.

The ZT value of monolayer PdSe<sub>2</sub> is small and almost isotropic, while that for  $p$ -type doping is large and strongly anisotropic. Therefore, the high  $S$ , low  $\sigma$ , and high ZT values of monolayer PdSe<sub>2</sub> at room temperature make PdSe<sub>2</sub> suitable for thermoelectric devices.

## 2.9 Phase Transformation Properties

Two-dimensional materials, especially TMDCs, can possess various properties via change in their phases, namely in terms of bonding and configurations, which can be exploited in other fields. For PdSe<sub>2</sub>, the interlayer interaction is relatively more reliable than the intralayer connection through covalent bonds, which facilitates the transition to other phases under different external parameters. The unique puckered pentagonal structure of PdSe<sub>2</sub> possesses imperfect rotational symmetry, resulting in high defect sensitivity, particularly Se vacancies ( $V_{\text{Se}}$ ), which facilitates the occurrence of different phase transitions [45].

PdSe<sub>2</sub> structure could transform into a Pd<sub>2</sub>Se<sub>3</sub> structure (Fig. 9a) through  $V_{\text{Se}}$  [46]. From the STEM images, it was found that the preferred monolayer phase form exfoliated from bulk PdSe<sub>2</sub> is not a PdSe<sub>2</sub> structure. Through analysis of the quantitative STEM image intensity and DFT calculations, a new stable monolayer phase was determined to be Pd<sub>2</sub>Se<sub>3</sub>, which corresponds to the result from the experimental ADF-STEM image (Fig. 9b) [47].



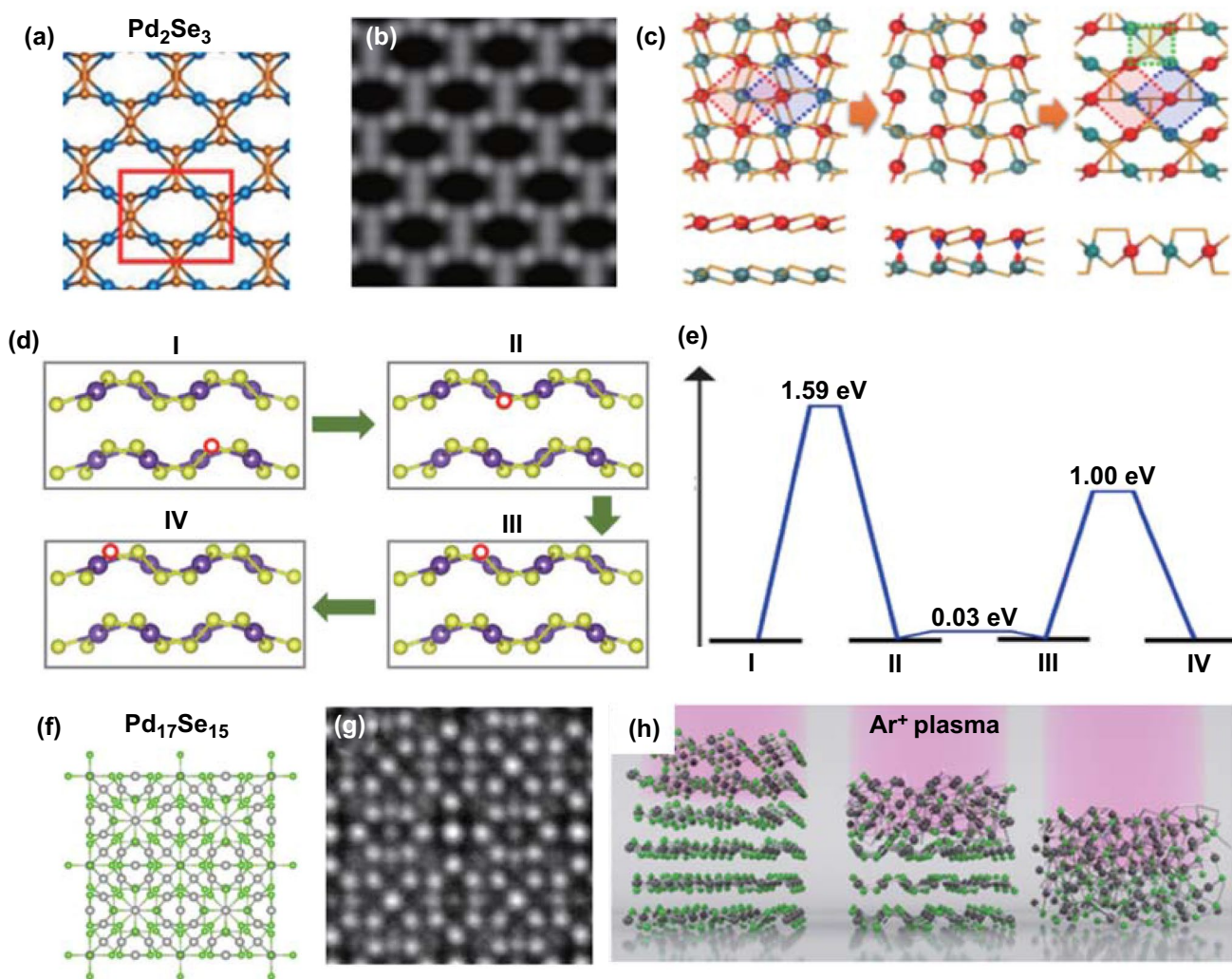
**Fig. 8** Thermoelectric properties of PdSe<sub>2</sub>. **a** Thermoelectric transport coefficients  $\sigma$ ,  $S$ , and  $S^2\sigma$  versus carrier concentration for PdSe<sub>2</sub> with *n*-type (left) and *p*-type (right) doping at room temperature. **b** Lattice thermal conductivity of monolayer PdSe<sub>2</sub> as a function of temperature. **c** Thermoelectric characteristics ( $ZT$ ) of monolayer PdSe<sub>2</sub> with *n*-type (left) and *p*-type doping (right) at room temperature. Adapted under the terms of the CC-BY Creative Commons Attribution 4.0 license (<https://creativecommons.org/licenses/by/4.0/>) from Ref. [138]. Copyright 2018, The Authors, published by Springer Nature

The reconstruction of Pd<sub>2</sub>Se<sub>3</sub> is due to the interlayer fusion mechanism, which results from the  $V_{\text{Se}}$  produced by electron radiation (Fig. 9c). According to the research results, the new Pd<sub>2</sub>Se<sub>3</sub> phase exhibits physical stability and high cohesive energy, implying robust chemical bonding. Moreover, the Pd<sub>2</sub>Se<sub>3</sub> monolayer is an excellent thermoelectric material with good electronic and optical properties [48].

Figure 9d shows the typical  $V_{\text{Se}}$  migration process in PdSe<sub>2</sub> in four possible configurations labeled I, II, III, and IV. The red circle indicates the position of the  $V_{\text{Se}}$ , which diffuses in the direction of the green arrow. The

theoretically calculated energy barriers were presented for the corresponding  $V_{\text{Se}}$  diffusion (Fig. 9e). For configurations I to II and III to IV, the energy barrier of interlayer and intralayer  $V_{\text{Se}}$  diffusion is 1.59 and 1 eV, respectively. These barriers are lower than the corresponding energy barriers in MoS<sub>2</sub>. These  $V_{\text{Se}}$  migrations are facilitated by the stronger interlayer interaction and weaker intralayer bond strength of PdSe<sub>2</sub>. For configurations II to III, the energy barrier for intralayer  $V_{\text{Se}}$  diffusion is 0.03 eV owing to the Se–Se bonding [45].

Environmental energy input elevates the energy of PdSe<sub>2</sub> and provides the activation energy for the formation



**Fig. 9** Atomic structure of different palladium selenide compounds. **a** Lattice structures and **b** corresponding simulated ADF-STEM image of monolayer  $\text{Pd}_2\text{Se}_3$ . Reprinted with permission from Ref. [47]. Copyright 2019, American Chemistry Society. **c** Schematic of reconstruction mechanism from bilayer  $\text{PdSe}_2$  to monolayer  $\text{Pd}_2\text{Se}_3$ , where the Se atoms are not presented. Reprinted with permission from Ref. [46]. Copyright 2017, American Physical Society. **d** Migration of  $\text{V}_{\text{Se}}$  configuration marked with the red circle in layered  $\text{PdSe}_2$ . **e** Energy barriers of  $\text{V}_{\text{Se}}$  diffusions calculated between different configurations. Reprinted with permission from Ref. [45]. Copyright 2017, American Physical Society. **f** Lattice structures and **g** corresponding ADF-STEM image of  $\text{Pd}_{17}\text{Se}_{15}$ , where green and gray spheres represent Se atoms and Pd atoms, respectively. **h** Process diagram of  $\text{Pd}_{17}\text{Se}_{15}$  formation from  $\text{PdSe}_2$  layer-by-layer through Ar plasma treatment. Reprinted with permission from Ref. [52]. Copyright 2019, American Chemistry Society

of other Pd–Se compounds, viz. the phase transformation occurs. For example, the thermal annealing, plasma, and laser treatment have resulted in the phase transition of  $\text{PdSe}_2$ . The typical external conditions are listed in Table 2 for the phase transition of  $\text{PdSe}_2$ .

First,  $\text{PdSe}_2$  can be transformed to  $\text{PdSe}_{2-x}$  with vacuum annealing. According to the traditional bulk Pd–Se phase diagram [49], the Se loss induces the change in the Pd/Se

ratio. Hence, the phase transition occurs after 30-s pulse annealing at 400 °C and the  $\text{PdSe}_{2-x}$  ( $x=0-1$ ) forms partially. Another 30-s pulse annealing completed the phase transition into  $\text{Pd}_2\text{Se}_3$ . The long-time annealing at 400 °C or heating at high temperature ( $> 400$  °C) leads to excess Se loss and thinning of 2D materials and finally form pure Pd materials [49]. Indeed, Se loss occurs in other metal selenide upon thermal annealing. Second, high laser power can lead to Se

**Table 2** The phase transition of PdSe<sub>2</sub> under different conditions

Phase transition from starting phase	To final phase	Conditions	References
Pristine PdSe <sub>2</sub> (2-4L)	Defective PdSe <sub>2</sub> (Se vacancy)	400 °C annealing in vacuum for 10 s	[49]
Defective PdSe <sub>2</sub>	50% PdSe <sub>2</sub> + 50% PdSe <sub>2-x</sub> (x = 0–1)	400 °C in vacuum for 30 s	[49]
Partial PdSe <sub>2-x</sub> (x = 0–1)	100% PdSe <sub>2-x</sub>	400 °C in vacuum for 30 s	[49]
PdSe <sub>2-x</sub> (x = 0–1)	Pd <sub>2</sub> Se <sub>3</sub> (striated; 1D channels)	400 °C heating in vacuum	[49]
Pd <sub>2</sub> Se <sub>3</sub>	PdSe	Vacuum annealing for Se loss	[49]
PdSe	Pd nanoparticles	Long vacuum annealing at 400 °C or heating at high temperatures (> 400 °C)	[49]
PdSe <sub>2</sub>	Pd <sub>17</sub> Se <sub>15</sub>	Ar plasma treatment	[52]
PdSe <sub>2</sub>	PdSe <sub>2-x</sub> (x = 0–1)	Laser irradiation (60 μW)	[50]
PdSe <sub>2</sub>	Pd nanoparticles	Laser irradiation (600 μW)	[50]
Monoclinic PdSe <sub>2</sub> (space group of I2/a)	Monoclinic PdSe <sub>2</sub> (C2/m space group)	High pressure (4.5 GPa)	[40]
PdSe <sub>2</sub>	Hexagonal PdSe <sub>2</sub> (P-3m1 space group)	High pressure (17.5 GPa)	[40]
Orthorhombic PdSe <sub>2</sub>	Ferroelastic PdSe <sub>2</sub> ; Transition of layer stacking from c to a-axis orientation	Uniaxial compressive stress (0.6 GPa)	[33]

loss and the formation of Pd nanoparticles [50]. Third, the high-pressure condition may induce the change of crystal structures [40] and layer stacking orientation [33].

Except for Pd<sub>2</sub>Se<sub>3</sub>, the Pd–Se binary phases include Pd<sub>17</sub>Se<sub>15</sub>, Pd<sub>7</sub>Se<sub>4</sub>, and Pd<sub>4</sub>Se. Through experiments, their metallic or superconducting characteristics have been displayed, and theoretical predictions have highlighted their topological quantum properties [51].

For instance, the Pd<sub>17</sub>Se<sub>15</sub> phase has excellent stability with analogous chemical bonds to those of the PdSe<sub>2</sub> phase [52]. Figure 9f, g shows the structure of the Pd<sub>17</sub>Se<sub>15</sub> phase and the corresponding STEM images. The phase transition results from the V<sub>Se</sub> in the PdSe<sub>2</sub> crystal are due to Ar plasma treatment (Fig. 9h). Moreover, the Raman spectra and STEM images indicate that the exposure time under Ar plasma irradiation affects the defects and degree of the phase transition in the PdSe<sub>2</sub> crystal.

We now come to the introduction of synthesis strategies and posttreatment approaches.

### 3 Synthesis Methods for Obtaining PdSe<sub>2</sub>

High-quality PdSe<sub>2</sub> has been obtained via several reliable methods [17], which shows promise for exploration of its remarkable properties. In this section, we review the specific PdSe<sub>2</sub> synthesis methods in terms of 3D bulk crystals and 2D thin films.

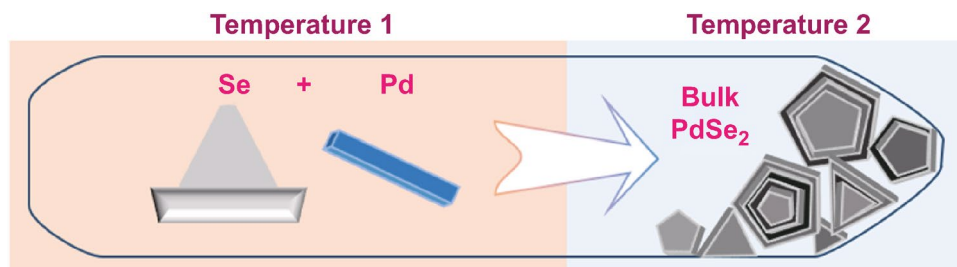
#### 3.1 Formation of 3D Bulk Crystals via Chemical Vapor Transport

The chemical vapor transport (CVT) method has been developed for the synthesis of most 3D bulk materials; it is an efficient method employed for laboratory synthesis and mass production. A common CVT reaction involves three processes: sublimation, transport, and deposition, and follows Le Chatelier's principle in thermodynamics [53].

The typical chemical vapor transport method has shown success in the growth of bulk PdSe<sub>2</sub> crystals [54]. Herein, a stoichiometric ratio of high-purity Pd and Se powder was mixed as the source and placed into an ampoule reactor with mineralizers as the transporting agent (Fig. 10). The sealed reactor was then heated under a preset temperature gradient, where Temperature 1 is the temperature for the sublimation of Pd and Se and Temperature 2 is the temperature for PdSe<sub>2</sub> deposition [54]. Generally, Temperature 1 is greater than Temperature 2 because the process of PdSe<sub>2</sub> crystal formation is endothermic [53].

For example, Pd and Se powders (mixed in an atomic ratio of 1:6) were filled in a sealed evacuated quartz ampule, which was slowly heated to 850 °C and maintained for 50 h. After the synthesis was completed, the quartz ampule was gradually cooled to 450 °C at a rate of 3 °C h<sup>-1</sup> and finally naturally cooled to room temperature [53]. Eventually, shiny single PdSe<sub>2</sub> crystals were obtained on millimeter-grade paper.





**Fig. 10** Scheme of the chemical vapor transport method for the bulk PdSe<sub>2</sub> formation. The selenium powder and Pd metal are sublimated in the left heating zone (Temperature 1) and cooling in the cold zone (Temperature 2) as bulk. The drawing was inspired by the literature [53]. The scheme was originally drawn by the authors in this review

### 3.2 Developing 2D Thin Film via Exfoliation

As devices with smaller sizes and higher performance are desired in the development of electronics, the growth of high-quality ultrathin 2D materials has become increasingly crucial. Thus, mechanical exfoliation and chemical vapor deposition (CVD) techniques are widely employed to produce layered PdSe<sub>2</sub> thin films.

After the synthesis of bulk PdSe<sub>2</sub> crystals, atomic PdSe<sub>2</sub> thin flakes could be easily obtained using the mechanical exfoliation method [15]. PdSe<sub>2</sub> flakes with different layers were transformed onto the Si/SiO<sub>2</sub> substrate (Fig. 11). The exfoliated PdSe<sub>2</sub> samples were then applied to different electronic devices.

The exfoliated PdSe<sub>2</sub> flakes have high crystallinity (Fig. 11) and intrinsic properties, which are beneficial for fabrication of individual devices [39]. The mechanical exfoliation method enables facile fabrication of the vdWHs [54]. However, the lack of large-area uniformity and layer-number controllability limits the applicability of the mechanical exfoliation method; moreover, the method is difficult to use for industrial production.

The typical features are compared in Table 3 for the synthesis approaches of 3D bulk, nanosheets, and 2D films of PdSe<sub>2</sub>.

Recently, the Au-assisted exfoliation method has shown success in the separation of monolayer 2D materials over a centimeter size [55]. In brief, the Au film is first deposited onto a target substrate [56]. Then, the tape with exfoliated 2D material is stuck onto the Au surface. Upon the pressing over the sample, the strong interaction forms between Au and 2D material. Eventually, monolayer or few-layer 2D materials remain over the Au surface after peeling off the tape. Here, the interlayer interaction in TMDCs can be

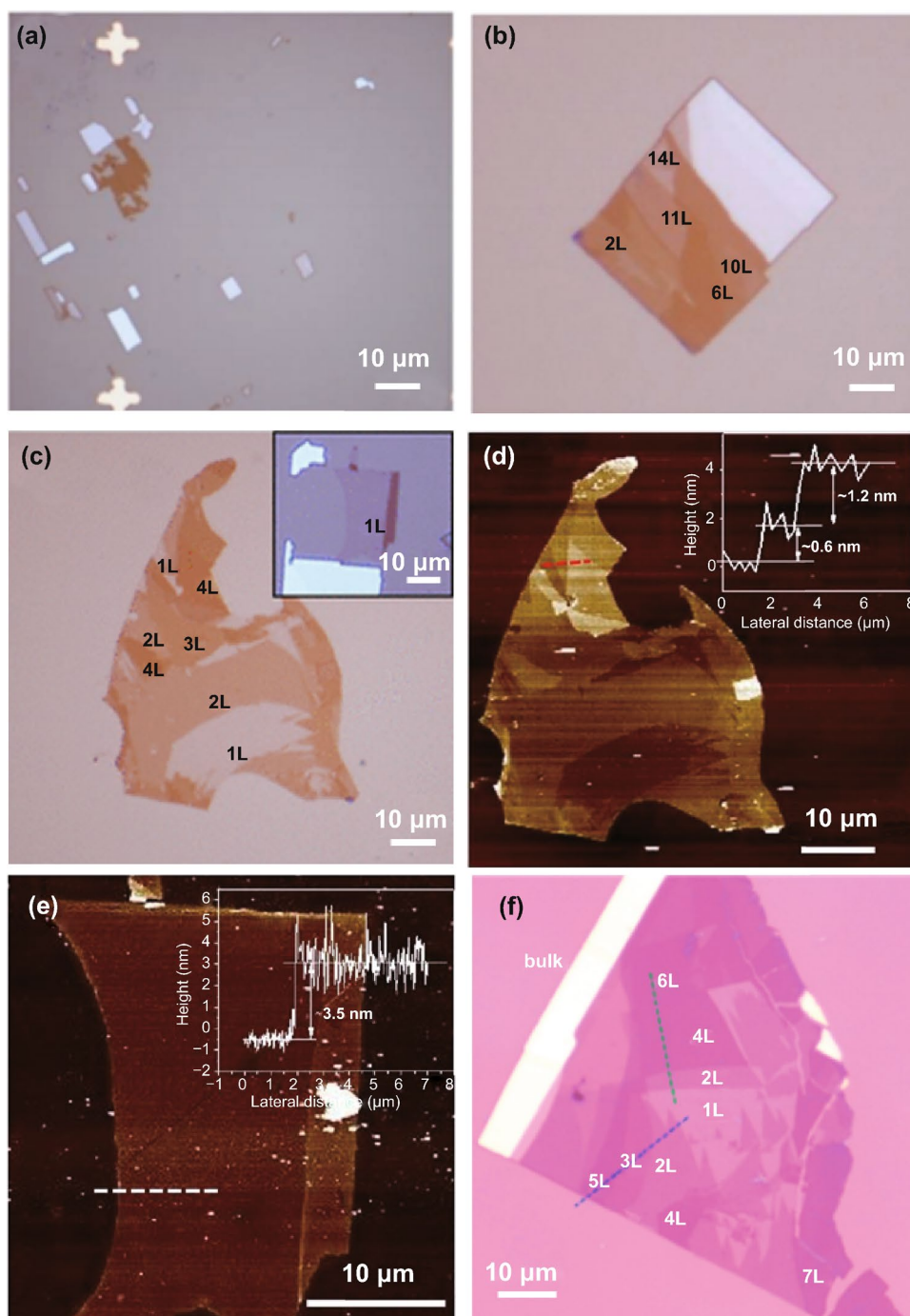
overcome by the interaction between Au film and 2D materials [57]. The strong van der Waals interaction between Au and the uppermost two-dimensional layered transition-metal chalcogenide promotes the exfoliation of the single layer, which leaves large-area single-layer domain on the Au surface. For example, Au-assisted exfoliation has produced large MoS<sub>2</sub> domains, i.e., 40 times greater than that produced by the tape-assisted exfoliation [57].

The Au-assisted exfoliation has become a universal approach for obtaining millimeter-sized 2D materials including PtSe<sub>2</sub>, PtTe<sub>2</sub>, and PdTe<sub>2</sub> [58]. It may apply to the exfoliation of PdSe<sub>2</sub> over a large size soon, which may accelerate the fabrication of electronic device arrays due to the large effective film area. The 2D materials over Au film by Au-assisted exfoliation can be applied in electrochemistry and photocatalyst [55].

Most 2D materials with large-area uniformity and high crystallinity can be synthesized via the CVD method or thermal selenization/sulfurization treatment [59]. Several approaches have been used to grow homogeneous PdSe<sub>2</sub> thin films, with satisfactory results being obtained. We now discuss thermal deposition approaches for synthesizing PdSe<sub>2</sub> films.

### 3.3 Chemical Vapor Deposition from the PdCl<sub>2</sub> and Se Reaction

A chemical vapor deposition strategy was developed by employing Pd-containing precursors and Se powders for synthesizing the PdSe<sub>2</sub> films. Here, PdCl<sub>2</sub> powder was selected as precursors [60]. A schematic of the CVD process with a three-zone tube furnace is shown in Fig. 12a.



**Fig. 11** Mechanically exfoliated PdSe<sub>2</sub> flakes. **a** Optical micrographs of exfoliated PdSe<sub>2</sub> nanosheets on the substrate with lithographed metal marks. **b, c** Optical micrographs of PdSe<sub>2</sub> flakes at different regions. **d, e** Atomic force microscopy images of PdSe<sub>2</sub> samples from the region at the panel **c** and its inset. Reprinted with permission from Ref. [15]. Copyright 2017, American Chemistry Society. **f** Optical microscopy images of the PdSe<sub>2</sub> flakes with different layers. Reprinted with permission from Ref. [39]. Copyright 2020, American Chemistry Society

Here, Se powder was placed in Zone 1 at a temperature of 250 °C, and PdCl<sub>2</sub> powder was placed in Zone 2 at a temperature of 500 °C. Then, Se and Pd precursors were

transported by Ar/H<sub>2</sub> to Zone 3, and the temperature was maintained at 600 °C, at which the polycrystalline PdSe<sub>2</sub> films were synthesized continuously on the substrate.

**Table 3** Different types of PdSe<sub>2</sub> from the various synthesis approaches. These scheme were drawn by the authors, which were inspired by the literatures, i.e., bulk [17], flake [42], nanosheet [137], large domain [27] and 2D film [138]

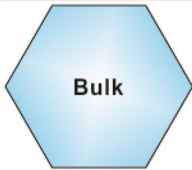

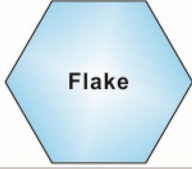
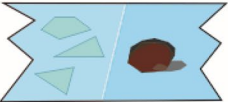
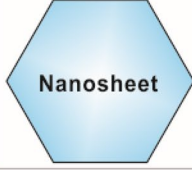
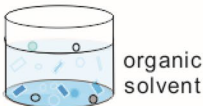
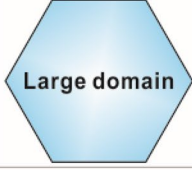
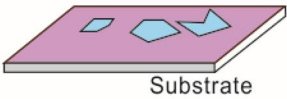

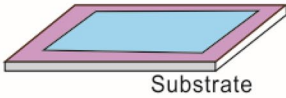
Type	Methods	Features
 Bulk	Chemical vapor transport 	<ul style="list-style-type: none"> <li>• Single crystal</li> <li>• Sub-1 cm size</li> <li>• Good homogeneity</li> </ul>
 Flake	Mechanical exfoliation 	<ul style="list-style-type: none"> <li>• Single crystal</li> <li>• Micrometer size</li> </ul>
 Nanosheet	Hydrothermal  organic solvent	<ul style="list-style-type: none"> <li>• Nanocrystal</li> <li>• Good electrochemical performances</li> </ul>
 Large domain	Chemical vapor deposition  Substrate	<ul style="list-style-type: none"> <li>• Single crystal</li> <li>• Good electronic transport</li> </ul>
 Full coverage film	Metal sputtering and selenization  Substrate	<ul style="list-style-type: none"> <li>• Polycrystal</li> <li>• Mass production</li> <li>• Flexibility</li> </ul>

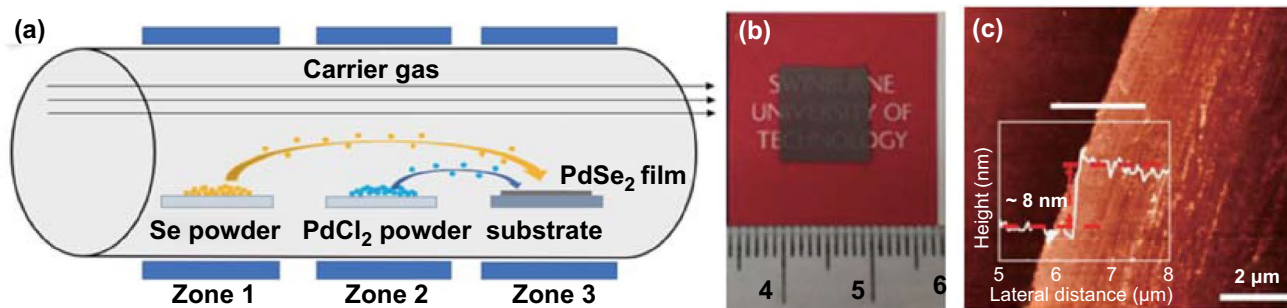
Figure 12b shows a photograph of the as-grown PdSe<sub>2</sub> film with high uniformity. The AFM image and height profile of the PdSe<sub>2</sub> films were characterized (Fig. 12c) with a thickness of ~8 nm, corresponding to 20 layers of PdSe<sub>2</sub> [15].

Because of the high melting point of the Pd metal precursor, the molten salt-assisted method can be utilized for the growth of PdSe<sub>2</sub> flakes, which can be synthesized at a lower temperature over a large domain [61]. The ambient pressure chemical vapor deposition (APCVD) method can be used with the assistance of salt powder, such as NaCl, where the Pd metal precursor is replaced by high-purity PdCl<sub>2</sub> powder. Au foils were placed above the mixture and heated at 850–900 °C at 85 sccm Ar and 15 sccm H<sub>2</sub> flows for 10–15 min. Interestingly, the length/width ratio of the PdSe<sub>2</sub> flakes increased markedly during the synthesis. PdSe<sub>2</sub> flakes were obtained with growth times of 20 and 35 min, respectively. The PdSe<sub>2</sub>

flakes on Au foil exhibited a ribbon-like shape, which was rarely the case on the amorphous oxide substrates. Hence, the synthesis of PdSe<sub>2</sub> may depend on its anisotropic structure and orthorhombic symmetry.

### 3.4 Chemical Vapor Deposition Reaction by the Sublimated Pd and Se

A CVD approach has been developed with the reaction of sublimated Pd and Se for growing few-layer PdSe<sub>2</sub> flakes with high crystallinity [62]. In the setup for the synthesis of PdSe<sub>2</sub> crystals, the Se powder was placed in a separate quartz tube zone wrapped with a heating belt at 350 °C, while Pd powder was located in the center of the furnace at 800 °C, with an Ar flow of 50–150 sccm for 10–20 min. Meanwhile, the substrate was placed in the downstream zone



**Fig. 12** **a** Schematic of PdSe<sub>2</sub> synthesis process using CVD method. **b, c** Photograph and AFM height profile of a prepared multilayer PdSe<sub>2</sub> film. Reprinted with permission from Ref. [60]. Copyright 2020, American Chemical Society

outside the heating zone at 480–600 °C. The scheme of the growth method is presented in Fig. 13.

Notably, the PdSe<sub>2</sub> flakes had various thicknesses, sizes, and shapes when the substrates were synthesized at different temperatures. For example, square-like flakes grown at 600 °C are thicker and larger than the heart-like flakes grown at a temperature of 500 °C.

Chemical vapor deposition has been employed for synthesizing large-area PdSe<sub>2</sub> films [16], single-crystal domains [63], nanowires [48], and ribbons [64]. Wafer-scale single-crystal PdSe<sub>2</sub> may be necessary for integrated circuit applications.

### 3.5 Selenization of Pd Film

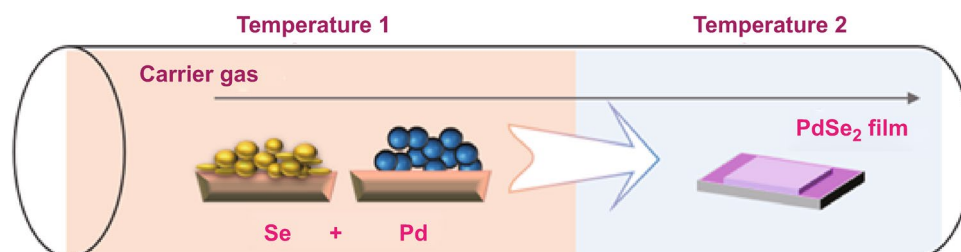
A simple selenization method leads to the synthesis of noble metal diselenide films [65]. The synthesis of PdSe<sub>2</sub> films by direct selenization and the thickness of PdSe<sub>2</sub> can be well controlled by varying the thickness of the deposited Pd layer [62]. The Pd layer deposited on the substrate via magnetron sputtering was placed in the center zone of the tube furnace at 480 °C, while the high-purity Se powder (99.99%) was placed

in the upstream zone at 220 °C under a 60-sccm Ar flow for 90 min. The selenization strategy could enable the wafer-scale growth of PdSe<sub>2</sub>, such as in the form of a 2-inch PdSe<sub>2</sub> film over a Si wafer [62]. The Raman mapping of the PdSe<sub>2</sub> film proves that the PdSe<sub>2</sub> film possesses good uniformity.

The structure–property relationship is listed in Table 4. The advantages and disadvantages are compared for different synthesis approaches for obtaining PdSe<sub>2</sub>. Future opportunities lie in the synthesis of monolayer single-crystal PdSe<sub>2</sub> full film over a wafer scale (yet shown).

### 3.6 Direct van der Waals Epitaxial Growth of PdSe<sub>2</sub> on Graphene

The PdSe<sub>2</sub> has been deposited over the support of graphene or MoS<sub>2</sub> in an epitaxial growth fashion [22]. The precursor of Pd containing organic molecules has been employed for the formation of PdSe<sub>2</sub>. Figure 14a illustrates a schematic of the experimental process. The van der Waals heterostructure of PdSe<sub>2</sub>/graphene can be directly grown with this method.



**Fig. 13** The chemical vapor deposition synthesis of the PdSe<sub>2</sub> film. The Se powder and Pd metal are sublimated in temperature 1 and deposited at temperature 2 for 2D film synthesis. The concept was inspired by Ref. [62]. The scheme is originally drawn by the authors of the review

**Table 4** Comparison of the types of PdSe<sub>2</sub> from different methods

Methods	Structure quality	Types	Thickness (nm)	Average domain size (µm)	Mobility (cm <sup>2</sup> V <sup>-1</sup> s <sup>-1</sup> )	Advantages	Disadvantages	References
Mechanical exfoliation	Single crystal	Flake	0.6 – 2.4	30	158	High crystalline quality; micrometer-scale grain size;	Not compatible with mass production; irregular shape; inhomogeneity in thickness	[15]
Mechanical exfoliation	Single crystal		6.8 – 116	5 – 10	130 (at 300 K) and 520 (at 77 K)	High quality from CVD-derived PdSe <sub>2</sub> bulk material	Large time cost; large human resource cost for repeating the exfoliation by human hands;	[139]
CVD from PdCl <sub>2</sub>	Nanocrystal	Film	8	From 0.01 to 0.1	n.a	Centimeter-scale film growth; industrial mass production potential;	Small grain size	[60]
CVD from Pd powder over Si/SiO <sub>2</sub> substrate	Nanocrystal	Film	3 – 12	From 3 to 5	294	Large-scale production promise		[16]
CVD over sapphire and mica substrate	Single crystal	Square domain	1.2 – 2.4 (2 L and 4 L)	5 – 10 (sapphire); 5 – 10 (mica);	n.a	High crystalline quality;	Fragile sapphire substrate; Not tolerant with fast cooling after CVD growth	[16]
CVD over Au substrate	Single crystal	Large domain	1.2 (bilayer)	200 µm long and 2 µm wide strip;	n.a	Large lateral grain size;	Expensive Au substrate	[16]
Metal film plus selenization	Nanocrystal	Film	1.2 – 20	From 0.03 to 0.05	n.a	Simple process; wafer-scale production	Small grain size; nanocrystalline; low crystalline quality;	[62]
Pd dimer and selenization over epitaxial substrates	Nanocrystal	Flake	5	From 0.005 to 0.01	n.a	Large single crystal	Small grain size; small-scale; irregular shape	[22]
Thinning of PdSe <sub>2</sub> flakes by etching	Single crystal	Flake	n.a	3	n.a	Regulating the layer number of PdSe <sub>2</sub> ; modulating the physical properties of PdSe <sub>2</sub> ;	The grain size depending on the pristine PdSe <sub>2</sub> material;	[66]

**Table 4** (continued)

Methods	Structure quality	Types	Thickness (nm)	Average domain size ( $\mu\text{m}$ )	Mobility ( $\text{cm}^2 \text{V}^{-1} \text{s}^{-1}$ )	Advantages	Disadvantages	References
Ideal CVD (to be investigated)	Single crystal	Film	0.6 (monolayer)	Beyond 100 $\mu\text{m}$ [139]	> 1000 (theoretical limit) [17, 19, 27]	Mass production potential; wafer-scale production; High-quality single crystal	n.a	To be announced

Graphene was suspended on top of the observation membrane by drop-casting the same volume of dispersion onto a TEM grid. The graphene was transferred onto a  $0.50 \times 0.50 \text{ mm}^2$   $\text{SiN}_x$  membrane, which has 2- $\mu\text{m}$  vacuum pinholes spaced 5  $\mu\text{m}$  apart.

Figure 14b shows the CVD system for the selenization of  $\text{PdSe}_2$ . The two-zone furnace was compiled with the temperature profile for Zone 1 at 240  $^\circ\text{C}$  and Zone 2 at 360  $^\circ\text{C}$  (Fig. 14c). This research presents a direct method for the growth of vdWHs at the nanoscale and atomic level and an innovative strategy for the synthesis of 2D materials through predetermined nucleation.

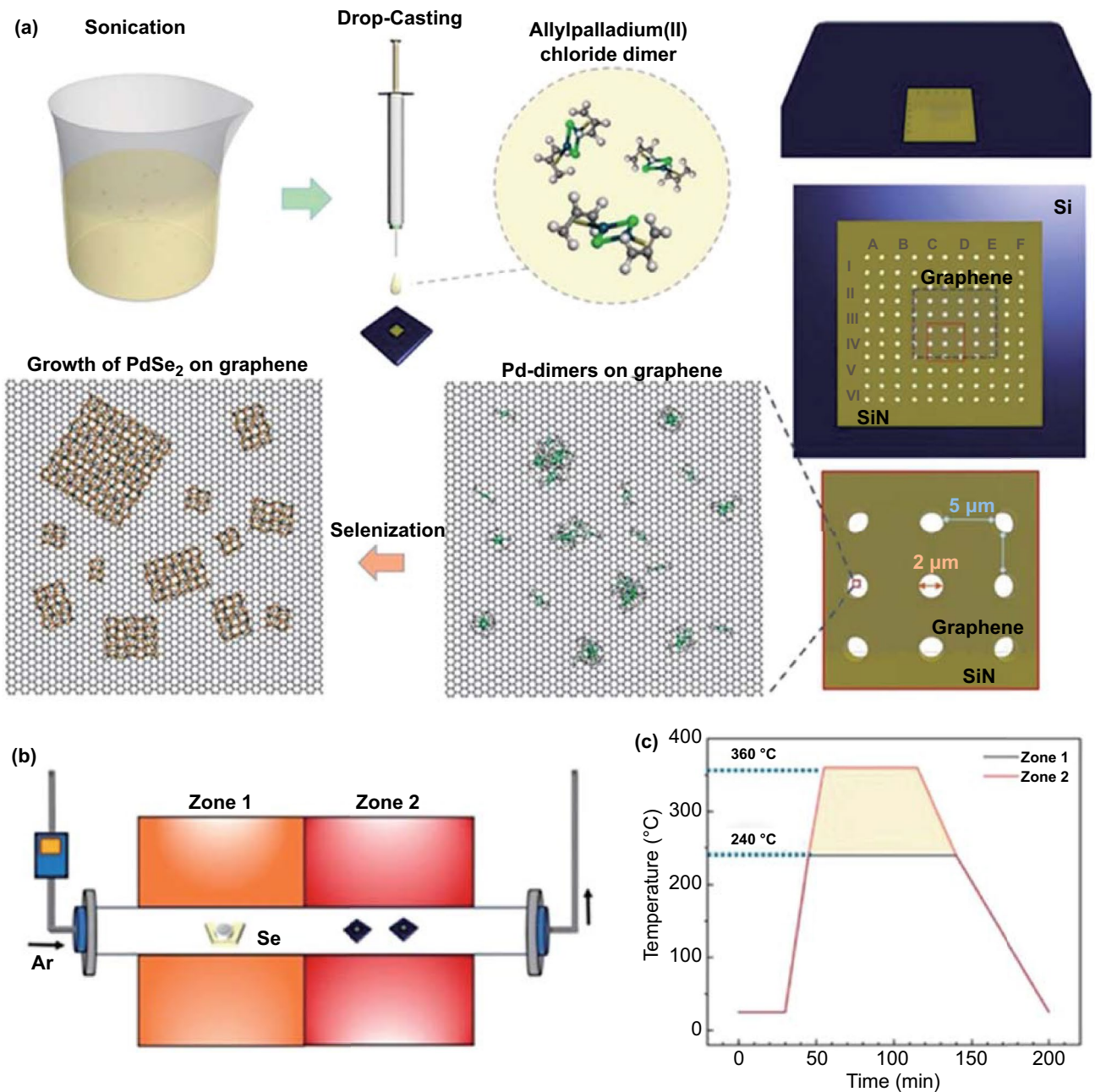
### 3.7 Layer-by-layer Thinning by the Oxygen Plasma

Precise layer control of  $\text{PdSe}_2$  samples plays an important role in tuning of the bandgap of  $\text{PdSe}_2$ . A layer-by-layer thinning strategy has been employed for etching an  $n$ -layered  $\text{PdSe}_2$  flake to the  $(n - 1)$  layered flake (Fig. 15). Precise layer thinning [66] has been depicted by selective oxidation via oxygen plasma and sublimation through thermal annealing (Fig. 15a-d).

To investigate the etching method, the  $\text{PdSe}_2$  flakes were exposed to plasma with different  $\text{O}_2/\text{Ar}$  ratios [66]. Figure 15e shows the variation in the thickness of the  $\text{PdSe}_2$  flakes after etching. The correlation between the thickness and number of layers employs an empirical value of 0.7 nm per  $\text{PdSe}_2$  layer [15]. Figure 15f shows an optical micrograph of two pristine  $\text{PdSe}_2$  flakes with seven and nine layers, respectively. Figure 15g shows the same regions after the plasma etch cycle. The color of the  $\text{PdSe}_2$  species changes subtly from blue to light purple, which indicates a decrease in the  $\text{PdSe}_2$  film thickness.

The AFM images of the corresponding  $\text{PdSe}_2$  flakes (Fig. 15h, i) provide line-scanning information (Fig. 15j). Here, 2-nm  $\text{PdSe}_2$  (ca. 3 layers) was etched after oxidation and sublimation upon  $\text{O}_2$  plasma treatment. Therefore, plasma etching and surface curing may shed light upon the bandgap regulation of 2D materials over a large area.

The posttreatment of  $\text{PdSe}_2$  could modify the structure and properties of the pristine material. First, mild plasma exposure to  $\text{PdSe}_2$  could lead to layer-by-layer plasma etching to regulate the thickness [66]. The ozone treatment [67]

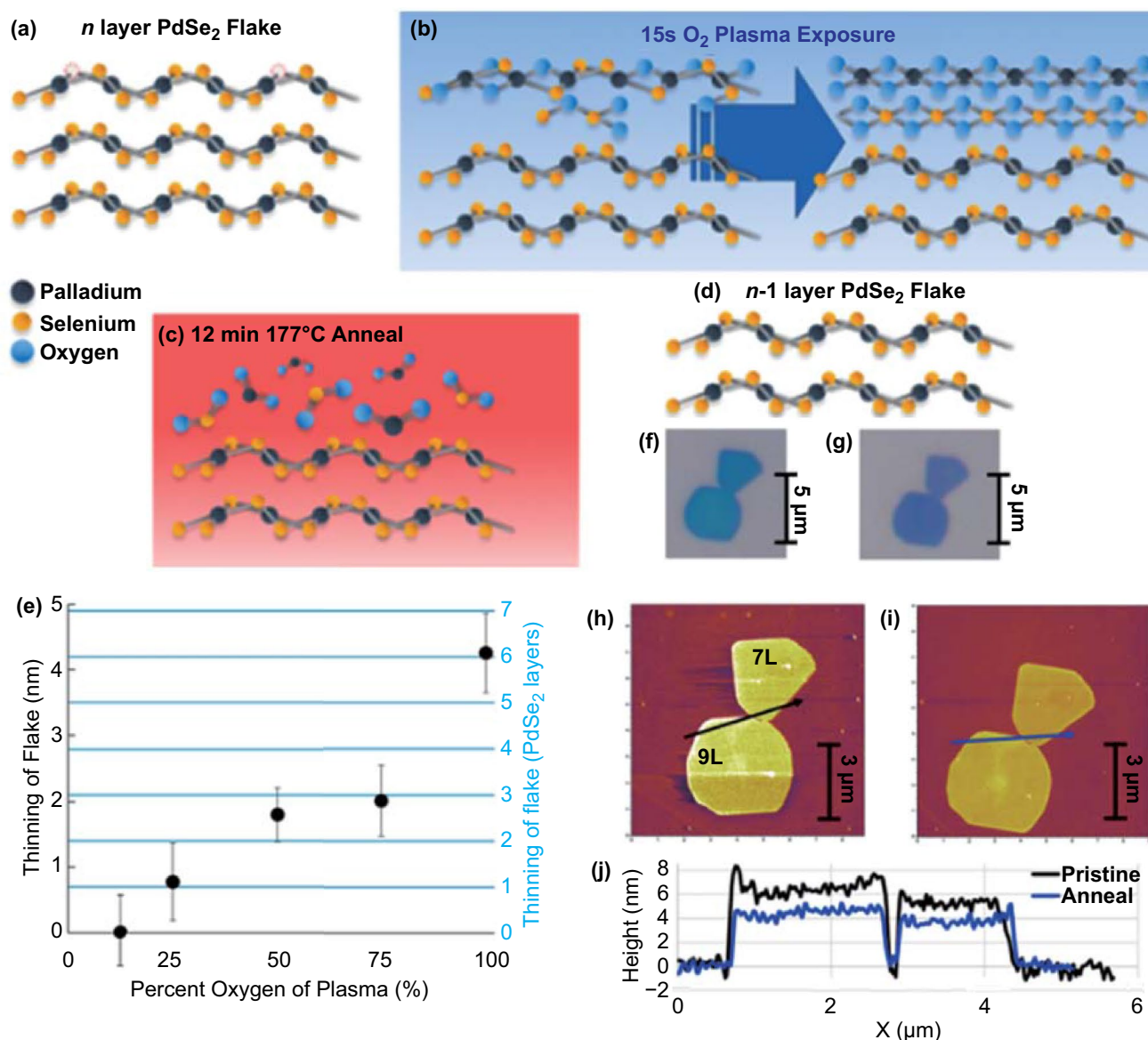


**Fig. 14** Growth of PdSe<sub>2</sub> over graphene with selenization of Pd dimers as precursors. **a** Schematic of protocol for PdSe<sub>2</sub> synthesis. **b** Schematic of two-zone horizontal furnace for thermal treatment under Se-rich atmosphere. **c** Temperature distribution along with tube furnace. Reprinted with permission from Ref. [22]. Copyright 2020, American Chemical Society

of PdSe<sub>2</sub> could enhance the chemical sensitivity owing to the weak oxidation. Electron irradiation can modify conductivity performance [68]. The phase transformation of PdSe<sub>2</sub> leads to a sub-1-nm channel by thermal treatment [49] and the Pd<sub>2</sub>Se<sub>3</sub> phase by interlayer fusion [46].

#### 4 Roles in Electronic Devices

As mentioned above, because of the strong interlayer interactions resulting from the almost fully occupied *d*-orbital and tunable properties, which depend on the number of



**Fig. 15** Thinning of PdSe<sub>2</sub> layers with plasma treatment. **a** Pristine PdSe<sub>2</sub> flakes. **b** Oxygen plasma etching. **c** Thermal annealing. **d** Resultant PdSe<sub>2</sub> after layer thinning. **e** Etching of layers versus the oxygen percentage in the plasma. Optical micrographs of PdSe<sub>2</sub> **f** before plasma etching and **g** after plasma thinning. Atomic force microscope micrographs of PdSe<sub>2</sub> flakes before **h** and after **i** layer thinning. **j** Height profiles from two lines extracted from panel **h** and panel **i**. Reprinted with permission from Ref. [66]. Copyright 2020, American Chemical Society

layers, PdSe<sub>2</sub> shows potential as a 2D material applicable for use in electronic devices.

#### 4.1 Electrical Contacts for PdSe<sub>2</sub> Devices

Prior to fabrication of an electric device, a metal/PdSe<sub>2</sub> contact is essential for optimizing the electrical performance of transistors, photodetectors, and integrated

circuits. At the interface of metal/semiconductor contact, the transport properties of charge carriers are determined by the Schottky height, tunneling energy barrier, orbital overlapping percentage, as well as the geometry of the interface.

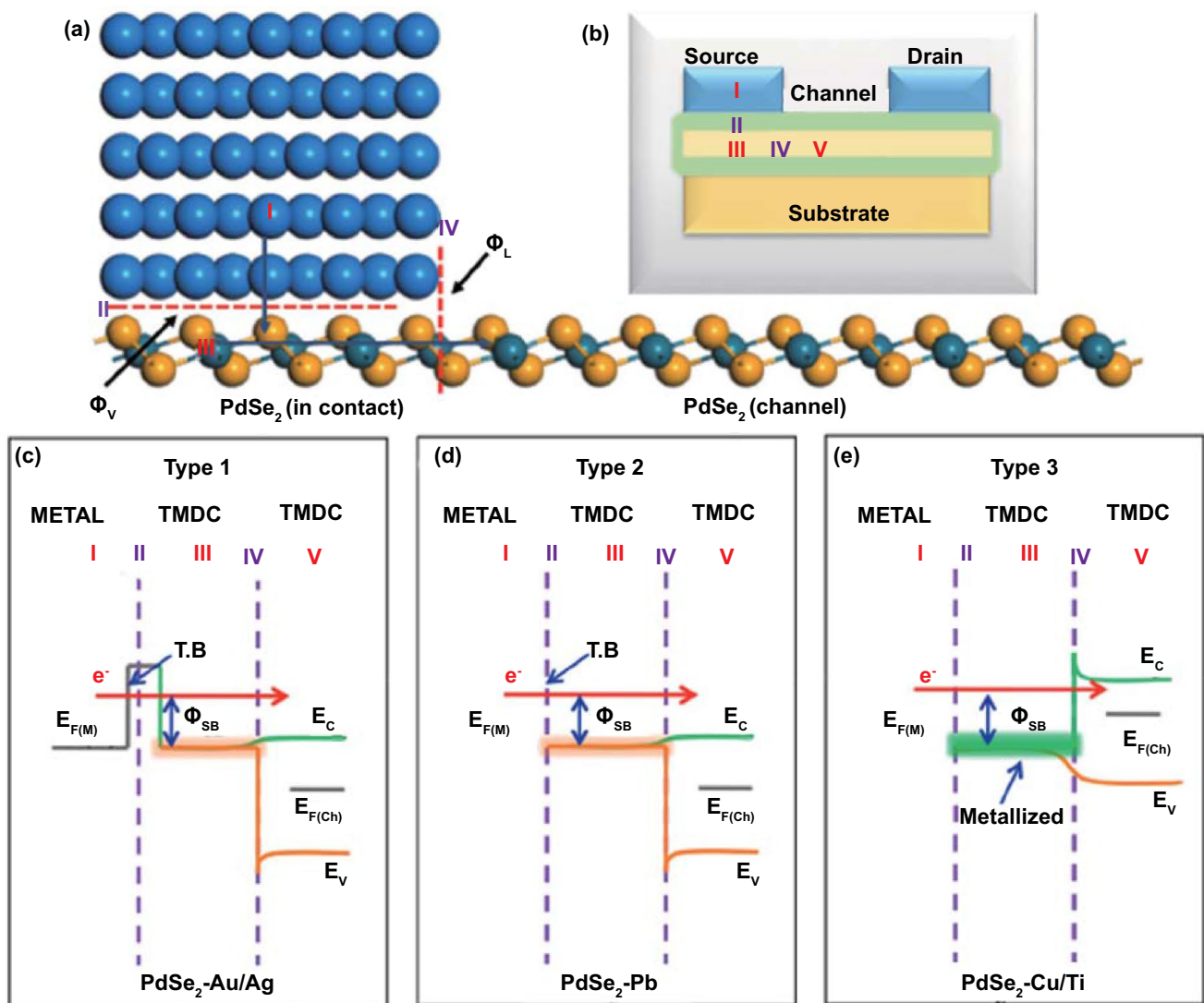
Theoretical calculations using the DFT approach were employed to compare the metal/PdSe<sub>2</sub> contact performances by tuning the metal types such as Au, Ag, Pb, Cu, and Ti, as well as semimetallic graphene. The efficiency of



charge transfer at the PdSe<sub>2</sub>-metal interface was examined for energy barrier evaluation [69]. Figure 16a shows the prototype of a PdSe<sub>2</sub>-metal contact with a carrier flowing from the metal electrode to the PdSe<sub>2</sub> channel through the pathway (I → II → III → IV → V). In a typical PdSe<sub>2</sub> FET (Fig. 16b), carriers diffuse from the metal to the layered PdSe<sub>2</sub> and encounter a tunneling barrier, which depends on the binding strength at the interface of the PdSe<sub>2</sub>-metal contact.

The PdSe<sub>2</sub>-metal contacts, i.e., with Au or Ag electrodes, are demonstrated with their energy band alignment based on

the binding energy owing to the Schottky barriers (Fig. 16c). First, Au/PdSe<sub>2</sub> was preferred via compression of the Schottky barrier height. Meanwhile, the Ag electrodes led to an improved orbital overlap with PdSe<sub>2</sub>. A vertical Schottky barrier appears at the interface (II) in the vertical direction, while a lateral Schottky barrier occurs at the interface (IV) between the heterojunction and the PdSe<sub>2</sub> channel region. Second, the Pb/PdSe<sub>2</sub> contact has a low tunneling potential with a Schottky barrier height of 0.67 eV (Fig. 16d). Third, Cu/PdSe<sub>2</sub> does not form a tunneling interface (Fig. 16e) but has a Schottky height of 0.58 eV.



**Fig. 16** Metal/PdSe<sub>2</sub> contact, transistor configuration, and their band alignment. **a** Atomic configuration of PdSe<sub>2</sub>-metal contact. The pathway of electron flows is coordinated from the metal electrode to the metal/PdSe<sub>2</sub> interface and then to the PdSe<sub>2</sub> channel. **b** Schematic of typical PdSe<sub>2</sub> field-effect transistor. The labeling is identical for the five panels of I, II, III, to IV and V. Energy band alignment of different PdSe<sub>2</sub>-metal contacts based on tunneling evaluation and Schottky barriers with **c** weak bonding by Au/Ag, **d** medium bonding with Pb, and **e** strong bonding by Cu/Ti interface. “T.B.” denotes the tunneling barrier. Reprinted with permission from Ref. [69]. Copyright 2020, American Chemical Society

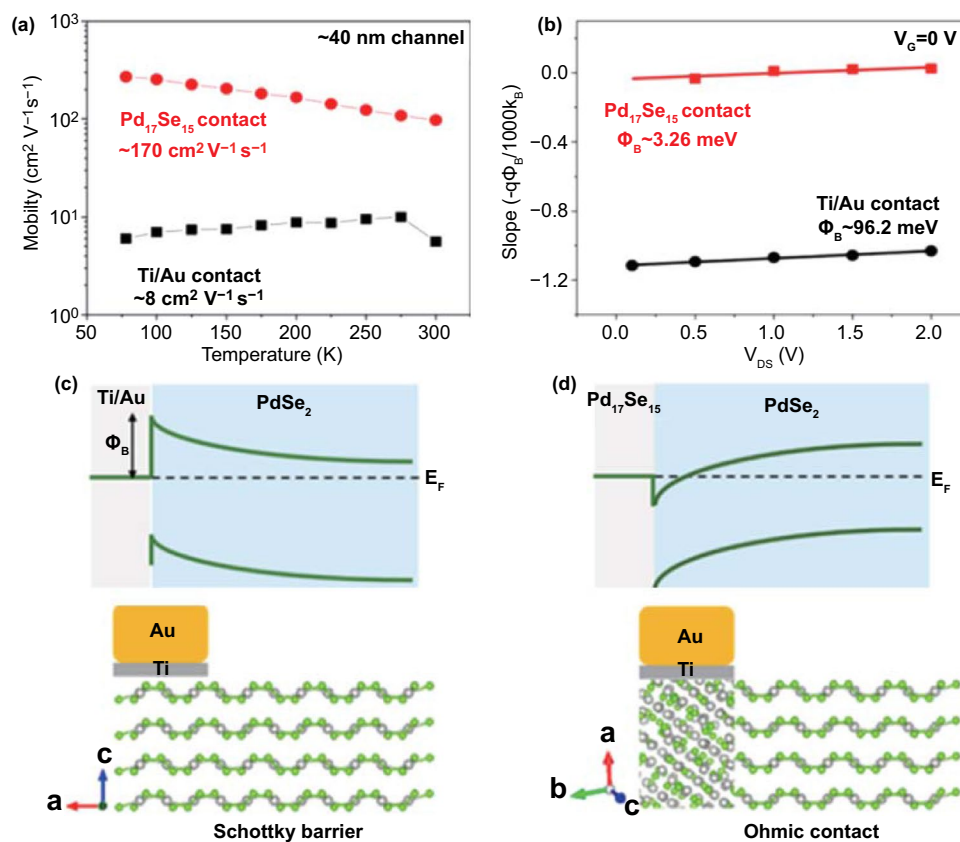
Eventually, the graphene/PdSe<sub>2</sub> contact has emerged as a proof of concept with regard to vdWHs. A Schottky barrier height of 0.22 eV is preferred for electron transport—that is, *n*-type charge carrier conductance [69]. Indeed, electrons are transferred from the interface to the PdSe<sub>2</sub> side with a band bending of  $-0.94$ . The weak van der Waals interactions between graphene and PdSe<sub>2</sub> render a quasi-Ohmic contact without energy transfer between the two surfaces. That is, the intrinsic transport properties of PdSe<sub>2</sub> are maintained. Analogous to the contact behavior of other 2D materials, one can fabricate high-performance optoelectronic devices.

The stability and metallicity of the Pd<sub>17</sub>Se<sub>15</sub> phase make it an ideal buffering material between the metal and PdSe<sub>2</sub>. The low lattice mismatch between both palladium selenides guarantees quasi-Ohmic conductance behavior, which suppresses the Schottky barrier height. In contrast, PdSe<sub>2</sub> devices with Pd<sub>17</sub>Se<sub>15</sub> contacts performed better than those with Ti/Au contacts [52]. Figure 17a shows the temperature-dependent

mobility of PdSe<sub>2</sub> devices with Pd<sub>17</sub>Se<sub>15</sub> contacts and Ti/Au contacts, which are approximately 170 and 8 cm<sup>2</sup> V<sup>-1</sup> s<sup>-1</sup>, respectively.

Figure 17b shows the relationship between the slope and different drain voltages at zero gate voltage. The Schottky barrier height  $\Phi_B$  of the Ti/Au contact device (96.2 meV) is greater than that of the Pd<sub>17</sub>Se<sub>15</sub> contact device (3.26 meV). Figure 17c, d illustrates the electrode contact of the PdSe<sub>2</sub> devices from the Schottky barrier of Ti/Au contacts to the Ohmic contact of Pd<sub>17</sub>Se<sub>15</sub> contacts. Thus, the contact resistance of the PdSe<sub>2</sub> device decreases and has the potential to become closer to the quantum limit.

Future opportunities may remain in developing the electrical contacts of PdSe<sub>2</sub> with other palladium selenides. Indeed, the PdSe<sub>2-x</sub> phases with different stoichiometric ratio may arouse different contact behaviors when stacking vertically with PdSe<sub>2</sub> or stitching together laterally. The PdSe<sub>2-x</sub>/PdSe<sub>2</sub> contact could be either Ohmic or Schottky



**Fig. 17** Metal/PdSe<sub>2</sub> contact for regulating the electronic transports. **a** Comparison of temperature-dependent mobility of the PdSe<sub>2</sub> channel with Ti/Au and Pd<sub>17</sub>Se<sub>15</sub> contacts, respectively. **b** Comparison of  $V_{DS}$ -dependent Schottky barrier height of PdSe<sub>2</sub> devices with Ti/Au and Pd<sub>17</sub>Se<sub>15</sub> contacts, respectively. Schematic of **c** Ti/Au contact and **d** Pd<sub>17</sub>Se<sub>15</sub> contact. Reprinted with permission from Ref. [52]. Copyright 2019, American Chemistry Society

typed, which require the optimization of researchers. The Schottky type contact could be utilized in the rectifier device. The Ohmic contact facilitates the electronic transport performances such as charge carrier mobility. The phase-engineering method proves that new crystal-line phases of anisotropic 2D materials can be induced by defects. These new PdSe<sub>2-x</sub> compounds may have different stoichiometries, which broadens the choices of materials for electrical contacts.

After understanding the metal/PdSe<sub>2</sub> contact, we now come to the discussion of electronic transport performances in field-effect transistors.

## 4.2 PdSe<sub>2</sub> Field-effect Transistors

The field-effect transistors are one of the most significant devices in semiconductor electronics, and FETs based on 2D materials have shown superior performance to those based on traditional semiconductors. Moreover, usage of 2D materials provides new opportunities and effective approaches regarding FETs, with a high on/off ratio, high carrier mobility, and excellent stability. The layer-dependent properties of TMDCs are important for the design of FETs for diverse functionalized devices [30]. In this section, PdSe<sub>2</sub> FETs and efficient methods to improve their performance are introduced.

PdSe<sub>2</sub> has proven to be a successful channel material for FETs. PdSe<sub>2</sub> transistors have achieved high mobility with tunable ambipolar characteristics [70]. Figure 18a shows an experimental setup to measure the PdSe<sub>2</sub> FET characteristics with *p*-type Si as a universal back-gate electrode, and Fig. 18b, c shows SEM images of the two as-fabricated PdSe<sub>2</sub> FET samples.

The electronic performances of the PdSe<sub>2</sub> FETs are depicted in the output and transfer characteristics (Fig. 18d, e). In the output curves, the PdSe<sub>2</sub> FET exhibited a linear correlation between the voltage and current (insets of Fig. 18d, e). Such a linear drain current–voltage dependence indicates quasi-Ohmic contact, i.e., suppression of the Schottky barrier between PdSe<sub>2</sub> and the electrodes. The electrons dominate the primary charge carriers of the FET at a positive gate voltage and a small negative gate voltage (Fig. 18f). In contrast, the holes become the leading charge carriers of the FET at a large negative gate voltage.

The air stability of PdSe<sub>2</sub> guarantees the lifetime of its transistor-based sensor applications in a wet environment.

For example, the 2D material-based transistors have been embedded in a microfluidic chip for microRNA detection and screening [71]. The chemical sensors of 2D materials have demonstrated superior performances.

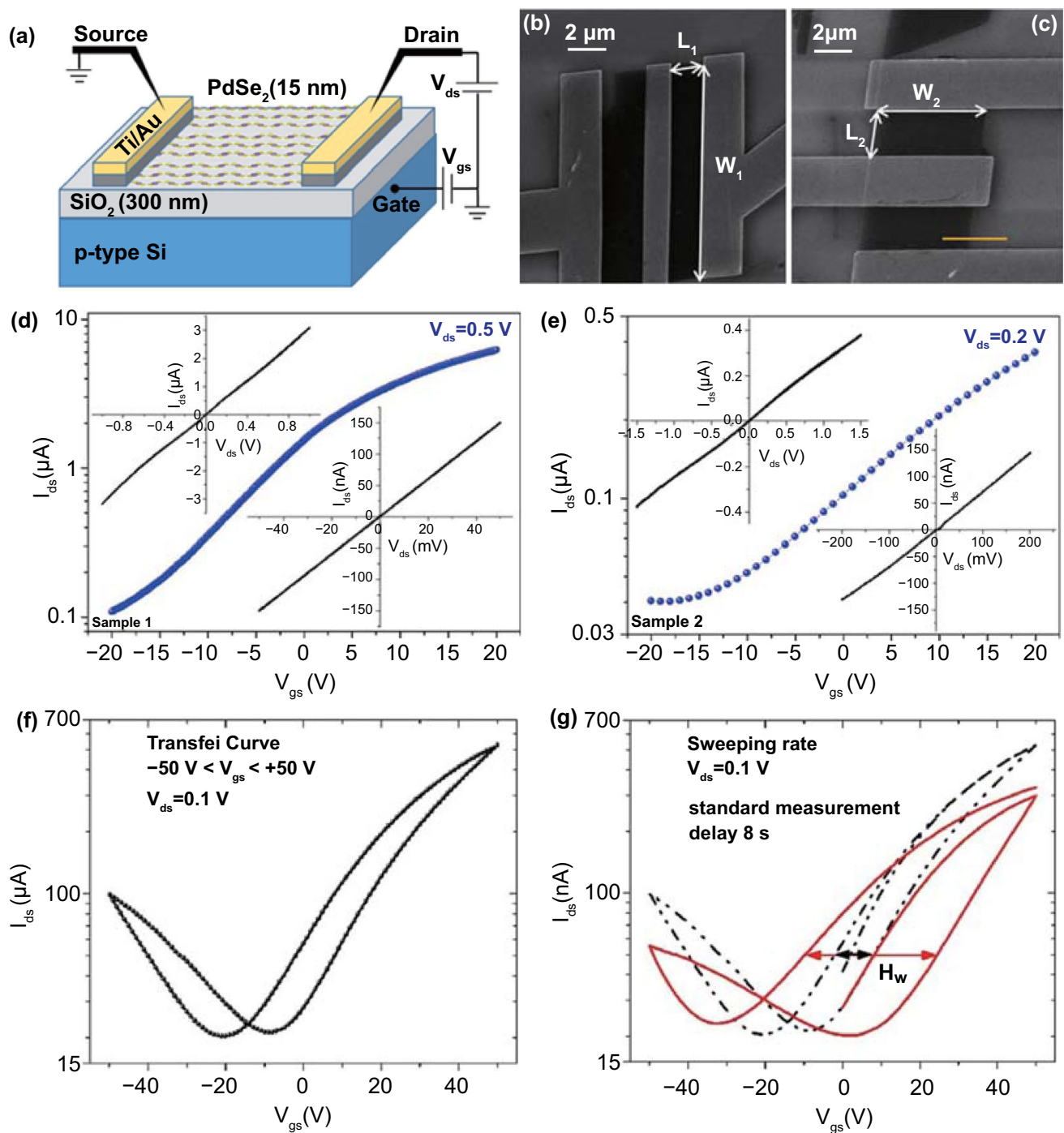
The slight hysteresis of the transfer curve could result from the effect of slow trap states and the surface adsorbates from the lithography-based fabrication process [17]. Remarkably, the ambipolar behavior of the PdSe<sub>2</sub> FET could be regulated through a biased sweep.

The hysteresis width can be periodically evaluated by continuously measuring several transfer curves. These two transfer curves of the PdSe<sub>2</sub> FET were measured in succession (Fig. 18g). The first curve in black was employed as a reference curve, and the second curve in red was collected at a delay of 8 s after the first signal capture. Therefore, the hysteresis is elevated with the increased sweeping time of the gate voltage.

The transport properties of PdSe<sub>2</sub> FETs can be regulated by employing vacuum annealing, charge doping, electrical stress, pressure, and electron irradiation [17]. Through reduction of both the pressure and electron irradiation, hysteresis in the PdSe<sub>2</sub> FET can be effectively suppressed. These strategies offer viable methods to reduce hysteresis in devices. Moreover, the types of charge carriers can be converted from *n*-type to *p*-type, which can be used as a switch for practical circuits.

Remarkably, vacuum annealing is an effective method for improving the mobility of FETs, and it has been widely used in electronic devices [72]. For PdSe<sub>2</sub> FETs, annealing can remove the surface adsorbates to achieve higher mobility, on/off ratio, and lower Schottky barrier. Moreover, annealing at 450 K can eliminate hysteresis in FETs [17]. After annealing at 400 and 450 K, PdSe<sub>2</sub> FET exhibits a higher mobility of 75 and 216 cm<sup>2</sup> V<sup>-1</sup> s<sup>-1</sup> than that measured at room temperature. Such a transistor achieves the highest current ON/OFF ratio of 10<sup>3</sup> at 450 K. Meanwhile, the threshold voltage shows an increasing shift to the negative gate voltage as the annealing temperature increases. This indicates that the Fermi level moved to the conduction band in PdSe<sub>2</sub>. Thus, the PdSe<sub>2</sub> FET exhibits an obvious *n*-type transfer characteristic.

Furthermore, a molecular doping method converts the electron transport behavior of PdSe<sub>2</sub> into a hole-transport feature [17]. As a prevalent *p*-dopant, F4-TCNQ has high electron affinity and has been utilized in low-dimensional materials



**Fig. 18** Demonstration and performance of PdSe<sub>2</sub> FET. **a** Schematic of PdSe<sub>2</sub> field-effect transistor and electrical measurements. **b, c** SEM micrographs of two devices with source and drain electrodes fabricated on 15-nm-thick PdSe<sub>2</sub> flakes. Channel length and width vary in both transistors. **d, e** Transfer characteristics of PdSe<sub>2</sub> FETs corresponding to **b, c**. Insets are the drain current versus voltage, i. e., the output characteristics of the PdSe<sub>2</sub> transistor at the high bias voltage (top left) and low bias voltage (bottom right). **f** The transfer curves of the PdSe<sub>2</sub> FETs measured at vacuum conditions of 10<sup>-6</sup> mbar. **g** Comparison of the transfer curves in panel **f** with the curves measured after a delay of 8 s relative to the standard measurement time in panel **f**. The H<sub>w</sub> denotes the hysteresis width. Reprinted with permission from Ref.[74]. Copyright 2019, Elsevier Ltd

[73], which can be applied to PdSe<sub>2</sub>. One can compare the transfer curves of the FET with different doping levels from undoped to completely doped, whereby a distinct conversion of the transfer characteristics from ambipolar to *p*-type is shown. The contact resistance of the PdSe<sub>2</sub> FET has a dependence on the gate voltage, resulting from the Fermi level being adjusted by electrostatic gating. Therefore, vacuum annealing and molecular doping can effectively reduce contact resistance.

The transport properties of PdSe<sub>2</sub> FETs can be altered via annealing or charge doping. Besides, the ambipolar behavior of PdSe<sub>2</sub> FETs can be obtained by varying the electrical stress, pressure, and electron irradiation [70].

Atmospheric pressure has a significant influence on the PdSe<sub>2</sub> FET. The transfer curves of the PdSe<sub>2</sub> FET were extracted under various pressures at a constant drain voltage of 100 mV. As the pressure increases, the transfer nature of the PdSe<sub>2</sub> FET gradually transforms from the *n*-type to the *p*-type, and the PdSe<sub>2</sub> FET exposed to air after 10 min becomes a *p*-type depletion mode transistor [70].

Moreover, electron irradiation changes the charge distribution in the PdSe<sub>2</sub> FET, which further affects the transfer characteristics [74]. The transfer curves of the PdSe<sub>2</sub> FETs were collected before and after electron irradiation via SEM imaging. With increasing time after SEM imaging, the transfer characteristics slowly revert to the initial state.

Two-dimensional PdSe<sub>2</sub> synthesized using different approaches has been used in the fabrication of FETs.

Table 5 compares the performance of these PdSe<sub>2</sub> FETs in terms of charge carrier mobility and current ON/OFF ratio. Further developments with large-area CVD-grown PdSe<sub>2</sub> may improve the electrical performance, such as the charge mobility and ON/OFF ratio.

In summary, several strategies have been developed to improve the FET performance of PdSe<sub>2</sub>. Future opportunities still exist in terms of surface cleaning and modification, electrode contact design, packaging conditions, and vdWH stacking. Indeed, the PdSe<sub>2</sub>-based electronic devices could be integrated with the piezoelectric materials, i.e., PVDF for tactile sensors [75]. For the comfort of human beings, stretchable and wearable electronics become emerging with device development such as strain sensors and electronic skin [76]. Besides, the introduction of triboelectric nanogenerators, supercapacitors [77], and batteries [78] may lead to self-powered sensors [79].

After knowing the electronic devices of PdSe<sub>2</sub>, we turn to the progress in its applications in optoelectronics and optics.

## 5 PdSe<sub>2</sub> for Optoelectronics and Optics

The photodetector, which is a device that converts an optical signal into an electrical signal instantaneously, plays an indispensable role in current and burgeoning technology, in

**Table 5** The performances of field-effect transistors based on PdSe<sub>2</sub> obtained from different methods

Synthesis methods and PdSe <sub>2</sub> types	Electrode types	Charge mobility (cm <sup>2</sup> V <sup>-1</sup> s <sup>-1</sup> )	Current ON/OFF ratio	References
CVD (Domains)	Cr/Au	294	10 <sup>3</sup>	[16]
Exfoliated (flake)	Ti/Au	158	10 <sup>6</sup>	[15]
CVD (Domains)	Ti/Au	6.4	> 10 <sup>6</sup>	[63]
Exfoliated (flake)	Ti/Au	4	10 <sup>4</sup>	[19]
Exfoliated (flake)	Pd/Au	20	10 <sup>2</sup>	[81]
Exfoliated (flake)	Pd <sub>17</sub> Se <sub>15</sub> /Ti/Au	170	n.a	[52]
Exfoliated (flake)	Ti/Au	8	n.a	[52]
Exfoliated (flake)	Ti/Au	216	10 <sup>3</sup>	[17]
CVD (domains)	Cr/Au	n.a	10 <sup>3</sup>	[140]
Exfoliated (flake)	Ti/Au	4	25	[70]
Exfoliated (flake)	Ti/Au	3	30	[74]
Exfoliated (flake)	Ti/Au	92	10 <sup>4</sup>	[41]
Exfoliated (flake)	Ti/Au	138.9	10 <sup>3</sup>	[54]



the fields of biotechnology, medicine, physics, and natural sciences [80].

Owing to their unique and significant properties, 2D materials have been applied in photodetectors and exhibit remarkable performance in terms of responsivity ( $R$ ), detectivity ( $D^*$ ), and external quantum efficiency (EQE) [81]. Here, the responsivity  $R$  describes the photoelectric conversion efficiency,  $D^*$  reflects the ability to measure the minimum optical signal, and EQE is the ratio of the number of photo-generated electron–hole pairs contributing to photocurrent to the number of the incident photons. The rise/fall time is a crucial parameter for evaluating the response speed of photodetectors.

Two-dimensional materials can be used as outstanding photodetector components by constructing heterojunctions [82] and gate-voltage regulated phototransistors [41]. For example, infrared photodetectors can employ the sensing materials such as BP [83], PtTe<sub>2</sub> [10], and WS<sub>2</sub>. But h-BN, graphene/Si [84], and MoS<sub>2</sub>/GaN [85] can be used for ultraviolet light detection. Besides, PtSe<sub>2</sub> has a large photoreponse at a wide spectral band ranging from 200 to 1550 nm [7]. Then, the anisotropic compounds such as PdSe<sub>2</sub> can be used for polarized sensitive photoelectric detection [29]. Therefore, the coupling of PdSe<sub>2</sub> and other 2D materials may cover the light detection of a broad spectral range.

In this section, we will discuss the detection band versus bandgap, photodetection performances, and polarized light detection based on PdSe<sub>2</sub> and related materials.

### 5.1 Detection Bands versus Bandgap

The performance of the photodetectors can be determined by the bandgaps of the materials. Photodetectors function at various wavelengths based on different 2D materials. Owing to the different bandgaps of the 2D materials, the corresponding photodetectors function in different spectral bands (Table 6).

The performances of 2D material-based photodetectors can be determined as per details, such as black phosphorene or black phosphorus, MoS<sub>2</sub>, MoSe<sub>2</sub>, WS<sub>2</sub>, WSe<sub>2</sub>, graphene, SnS, SnSe, SnS<sub>2</sub>, SnSe<sub>2</sub>[86], InSe, In<sub>2</sub>Se<sub>3</sub>, ReS<sub>2</sub>, black AsP, PtSe<sub>2</sub>, PtS<sub>2</sub>, and PdSe<sub>2</sub>.

The PdSe<sub>2</sub> layered material has remarkable optoelectronic properties, with a large bandgap tenability and extraordinary carrier mobility. The PdSe<sub>2</sub>-based devices are relatively stable and can be applied for photodetection from

**Table 6** Detection bands of photodetectors and bandgaps depending on the types of 2D materials

Material	Bandgap (eV)	References	Detection bands		References
PdSe <sub>2</sub>	0–1.3	[141]	532	1060	[19]
	0–1.43	[15]	n.a	1060	[41]
PtS <sub>2</sub>	0.25–1.6	[142]	500	n.a	[143]
	0.25–1.6	[144]	405	1550	[144]
PtSe <sub>2</sub>	0.3–1.2	[106]	632	10,000	[106]
	0–1.17	[142]	n.a	980	[11]
ReS <sub>2</sub>	1.5	[145]	633	n.a	[145]
	1.5	[146]	405	655	[146]
ReSe <sub>2</sub>	1.27	[147]	520	n.a	[147]
	1.2–1.3	[148]	n.a	808	[148]
InSe	1.26	[149]	254	850	[149]
	1.26	[150]	365	685	[150]
In <sub>2</sub> Se <sub>3</sub>	1.3	[151]	500	800	[152]
	1.3	[153]	300	1100	[153]
AsP	0.15–0.3	[105]	2360	8050	[105]
	0.1–0.3	[154]	980	n.a	[154]
SnS	1.0–1.2	[155]	400	1050	[155]
SnS <sub>2</sub>	2.1	[156]	457	633	[156]
SnSe	1.30–1.55	[155]	400	1400	[155]
SnSe <sub>2</sub>	1–2	[86]	300	2000	[86]
Graphene	0	[157]	n.a	1550	[157]
	0	[158]	285	1150	[159]
	0	[160]	630	10,000	[160]
WS <sub>2</sub>	1.4–2.1	[161]	365	650	[161]
	1.4–2	[162]	650	690	[163]
WSe <sub>2</sub>	1.63	[164]	500	900	[164]
	1.2	[165]	473	1550	[166]
MoS <sub>2</sub>	1.35–1.82	[167]	375	808	[168]
	1.65	[169]	532	1070	[169]
MoSe <sub>2</sub>	8.4–1.1	[170]	638	n.a	[170]
	1.1	[171]	n.a	785	[172]
Phosphorene	0.3	[173]	532	3390	[174]
	0.3	[175]	400	3800	[176]

deep ultraviolet to mid-infrared bands [21], and the longest photodetection wavelength studied thus far is 10.6  $\mu\text{m}$  [54].

### 5.2 PdSe<sub>2</sub> Photodetectors for Near-infrared Light Detection

The near-infrared light (1060 nm) is important for optical data communication and biomedical imaging. The small

bandgap of monolayer PdSe<sub>2</sub> features resonant optical absorption of such a wavelength. Therefore, PdSe<sub>2</sub> is an ideal material for near-infrared light photodetectors.

A typical PdSe<sub>2</sub> photodetector has been measured under monochromatic illumination [19]. Because the PdSe<sub>2</sub> photodetector is based on field-effect transistors, the gate voltage plays an important role in photodetection. The responsivity of the PdSe<sub>2</sub> photodetector demonstrates a strong gate voltage dependence under 1.06- $\mu\text{m}$  light illumination. The device showed an ultrahigh responsivity of 708 A W<sup>-1</sup> at a gate voltage of 30 V, and the detectivity was calculated to be  $1.31 \times 10^9$  Jones.

The normal positive trend of the photocurrent increases with increasing power intensity [19]. The responsivity of the PdSe<sub>2</sub> photodetector under 4.05- $\mu\text{m}$  illumination is much lower at 1.9 mA W<sup>-1</sup>. The photodetector exhibits excellent stability and repeatability in the environment at room temperature. The absorption spectra of PdSe<sub>2</sub> flakes with different thicknesses demonstrate that the thick PdSe<sub>2</sub> flakes have a higher MIR wavelength absorption. Therefore, this proves the feasibility of photodetection in the mid-infrared band.

However, the photoresponse time of PdSe<sub>2</sub> photodetectors, in the order of several milliseconds, is less than desirable. The photogating effect may account for this phenomenon. That is, photogenerated electrons cannot recombine in a timely manner with photogenerated holes trapped by trap states. Therefore, the lifetime of photoelectrons is prolonged, and the device response is slow.

Both 2D materials and traditional 3D semiconductor materials can form heterostructures with PdSe<sub>2</sub> and perform well in photodetection. A pyramid microstructure for heterojunction photodetectors have demonstrated their excellent performances via the light trapping effect and numerical modeling [62].

The PdSe<sub>2</sub>/pyramid Si photodetector can achieve greater performance than that of the PdSe<sub>2</sub>/Si photodetector in terms of the responsivity, detectivity, and ON/OFF ratio [62], and they are compared with other heterostructures (discussed later in 6.3). The PdSe<sub>2</sub>/pyramid Si photodetector can function as a self-driven device without a power supply. The tuning of the light intensity leads to a difference in the responsivity and ON/OFF ratio at zero bias. The maximum ON/OFF ratio can reach  $1.6 \times 10^5$ . The responsivity and detectivity depend on the illuminating light wavelength, and the maximum values are 456 mA W<sup>-1</sup> and  $9.97 \times 10^{13}$  Jones, respectively. Both are

determined under 980-nm illumination for obtaining the peak sensitivity of the PdSe<sub>2</sub>/pyramid Si photodetector.

Similar to the Si pyramid, Ge nanocones (GeNCs) in heterojunction photodetectors can absorb photons more efficiently [87]. They have a higher photocurrent than that of the PdSe<sub>2</sub>/planar Ge heterostructure. Under 1550-nm illumination with a power intensity of 5  $\mu\text{W cm}^{-2}$ , the PdSe<sub>2</sub>/GeNCs photodetector exhibits a much larger responsivity (530.2 mA W<sup>-1</sup>) and quantum efficiency (42.4%) than those under 1300-nm and 1650-nm illumination. The variation of the current ON/OFF ratios with light intensity was compared under three different wavelengths. This proves the best performance of the PdSe<sub>2</sub>/GeNCs photodetectors in the 1550-nm detection.

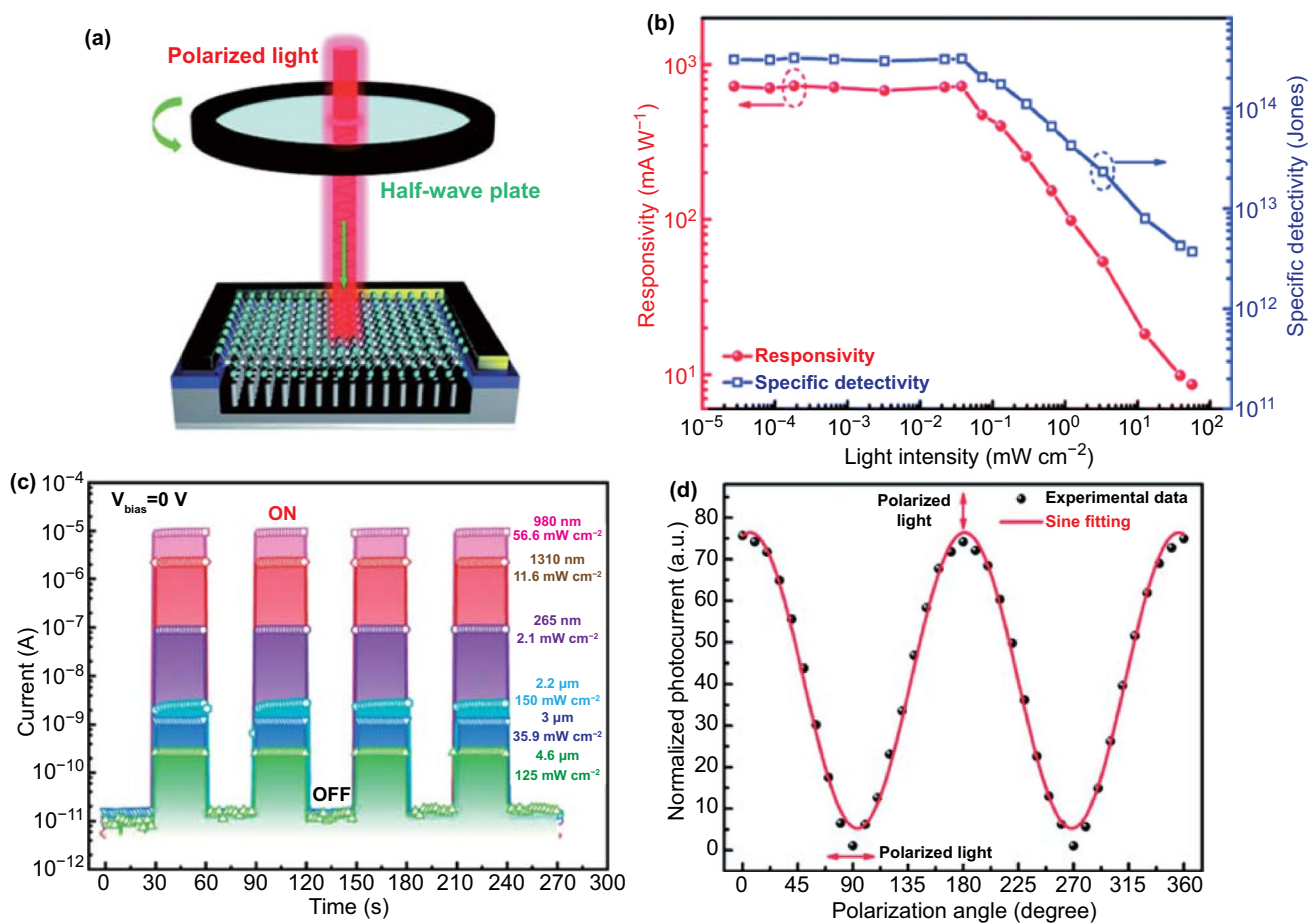
### 5.3 PdSe<sub>2</sub> Photodetectors for Sensing Polarized Light

Polarized light detection can be achieved in the heterostructures of PdSe<sub>2</sub> with other materials, such as PdSe<sub>2</sub>/Si nanowire arrays (SiNWA) [25] and PdSe<sub>2</sub>/perovskite [26] heterostructures.

Figure 19a demonstrates the schematic of the setup of the PdSe<sub>2</sub>/SiNWA heterostructure-based photodetector. The responsivity  $R$  and detectivity  $D^*$  under various light intensities are shown in Fig. 19b. Both parameters increase with the decrease in light intensity and reach a maximum at 726 mA W<sup>-1</sup> and  $3.19 \times 10^{14}$  Jones upon illumination with a light intensity of 27.5  $\text{cm}^{-2}$ . Notably, the PdSe<sub>2</sub>/SiNWA photodetector demonstrates a significant response to the weak light signals with a broad spectral detection range from the deep ultraviolet to the mid-infrared range (Fig. 19c).

However, it shows a high sensitivity to polarized light signals attributed to the asymmetric pentagonal structure of PdSe<sub>2</sub>. Here, the incident polarized light is supplied with various polarization angles through a half-wave plate using a polarizer. The normalized photocurrent was measured versus the polarization angle at zero bias (Fig. 19d). The polarization sensitivity of the PdSe<sub>2</sub>/SiNWA device is 75, which is higher than that of other 2D material-based devices.

Therefore, the PdSe<sub>2</sub>/SiNWA heterostructure exhibits great advantages as the self-driven and wide-band photodetector with highly polarization sensitivity. It has shown a remarkable broad photodetection from DUV to MIR with an excellent



**Fig. 19** PdSe<sub>2</sub> heterostructure-based photodetector for sensing polarized light. **a** Schematic illustration of photodetector based on PdSe<sub>2</sub> and silicon nanowire arrays. **b** Light-intensity-dependent responsivity and detectivity of photodetector. **c** Time-dependent current of photodetector under illumination of infrared light with different wavelengths. Zero bias voltage applies. **d** Evolution of photocurrent under exposure of light with different polarization angles. The fitting curve approximates the sine function. Reprinted with permission from Ref. [25]. Copyright 2020, The Royal Society of Chemistry

responsivity, specific detectivity, response time, and polarization sensitivity. Meanwhile, the device holds prominent potential in infrared imaging of high pixel resolution.

Under 650-nm illumination, the graphene/PdSe<sub>2</sub>/Ge photodetector [21] shows a record polarization sensitivity (112.2) among the reported PdSe<sub>2</sub>-based devices, including PdSe<sub>2</sub>/SiNWA photodetectors (75) and PdSe<sub>2</sub>/perovskite photodetectors (6.04) [26].

A comparison of polarized light sensing is presented for different 2D materials and their heterostructures (Table 7). The polarization sensitivity of the graphene/PdSe<sub>2</sub>/Ge photodetector is much higher than that of some devices based

on other 2D materials, such as GeS<sub>2</sub> (2.1) [88], GeSe<sub>2</sub> (2.16) [89], BP (8.7) [90], antimonene (17) [91], and BP/MoS<sub>2</sub> heterostructures (22) [92].

Analogous to silicene and black phosphorus, PdSe<sub>2</sub> has a high sensitivity to polarized light owing to its anisotropic crystalline structure. Based on this, graphene/PdSe<sub>2</sub>/Ge heterojunction photodetectors have been studied for the polarization-dependent photoresponse [21].

Overall, PdSe<sub>2</sub>-based photodetectors demonstrate remarkable photodetection of broadband bands (from deep ultraviolet to mid-infrared), good responsivity, outstanding stability, and sensitive polarization.



**Table 7** Polarization sensitivity performance of 2D material-based photodetectors

Material types	Illumination wavelength (nm)	Polarization sensitivity	References
Graphene/PdSe <sub>2</sub> /Ge	650	112.2	[21]
PdSe <sub>2</sub> /Si nanowire arrays	n.a	75	[25]
Phosphorene/MoS <sub>2</sub>	3500	22	[92]
Antimonene	450	17	[91]
Phosphorene	1550	8.7	[90]
PdSe <sub>2</sub> /perovskite	808	6.04	[26]
GeSe <sub>2</sub>	n.a	2.16	[89]
GeS <sub>2</sub>	325	2.1	[88]
GeSe	532	1.3	[177]
MoS <sub>2</sub> /GaAs	780	4.8	[178]
ZnSb	1342	1.28	[179]
PdSe <sub>2</sub>	532	1.29	[29]
PdS <sub>2</sub>	n.a	0	[180]
PtSe <sub>2</sub>	10,000	0	[106]
PtS <sub>2</sub>	500	0	[143]

#### 5.4 PdSe<sub>2</sub> Photodetector-enhanced Humidity Sensors

Besides image sensor, PdSe<sub>2</sub>-based devices can be applied to humidity sensors owing to the large surface-to-volume ratio of the PdSe<sub>2</sub> film. For instance, a PdSe<sub>2</sub>/SiNWA device has been utilized as a highly sensitive sensor of the relative humidity (RH) of the ambient environment [25].

Figure 20a shows the response performance of the PdSe<sub>2</sub>/SiNWA devices at various relative humidity values from 11 to 95% in the dark. The response of the device exhibited good stability and repeatability at all RH values.

Moreover, the response of the PdSe<sub>2</sub>/SiNWA device under 780-nm illumination was significantly more sensitive than that in the dark (Fig. 20b). Figure 20c shows that the response speed is further improved under illumination when the RH value is 75%, and the response and recovery times are superior to those of some sensors based on other materials reported previously. The rapid response of the device under illumination may have resulted from the rapid recombination of carriers. Figure 20d plots the incident light intensity dependence of the sensitivity at 75% RH under 780-nm illumination, and the sensitivity of the device increases as the light intensity increases. Furthermore, the PdSe<sub>2</sub>/SiNWA device can retain its initial

sensing performance after 6 months, indicating the good stability of the device [25].

#### 5.5 Saturable Absorber for Pulsed Laser

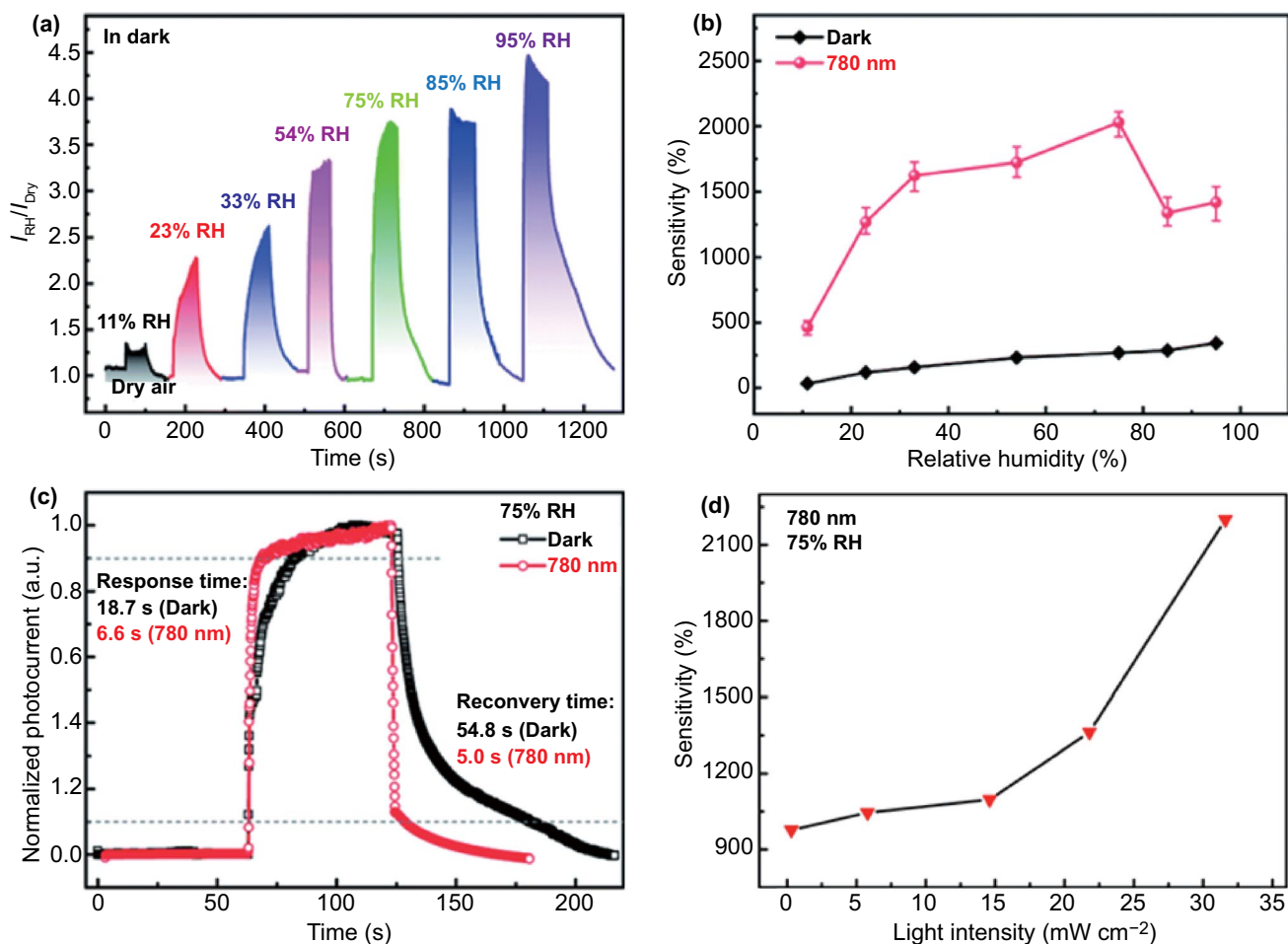
Graphene has been employed as a saturable absorber in the formation of pulsed lasers in the visible to mid-infrared range. However, the zero bandgap of graphene hinders its photonic application. Moreover, TMDCs have been employed as Q switches or mode lockers in the generation of pulsed lasers such as MoS<sub>2</sub>, WS<sub>2</sub>, MoSe<sub>2</sub>, and WSe<sub>2</sub>. However, their bandgaps are tunable in a limited range, i.e., from 1 to 2 eV, which suppresses the potential for application in optical regulation. With a wide range of tunable bandgaps, phosphorene has shown remarkable performance as a saturable absorber in pulsed lasers [93]. However, its weak air stability impedes further studies.

The tunable bandgap and air stability have guaranteed that PdSe<sub>2</sub> is a saturable absorber (SA) in passive Q-switching, which is a crucial method when fabricating pulsed laser devices [94].

A typical PdSe<sub>2</sub>-based passive Q-switched Nd:GdLaNbO<sub>4</sub> laser is demonstrated (Fig. 21a). The laser diode (LD) as a direct pumping source is condensed into the Nd:GdLaNbO<sub>4</sub> crystal through the fiber core and a pair of convex lenses (L1, L2), and it is then transformed into a pulsed laser through the PdSe<sub>2</sub> nanosheet, while the plane mirrors (M1, M2) are coated with the transmission of different reflectivity to control the output laser.

The pulse repetition frequency shows a positive correlation with the absorbed pump power (Fig. 21b), whereas the pulse duration displays a negative correlation. Figure 21c shows the evolution of the pulse energy and peak power of the PdSe<sub>2</sub>/Nd:GdLaNbO<sub>4</sub> laser with varying absorbed pump power, which may be due to the extensive modulation range of PdSe<sub>2</sub>. These results are better than those of MoS<sub>2</sub> and WS<sub>2</sub> [95], proving the excellent characteristics of the PdSe<sub>2</sub> SA and the excellent potential of passive Q-switched lasers.

Due to the suitable bandgaps, 2D materials have been employed as saturable absorbers (SA) for passively Q-switched and mode-locked fiber laser. Besides, optical circuits have incorporated various saturable absorber materials, such as SnTe quantum dots, graphitic-phase C<sub>3</sub>N<sub>4</sub>, MoS<sub>2</sub>, PdS<sub>2</sub>, In<sub>2</sub>Se<sub>3</sub>, PtS<sub>2</sub>, WS<sub>2</sub>, and PdSe<sub>2</sub> [96]. Indeed, they have emerged



**Fig. 20** **a** Variation of current ratio of PdSe<sub>2</sub>-based device with relative humidity in the dark. **b** Relative humidity dependence of sensitivity in the dark and under 780-nm illumination. **c** Temporal response of PdSe<sub>2</sub>-based device at 75% RH in the dark and under 780-nm illumination. **d** Light intensity dependence of sensitivity at 75% RH under 780 nm. The RH denotes the relative humidity. Reprinted with permission from Ref. [25]. Copyright 2020, Royal Society of Chemistry

as cost-effective, simple, and highly integrated component for pulsed laser generation.

Future works may lie in the adoption of PdSe<sub>2</sub>-based van der Waals heterostructures as saturable absorbers for pulsed laser modulation in the fiber lasers or solid-state lasers.

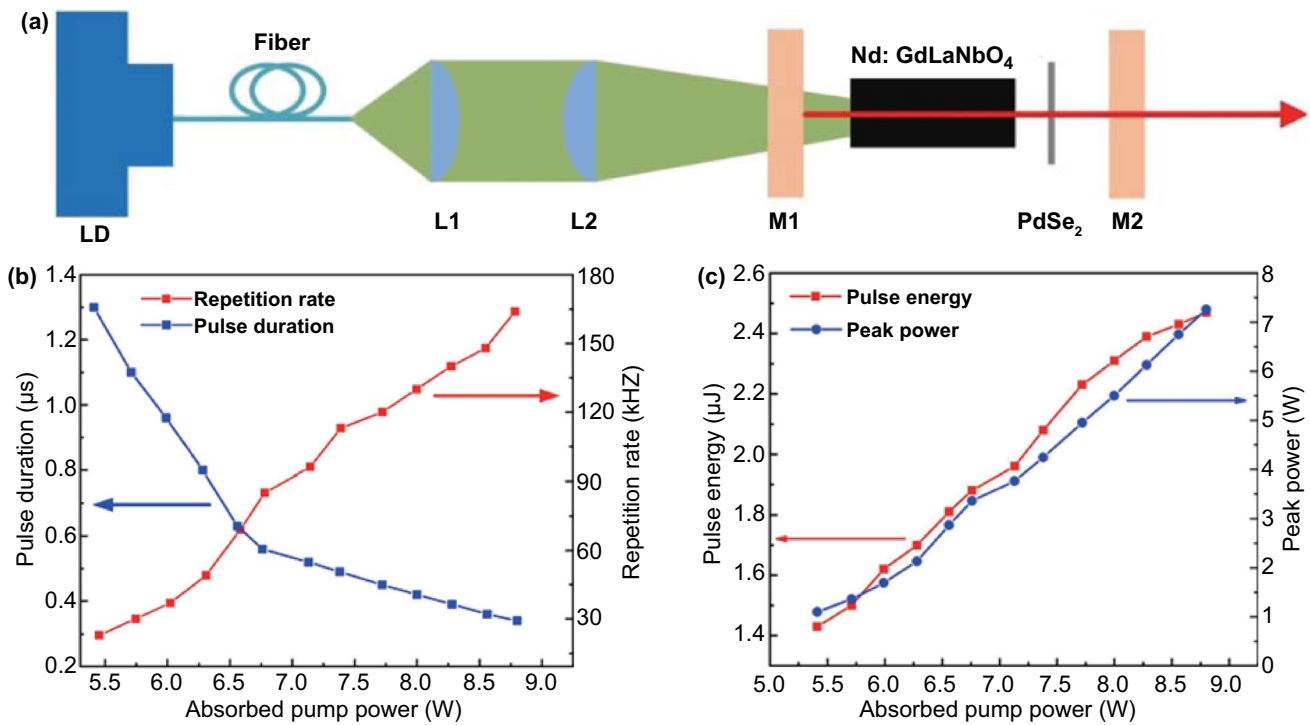
Previously, the electronics, optoelectronics, and optics of PdSe<sub>2</sub> have been introduced. Besides, the PdSe<sub>2</sub> may possess great promises in the environmental, energy and biomedical applications. Indeed, the 2D materials have demonstrated the great performances in clean energy production [97–99], i.e., catalysis of hydrogen production or oxygen reduction, solar cells [100], thermoelectric power generation, energy storage, environmental remediation [101, 102], and photodegradation of organic-molecules-polluted water [103] as well as water

purification. Besides, the metallic low dimension materials may favor the anti-bacterial performances as well as other biomedical engineering.

After knowing the devices of individual PdSe<sub>2</sub> material, we come to the discussion of PdSe<sub>2</sub>-based van der Waals heterostructures.

## 6 PdSe<sub>2</sub>-based van der Waals Heterostructures

The vdWHs of 2D materials employ weak layer interactions between two stacked layered materials to form multilayer structures. Owing to the enriched choice



**Fig. 21** a Schematic illustration of PdSe<sub>2</sub> passively Q-switched Nd:GdLaNbO<sub>4</sub> pulsed laser experimental setup. b Pulse duration (left) and repetition rate (right) versus absorbed pump power. c Variation of the pulse energy (left) and pulse peak power (right) with the absorbed pump power. Reprinted with permission from Ref. [94]. Copyright 2020, Elsevier Ltd

of conductivity types, 2D materials can be stacked by choosing from semiconducting, metallic, and insulating types. Indeed, 2D material-based vdWHs have enhanced the device architectures of conventional Si technology. Here, PdSe<sub>2</sub> as a semiconducting 2D material could broaden the applicability of 2D vdWHs. In this section, we discuss emerging applications in electronics, such as rectifiers and optoelectronics, such as image sensors.

### 6.1 Van der Waals Heterostructure Based on PdSe<sub>2</sub>/MoS<sub>2</sub> Contact

Two-dimensional heterojunction-based photodetectors show superior photoresponse time and detectivity. PdSe<sub>2</sub>/MoS<sub>2</sub> vdWH photodetectors (Fig. 22a) can effectively improve the responsivity and detectivity under 10.6- $\mu\text{m}$  illumination, and the rise/fall time ( $\tau_r/\tau_f$ ) of the photocurrent is 65.3/62.4  $\mu\text{s}$  [54].

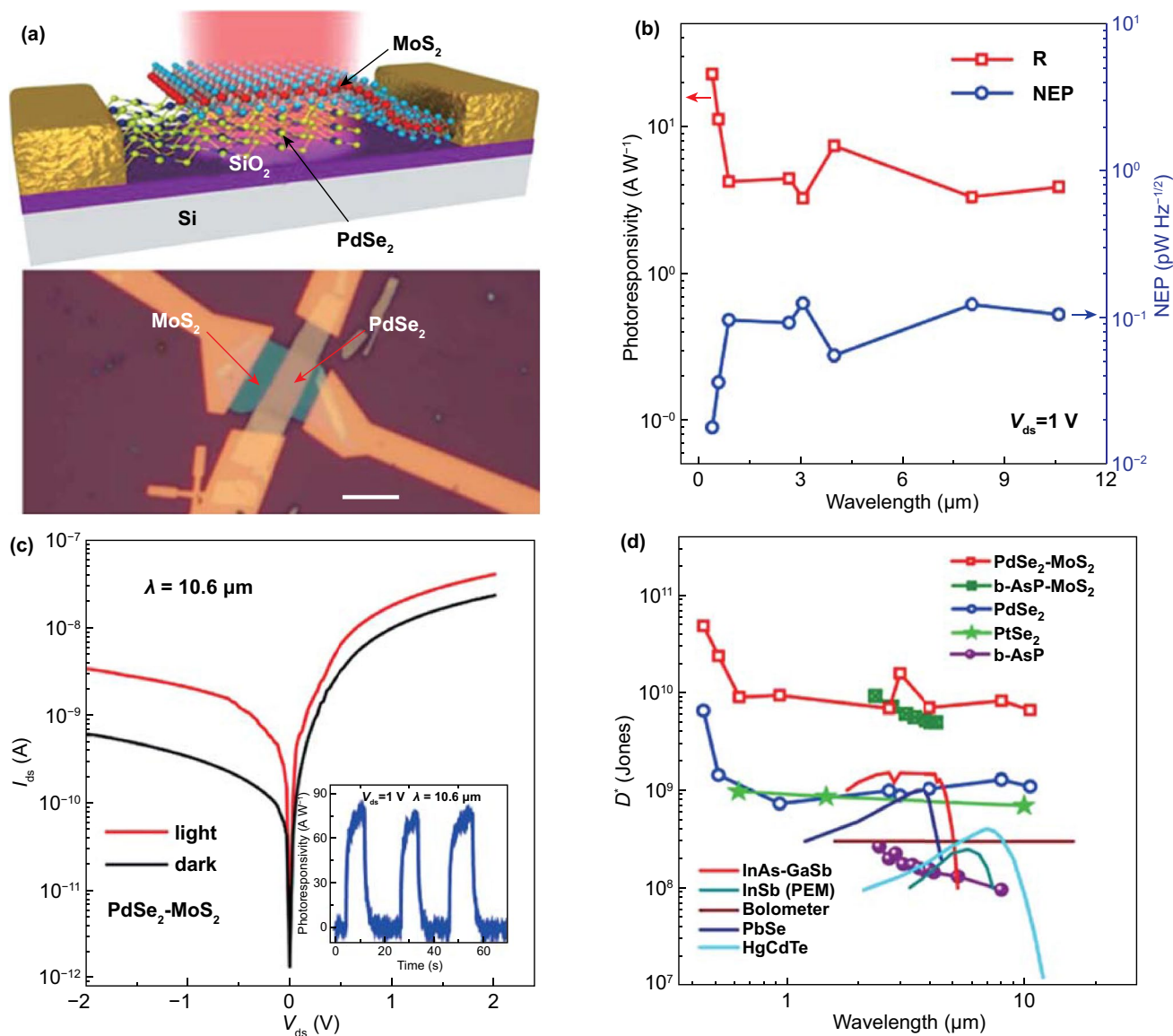
The vdWH can significantly suppress the dark current and current noise of the device, and the photocurrent can be

generated under the combined action of intralayer excitons and interlayer excitons [54].

Figure 22b shows the responsivity and noise equivalent power as a function of the incident wavelength. PdSe<sub>2</sub>-based heterojunction photodetectors have better responsivity and detectivity for broadband detection. Typical photocurrent performances are presented in the dark and under illumination (Fig. 22c).

The photoresponse time can be improved by fast charge transfer in the heterostructure. Indeed, the PdSe<sub>2</sub>/perovskite heterojunction photodetector could solve the problems faced by most perovskite photodetectors, i.e., low specific detectivity and slow photoresponse [104].

The detectivity of PdSe<sub>2</sub>/MoS<sub>2</sub> photodetectors can reach  $8.21 \times 10^9$  Jones, which is much better than that of most mid-infrared photodetectors (Fig. 22d) based on AsP [105], PtSe<sub>2</sub> [106], graphene thermopiles [107], and uncooled HgCdTe [108]. The detectivity of PdSe<sub>2</sub> exceeded that of some traditional mid-infrared photodetectors [108]. Compared with the PdSe<sub>2</sub>/MoS<sub>2</sub>



**Fig. 22** PdSe<sub>2</sub>/MoS<sub>2</sub> van der Waals heterostructure-based photodetector. **a** Scheme of the PdSe<sub>2</sub>/MoS<sub>2</sub> photodetector (top) and optical micrograph of the corresponding device (bottom), where the scale bar is 5 μm. **b** Wavelength dependence of photoresponsivity (red) and noise equivalent power (blue) of the PdSe<sub>2</sub>/MoS<sub>2</sub> photodetector at V<sub>DS</sub> = 1 V. NEP denotes noise equivalent power. **c** Drain current of heterostructure-based device under illumination and in the dark. The inset shows the current profile against time with periodic light illumination and dark state. **d** Wavelength-dependent detectivity of different 2D materials and some infrared materials at room temperature. Reprinted with permission from Ref. [54]. Copyright 2019, American Chemistry Society

photodetector (Table 8), the potential of PdSe<sub>2</sub> in mid-infrared photodetection is further reflected.

## 6.2 PdSe<sub>2</sub> van der Waals Heterostructure-based *p-n* Junction-based Rectifier

The optoelectronics has stemmed from the fundamental component of *p-n* junctions. Indeed, the conventional 3D

thin film stacking has contributed to the photovoltaics [109, 110], photodetectors, tunneling transistors, rectifiers, and light-emitting diodes. The metal/semiconductor contact has favored the Ohmic type conductance behavior for elevating the charge carrier transport. These investigations based on thin film deposition techniques have provided useful guide for 2D materials.

**Table 8** Detectivity performance of 2D materials in mid-infrared photodetectors

Materials	Illumination wavelength (nm)	Detectivity (Jones)	References
PdSe <sub>2</sub> /MoS <sub>2</sub>	10,600	$8.21 \times 10^9$	[54]
AsP	5000	$4.9 \times 10^9$	[105]
PtSe <sub>2</sub>	10,000	$7 \times 10^8$	[106]
graphene thermo-piles	n.a	$8 \times 10^8$	[107]
uncooled HgCdTe	9000	$10^9$	[108]

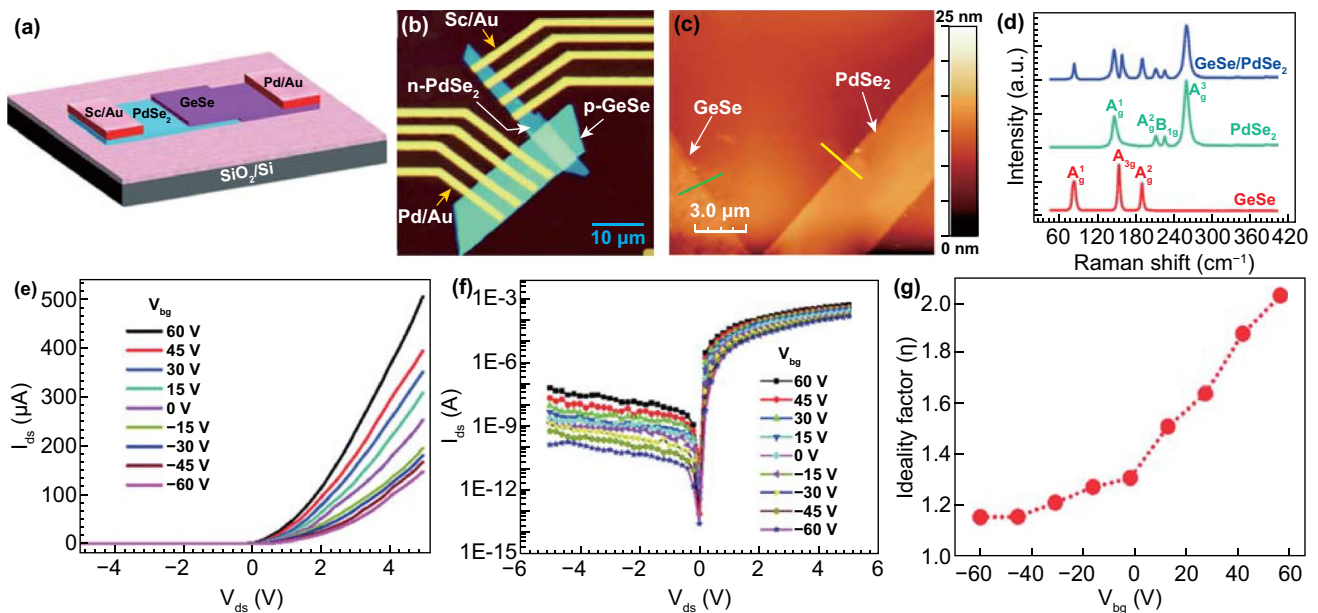
Two types of 2D materials stack together with weak interaction, termed van der Waals heterostructure. With delicate selection, one can assembly a *p-n* junction with the atomic layer thickness [111, 112]. No dangling bonds remain at their interface; besides, low lattice mismatch between both 2D materials result in the declined defect states. Therefore, the quantity of scattering center for charge carrier is minimized for boosting the charge carrier transport, which is superior to the Si based materials.

High gate-modulated rectification in vdWHs based on PdSe<sub>2</sub> has been introduced and examined. For example, *p*-type germanium selenide (GeSe) and *n*-type PdSe<sub>2</sub> with a pure ohmic contact show a large rectification ratio, which is defined as the ratio between the forward and reverse currents, up to  $5.5 \times 10^5$ , resulting from the clean interface and low Schottky barrier [24].

One can find schematic of the *p*-GeSe/*n*-PdSe<sub>2</sub> vdWH-based rectifier device (Fig. 23a), and the corresponding optical image (Fig. 23b).

Figure 23c displays the AFM images of the GeSe and PdSe<sub>2</sub> flakes with thicknesses of 12 and 11.5 nm, respectively. The Raman spectra of GeSe and PdSe<sub>2</sub> demonstrate the successful stacking of both 2D materials (Fig. 23d).

For *p*-GeSe/*n*-PdSe<sub>2</sub> diodes, the linear scale (Fig. 23e) and the semi-log scale (Fig. 23f) of the drain current versus voltage curves were measured at different gate voltages. Indeed, the gate voltage can modulate the rectifying effect. This result is due to the carrier density and electrostatic inversion from semiconductor to semi-insulator materials [113]. Figure 23g presents the variation in the ideality factor  $\eta$  of the *p-n* diodes, which is obtained as 1.2 at a negative gate voltage. The *p-n* diode tends to decrease its ideality at



**Fig. 23** GeSe/PdSe<sub>2</sub> junction-based rectifier. **a** Schematic of the GeSe/PdSe<sub>2</sub> *p-n* junction. **b** Optical micrograph of the GeSe/PdSe<sub>2</sub> junction with Pd/Au and Sc/Au electrodes. **c** AFM image of the GeSe/PdSe<sub>2</sub> heterostructure. **d** Raman spectra of the GeSe/PdSe<sub>2</sub> junction and individual flakes. **e**, **f** Drain current versus voltage curves of the device in a linear scale and semi-log scale with sweeping different back gate voltages. **g** Gate voltage dependence of the ideality factor of the device. Reprinted with permission from Ref. [24]. Copyright 2020, The Royal Society of Chemistry

a positive gate voltage, which can be attributed to the carrier recombination at the sharp interface resulting from the decrease in electric field [114]. Table 9 compares the rectification ratios of typical  $p$ - $n$  diodes based on the vdWHs of PdSe<sub>2</sub> and other 2D materials.

This proves that nTMDC-based rectifier may hold promises in logic switches as shown in other TMDC logic circuits [115]. Besides, the nTMDC-based rectifier could be employed as an energy harvester for collecting the electromagnetic wave energy as proved by other 2D materials [116].

### 6.3 PdSe<sub>2</sub> van der Waals Heterostructure-based Junction Photodetectors

The PdSe<sub>2</sub> based van der Waals heterostructures remain less investigated in terms of fabrication strategies. One can refer to the investigation of other vdWH emerging 2D materials. To date, the dry stamp transfer method has dominated the stacking nanosheets. Indeed, the epitaxy-based synthesis has great opportunities of fabricating the secondary layer of 2D materials. Besides, large quantity of 2D materials remain unexplored for the stacking of 2D materials such as metal–organic framework, graphene, MoS<sub>2</sub>, ReSe<sub>2</sub>, PtSe<sub>2</sub>, MXene, and tellurium as well as perovskites. Besides, the lateral heterostructure may arise the attention for novel charge carrier transport.

To investigate the additional features of the  $p$ - $n$  vdWH diode, the photoresponse was investigated [117]. Figure 24a shows a schematic of the  $p$ -BP/ $n$ -PdSe<sub>2</sub> vdWH diode under illumination.

The time-resolved photocurrent was measured under intermittent lasers with different wavelengths at a fixed

**Table 9** Rectification ratio of  $p$ - $n$  junction-based diodes with different van der Waals heterostructures based on 2D materials

$p$ - $n$ junction diodes	Rectification ratio	References
GeSe/PdSe <sub>2</sub>	$5.5 \times 10^5$	[24]
Phosphorene/PdSe <sub>2</sub>	$7.1 \times 10^5$	[117]
Phosphorene/MoS <sub>2</sub>	$1 \times 10^5$	[181]
GaSe/InSe	$1 \times 10^5$	[182]
Graphene/WSe <sub>2</sub>	$1 \times 10^4$	[115]
WSe <sub>2</sub> /MoS <sub>2</sub>	$1 \times 10^4$	[183]
WSe <sub>2</sub> /SnSe <sub>2</sub>	$2.1 \times 10^4$	[184]
MoS <sub>2</sub> /WSe <sub>2</sub>	$1.3 \times 10^5$	[185]
WSe <sub>2</sub> /GeSe	$1 \times 10^5$	[186]

power (Fig. 24b). The varying incident wavelengths from the visible to NIR region on the  $p$ -BP/ $n$ -PdSe<sub>2</sub> diode led to current versus voltage curves (Fig. 24c). This indicates that the photocurrent decreased when the incident wavelength increased. The photocurrent of the diode depends on the back-gate voltage (Fig. 24d).

The energy band alignment of  $p$ -BP,  $n$ -PdSe<sub>2</sub>, and their heterostructures after contact (Fig. 24e), with the CBM, VBM, work function, and electron affinity. A magnified view of the band alignment is presented after contact at a gate voltage of 0 V (Fig. 24e). When the diode operates at a negative back-gate voltage, the Fermi level moves away from the conductance band. This increases the potential barrier of the  $p$ -BP/ $n$ -PdSe<sub>2</sub> interface, resulting in a high rectifying current. The Fermi level approaches the conductance band at a negative gate voltage (Fig. 24f) and decreases the potential barrier and rectification ratio. For the  $p$ -BP/ $n$ -PdSe<sub>2</sub> diode, the positive gate voltage (Fig. 24g) can modulate the Fermi level and control the carrier densities, which can eventually control the rectification ratio.

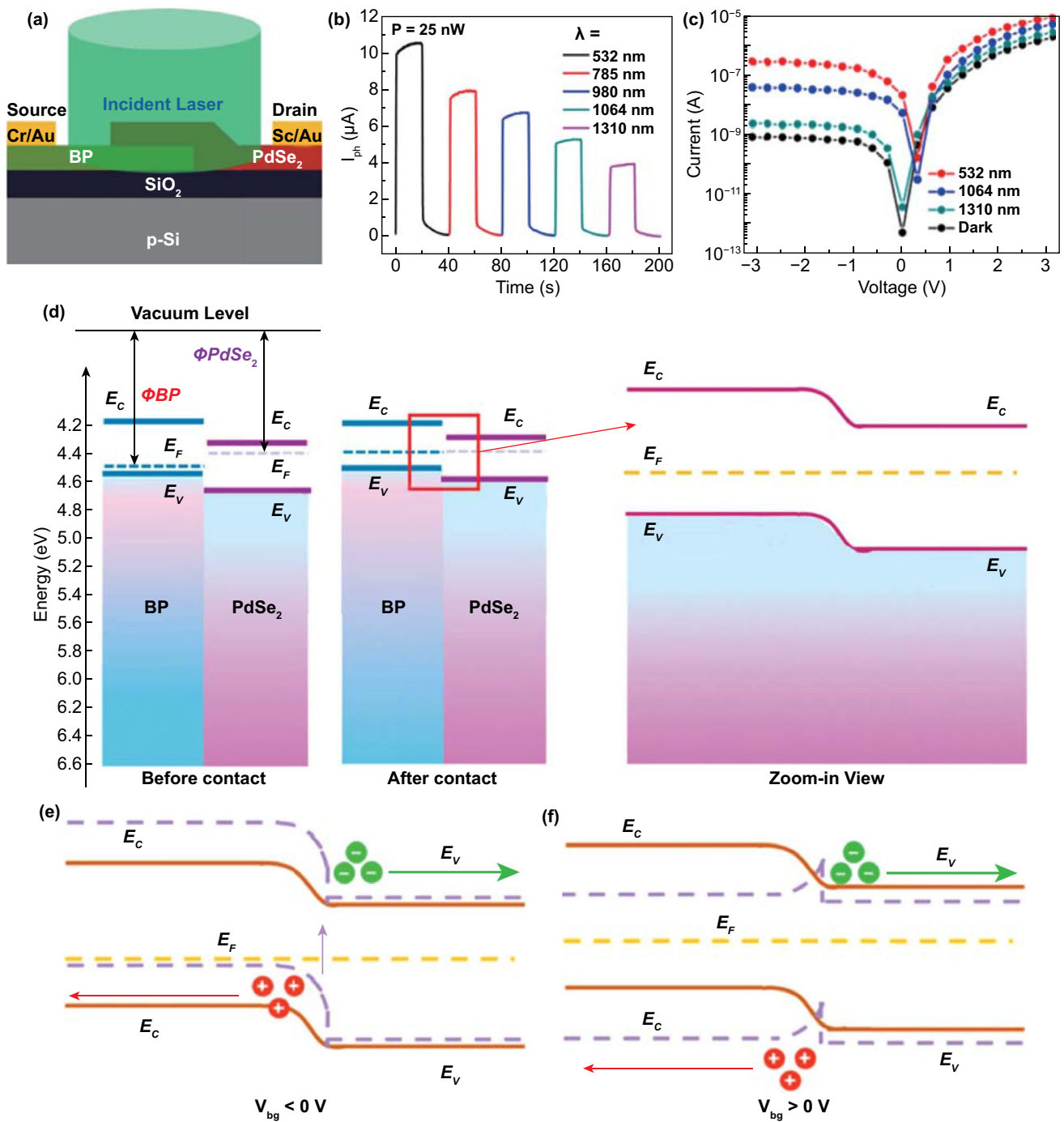
Therefore, the PdSe<sub>2</sub>  $p$ - $n$  junction-based photodiode shows a great potential in high-performance visible-infrared photodetectors, as well as solar cell for electricity production. This  $p$ - $n$  diode concept may broaden the application of 2D nTMDC-based heterostructures in photovoltaics.

In this section, we discuss the structure and performance of different photodetectors based on PdSe<sub>2</sub>. A comparison of the performances of different PdSe<sub>2</sub>-based photodetectors is listed in Table 10.

### 6.4 Image Sensor System from PdSe<sub>2</sub> van der Waals Heterostructure

Because of the excellent performance of PdSe<sub>2</sub> in the field of photodetection, some studies subsequently explored further possibilities in the image sensor field. Infrared image sensors have emerged as an essential device unit in optoelectronic systems such as fire monitoring, night vision, and surveillance cameras [118].

The PdSe<sub>2</sub>/pyramid Si device presented superior results in terms of infrared image sensing [119]. In portable systems, cardboard masks can be imaged using such a device. The geometry of the house and tree shapes was imaged under 980-nm and 1300-nm illumination. The illuminated areas are highlighted in photocurrent mapping. In contrast, the



**Fig. 24** **a** Schematic of the *p*-BP/*n*-PdSe<sub>2</sub> *p*-*n* diode under illumination. **b** Time-dependent  $I_{ph}$  of the *p*-BP/*n*-PdSe<sub>2</sub> photodiodes under the illumination of different wavelengths. **c**  $I_{DS} - V_{DS}$  curves under the illumination of different wavelengths at back gate voltage of 10 V. **d** Energy band of the *p*-BP/*n*-PdSe<sub>2</sub> van der Waals heterojunction before contact and after contact with a zoom-in view. Energy band alignment of a *p*-BP/*n*-PdSe<sub>2</sub> photodiode under **e** a negative back-gate voltage and **f** a positive back-gate voltage. Reprinted with permission from Ref. [117]. Copyright 2020, American Chemical Society

**Table 10** Performances of photodetectors based on 2D PdSe<sub>2</sub> and its van der Waals heterostructures as well as related nanostructures

Materials	Wavelength or band $\lambda$ (nm)	Responsivity $R$ (mA W <sup>-1</sup> )	Detectivity $D^*$ (Jones)	$I_{\text{light}}/I_{\text{dark}}$	$\tau_r/\tau_f$	References
PdSe <sub>2</sub> /MoS <sub>2</sub>	10,600	$4.21 \times 10^4$	$8.2 \times 10^9$	10	65.3/62.4 $\mu$ s	[54]
PdSe <sub>2</sub> /GeNCs	1550	530.2	$1.45 \times 10^{11}$	$7 \times 10^3$	25.4/38.5 $\mu$ s	[87]
PdSe <sub>2</sub>	1060	$7.08 \times 10^5$	$1.31 \times 10^9$	10	220 ms	[19]
PdSe <sub>2</sub>	1060	n.a	n.a	n.a	156/163 $\mu$ s	[41]
PdSe <sub>2</sub> /Ge	980	691.5	$1.73 \times 10^{13}$	$10^5$	6.4/92.5 $\mu$ s	[21]
PdSe <sub>2</sub> /pyramid Si	980	456	$9.97 \times 10^{13}$	$1.6 \times 10^5$	n.a	[119]
PdSe <sub>2</sub> /SiNWA	980	726	$3.19 \times 10^{14}$	$10^6$	3.4/3.9 $\mu$ s	[25]
PdSe <sub>2</sub> /perovskite	808	313	$2.72 \times 10^{13}$	$10^4$	3.5/4 $\mu$ s	[26]
PdSe <sub>2</sub> /Si	780	300.2	$1.18 \times 10^{13}$	$1.08 \times 10^5$	38/44 $\mu$ s	[62]
PtSe <sub>2</sub> /SiNWA	200–1550	$1.265 \times 10^4$	$2.5 \times 10^{13}$	$4 \times 10^4$	10.1/19.5 $\mu$ s	[7]
PtSe <sub>2</sub> /n-GaN	265	193	$3.8 \times 10^{14}$	$10^8$	45/102 $\mu$ s	[82]
PtS <sub>2</sub>	500	$1.56 \times 10^6$	$2.9 \times 10^{11}$	n.a	0.46 s	[143]
WS <sub>2</sub> /p-Si	340–1100	$5.7 \times 10^3$	n.a	10.65	670/998 $\mu$ s	[187]
WS <sub>2</sub>	365	$5.35 \times 10^4$	$1.22 \times 10^{11}$	n.a	n.a	[161]
NiPS <sub>3</sub>	254	126	$1.22 \times 10^{12}$	200	3.2/15.6 ms	[188]
BP	640–940	4.8	n.a	n.a	1/4 ms	[83]
MoS <sub>2</sub> /BP	532–1550	153	n.a	n.a	15/70 $\mu$ s	[189]
MoS <sub>2</sub> /n-Si	300–1100	$1.19 \times 10^4$	$2.1 \times 10^{10}$	59.9	30.5/71.6 $\mu$ s	[190]
MoS <sub>2</sub> /Graphene	420–980	835	n.a	n.a	20/30 ms	[191]
MoS <sub>2</sub> /p-GaN	265	187	$2.34 \times 10^{13}$	$10^5$	46.4/114.1 $\mu$ s	[85]
GaN	325	340	$1.24 \times 10^9$	n.a	280/450 ms	[192]
GaSe/GaSb	400–1800	115	$1.3 \times 10^{12}$	n.a	32/24 $\mu$ s	[193]
InGaAs/p-Si	400–1250	$7.52 \times 10^3$	n.a	n.a	13/16 ms	[194]
MgO	150	$1.86 \times 10^3$	$1.8 \times 10^{10}$	$10^2$	n.a	[195]
Graphene/Ge	1200–1600	51.8	$1.38 \times 10^{10}$	$2 \times 10^4$	23/108 $\mu$ s	[196]
Graphene/n-Si	300–1100	730	$4.2 \times 10^{12}$	$10^4$	320/750 $\mu$ s	[197]
Graphene/MoTe <sub>2</sub> /Graphene	1064	110	$10^{10}$	n.a	24/46 $\mu$ s	[198]
Graphene/Si	365	120	$6.1 \times 10^{12}$	$10^5$	4/12 ns	[84]

photocurrent in the other areas remained much weaker, similar to the dark state.

Although some blemishes in the blocked regions need to be further corrected, the shapes of the patterns can be distinguished easily by contrast. Similar results were obtained for the PdSe<sub>2</sub>/GeNCs hybrid device [263], indicating the reliable infrared imaging capability of PdSe<sub>2</sub>-based devices.

The suitable bandgap of PdSe<sub>2</sub> guarantees its application in infrared light sensing. When the devices are fabricated into arrays, the system can achieve image sensing with high pixel numbers [21]. When the polarized light is incident on the device through a specific mask, the lock-in amplifier can timely scan the voltage of the device and transform it into the voltage mapping image.

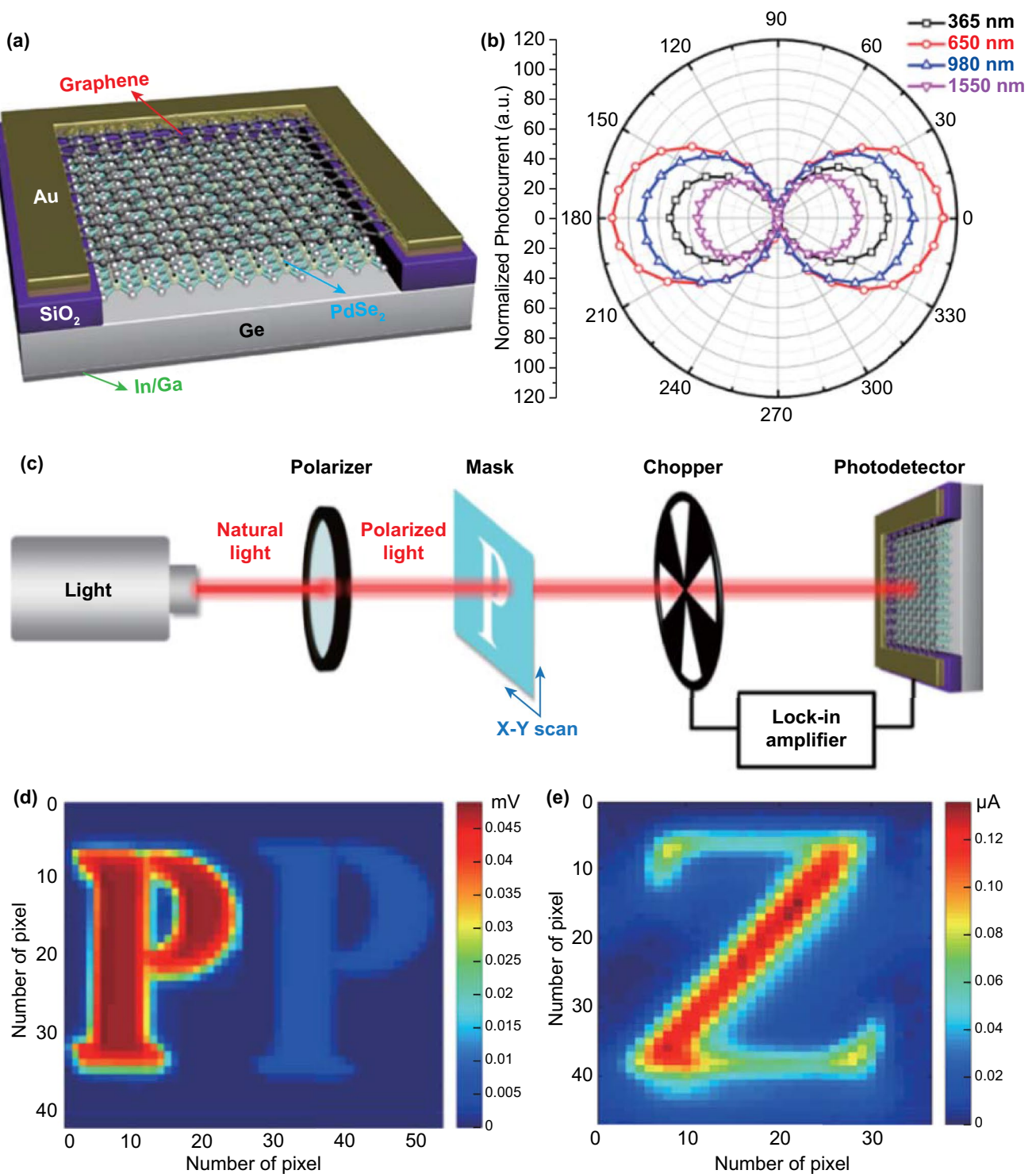
The graphene/PdSe<sub>2</sub>/Ge photodetector with a broadband range from ultraviolet to near-infrared light (Fig. 25a).

The normalized photocurrent of the graphene/PdSe<sub>2</sub>/Ge device shows a strong correlation with the polarization angle under various illuminations having different wavelengths, including 365, 650, 980, and 1550 nm (Fig. 25b).

The maximum and minimum values of the photocurrent were achieved at polarization angles of 0° (180°) and 90° (270°), respectively. Indeed, the sine-shaped photocurrent curve indicates a good polarization sensitivity of the graphene/PdSe<sub>2</sub>/Ge device [21].

A high-resolution infrared image is compiled after projecting a patterned light to the detector (Fig. 25c) after passing through the P letter mask (Fig. 25d). Here, the photocurrent intensity is stronger with a polarization





**Fig. 25** Graphene/PdSe<sub>2</sub>/Ge heterostructure-based polarized-light image sensor. **a** View of the image sensing device. **b** Photocurrent of the sensor under the illumination of monochromatic light by regulating different polarization angles. The light sources of four wavelengths are employed for light irradiation. **c** System setup for imaging the mask of a capital *P* with the illumination of infrared polarized light. **d** High-resolution current mapping image of the capital *P* under 780-nm light illumination with polarization angles of 0° (left) and 90° (right). **e** Imaging of a capital *Z* with a polarization angle of 0°. Reprinted with permission from Ref. [21] Copyright 2019, American Chemistry Society

angle of  $0^\circ$  (left panel) than that of polarized light at  $90^\circ$  (right panel). The high polarization contrast ratio ( $> 10$ ) between the polarization angles of  $0^\circ$  and  $90^\circ$  indicates the outstanding performance of the PdSe<sub>2</sub>-based device in polarized light imaging. The heterojunction-based photodetector has excellent potential as a mid-infrared image sensor. Figure 25e presents a highly recognizable spectral image of the Z letter under 3043-nm illumination with a polarization angle of  $0^\circ$ .

Such an image sensor is highly promising for broadband photodetection and imaging. The PdSe<sub>2</sub> heterojunction-based photodetector demonstrates an extraordinary polarization sensitivity, which is the highest value among 2D material-based polarized light photodetectors (thus far). On account of a strong asymmetry of PdSe<sub>2</sub>, the effective separation of photogenerated electron–hole pairs occurs by a built-in perpendicular electric field in the *p–n* junction. Then, the efficiency of the carrier collection is enhanced by graphene electrode. Therefore, PdSe<sub>2</sub> is a very profound material for high-performance polarization-sensitive photodetectors.

The integration with light-absorbing materials could provide the power source owing to the photovoltaic effect. Moreover, the use of perovskite as an absorber material can transform the light into electricity for self-powering by forming a Schottky junction with PdSe<sub>2</sub>. The PdSe<sub>2</sub>/perovskite heterostructure photodetector is illustrated in Fig. 26a with a high quantum efficiency (Fig. 26b).

Such a photodetector has a broad detection band ranging from 200 to 1200 nm. Through tuning of the illuminating light with various incident wavelengths from 265 to 980 nm, the current of the photodetector has been recorded. Here, the photocurrent curve displays a maximum value under 808-nm illumination at a negative bias (Fig. 26c), which corresponds to the quantum efficiency peak around 800 nm.

In the inset panel, the current–voltage curves show the photovoltaic effect upon illumination. Similarly, PdSe<sub>2</sub>/perovskite photodetector-based arrays can be employed in image sensing with significant photoresponse capability (Fig. 26d). When the infrared light passes through the mask, the projection of the features from the mask is captured by the detector. Moreover, the processing unit converted the current signal to each pixel. Subsequently, the 2D contrast current mapping software automatically incorporates the data and exhibits the current mapping image.

Consequently, the outlines of the five letters can be recognized by 2D current mapping under 808-nm illumination. Therefore, the PdSe<sub>2</sub>/perovskite heterostructure device shows potential for the future image sensing of complicated shapes such as human beings and animals.

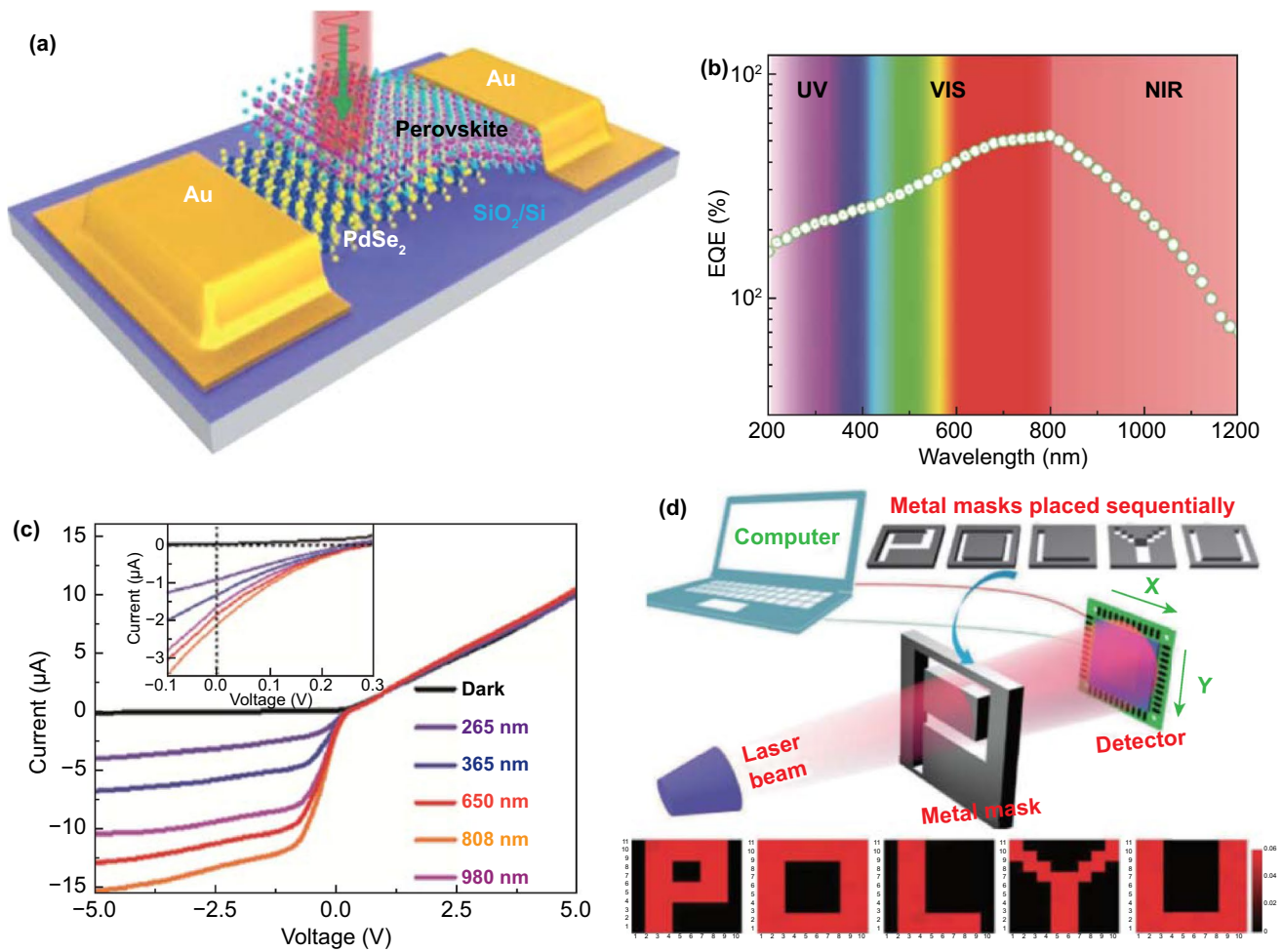
The currently available image sensors are listed in Table 11. The resolution and current contrast ratio may require the future efforts for improvement.

Owing to the superior capability of detecting mid-infrared light at room temperature, PdSe<sub>2</sub>-based devices highlight the high potential for application of photodetectors and image sensor systems. There remain good opportunities in the formation and application of vdWHs based on PdSe<sub>2</sub> and other 2D materials. Indeed, low-dimensional materials have yet to be tested in vdWH assemblies with the coupling of PdSe<sub>2</sub>.

## 7 Conclusions and Outlook

In this work, we deliver a comprehensive review of the progress in the rising-star pentagonal 2D material, i.e., palladium diselenide. First, the fundamental of PdSe<sub>2</sub> is introduced with the types, atomic and electronic structure, bandgap, and vibration properties. Second, the synthesis approaches are listed with top-down and bottom-up methods. Indeed, the authors are fed with mechanical exfoliation, plasma thinning, and vacuum annealing. Then, the large-area synthesis has been introduced with thermal selenization of Pd thin film, and chemical vapor deposition with different Pd precursors such as PdCl<sub>2</sub> powers. Third, the electronic and optoelectronic devices are discussed with the metal/semiconductor contact, field-effect transistors, photodetectors, and humidity sensors. The PdSe<sub>2</sub> has been employed in the generation of pulsed laser and the thermoelectric power. Last but not the least, the van der Waals heterostructures of PdSe<sub>2</sub> are delivered as well as their applications in the rectifier, photodetectors, and image system.

The fundamental physics of PdSe<sub>2</sub> may provide for the insight for the guide of device design and fabrication. Indeed, the engineering applications of conventional devices and characterization tools require refreshing novel materials to enrich the interdisciplinary research across the microelectronics, optoelectronics, spectroscopy, optics, photonics, spintronics, and valleytronics. Besides, the magnetic properties of materials are interesting for the incubation



**Fig. 26** PdSe<sub>2</sub>/perovskite heterostructure-based photodetector arrays for imaging. **a** Schematic of the PdSe<sub>2</sub>/perovskite-based photodetector. **b** External quantum efficiency of the PdSe<sub>2</sub>/perovskite device as a function of the incident wavelength. **c** Current–voltage curve of the PdSe<sub>2</sub>/perovskite photodetector in the dark and under illumination with different wavelengths. Inset is zoomed-in current–voltage curves at the range from –0.1 to 0.3 V. **d** Scheme of the imaging system based on the photodetector arrays under 808-nm illumination, and 2D photocurrent mapping images after sensing five different letters. Adapted under the terms of the Creative Commons CC by license (<https://creativecommons.org/licenses/by/4.0/>) from Ref. [26] Copyright 2019, The Authors, published by WILEY–VCH Verlag GmbH & Co. KGaA, Weinheim

**Table 11** Performances of image sensors based on 2D PdSe<sub>2</sub> and its van der Waals heterostructures

Material types	Resolution (pixel)	Mask area (cm <sup>2</sup> )	Active device area (cm <sup>2</sup> )	Current contrast ratio	Wavelength λ (nm)	References
PdSe <sub>2</sub> /Ge	46 × 46	5 × 5	0.6 × 0.6	> 10 <sup>2</sup>	3043	[21]
PdSe <sub>2</sub> /pyramid Si	19 × 20	several	0.1 × 0.1	> 10 <sup>2</sup>	1330	[119]
PdSe <sub>2</sub> /GeNCs	6 × 6	several	Sub-1	10 <sup>2</sup>	1550	[87]

of the proof-of-concept devices. Besides, the band alignment in a heterostructure may provide a platform for photo-generated carrier transport. The 2D materials as saturable absorbers have demonstrated extraordinary performances

in Q-switching and mode lock for pulsed laser generation. Indeed, the metallic 2D materials have demonstrated superior performances in electromagnetic interference shielding or microwave absorption. Besides, the incorporation of

magnetic nanoparticles may lead to the change of magnetoresistance as a magnetic field sensor.

The performance of PdSe<sub>2</sub> devices has been verified in photodetectors [62], field-effect transistors [16], and humidity sensors [25]. First, PdSe<sub>2</sub> transistors demonstrate pressure-tunable hysteresis [70], field emission [81], and phototransistors [41]. Second, the narrow bandgap of PdSe<sub>2</sub> guarantees its performance in an infrared range such as 10.6- $\mu$ m light detection [54] and broadband sensing [19]. Third, the linear dichroism transition [39] in PdSe<sub>2</sub> guarantees optical switching and communication. As a saturable absorber, PdSe<sub>2</sub> shows success in Q-switching for pulsed lasers [96].

There are still plenty of room in the development of sophisticated techniques for mass production of PdSe<sub>2</sub>. First, the chemical vapor deposition [120] has the features of upscale production, large-area homogeneity, and compatibility with Si-based technology. Indeed, the chemical vapor deposition of 2D materials [121–123] become necessary to achieve the synthesis over a large area and even a wafer size [124]. Owing to the layer-dependent properties, the preparation methods of high-quality 2D PdSe<sub>2</sub> should be modified to accurately control the thickness, which is essential for the manufacture of high-performance devices. According to the trend of sophisticated 2D materials such as graphene, the quality of synthetic PdSe<sub>2</sub> may go through the path, i.e., from mechanically exfoliated nanosheets, ball-milled nanopowders [125], polycrystalline thick films, monolayer or bilayer polycrystalline thin film [126, 127], and monolayer single-crystal domains [128]. More effective synthesis of atomically thin, large-scale, and uniform 2D PdSe<sub>2</sub> should be explored to satisfy the needs of industrialization. Eventually, the domain size of PdSe<sub>2</sub> single crystal may expand to centimeter scale and even to the wafer scale.

The posttreatment of PdSe<sub>2</sub> may broaden its material properties, and consequently, its device performances may vary. First, the thermal annealing or plasma treatment [129] has shown modification of 2D materials. Second, the in situ characterization tools such as transmission electron microscopy [130] and XRD may provide the direct evidence for phase transition, i.e., the lattice distortion in the atomic scale. Third, the machine learning acts an efficient tool for defects determination and device performances enhancement. The properties of 2D materials could be regulated with defect engineering by the theoretical calculation, as well as big data for materials science. Besides, the patterning

of 2D materials becomes a prerequisite for the fabrication of device arrays.

Future opportunities of PdSe<sub>2</sub>-based devices and systems remain great at integrated circuits as well as the internet of things. Indeed, the 2D materials have been incorporated in the logic gate-based digital circuits, programmable memories, and RF integrated circuits. One can refer to the graphene [124] and transition-metal dichalcogenides [131] for borrowing the concept of heterostructures. There remains a vortex of materials science research for artificial intelligence such as actuator devices, and human/machine interface. Therefore, great prospects of PdSe<sub>2</sub>-based van der Waals heterostructures are calling for the input of physicists, chemists, and materials scientists as well as industrial engineers.

**Acknowledgements** H.L. acknowledges the National Key Research and Development Program of China (2017YFB0405400) from the Ministry of Science and Technology (MOST) of China, and the Natural Science Foundation for Distinguished Young Scientist of Shandong Province (Grant No. JQ201814). We thank the Project of “20 items of University” of Jinan (2018GXRC031). W.Z thanks Taishan Scholars Project Special Funds (tsqn201812083) and NSFC (No. 52022037). The authors show their gratitude to the National Natural Science Foundation of China (NSFC grant No. 51802113, 51802116) and the Natural Science Foundation of Shandong Province, China (grant No. ZR2019BEM040, ZR2018BEM015). M.H.R. thanks the National Science Foundation China (NSFC, Project 52071225), the National Science Center and the Czech Republic under the ERDF program “Institute of Environmental Technology—Excellent Research” (No. CZ.02.1.01/0.0/0.0/16\_019/0000853) and the Sino-German Research Institute for support (Project No. GZ 1400).

**Open Access** This article is licensed under a Creative Commons Attribution 4.0 International License, which permits use, sharing, adaptation, distribution and reproduction in any medium or format, as long as you give appropriate credit to the original author(s) and the source, provide a link to the Creative Commons licence, and indicate if changes were made. The images or other third party material in this article are included in the article’s Creative Commons licence, unless indicated otherwise in a credit line to the material. If material is not included in the article’s Creative Commons licence and your intended use is not permitted by statutory regulation or exceeds the permitted use, you will need to obtain permission directly from the copyright holder. To view a copy of this licence, visit <http://creativecommons.org/licenses/by/4.0/>.

## References

1. Y. Saito, J. Ge, K. Watanabe, T. Taniguchi, A.F. Young, Independent superconductors and correlated insulators in twisted

- bilayer graphene. *Nat. Phys.* **16**(9), 926–930 (2020). <https://doi.org/10.1038/s41567-020-0928-3>
- C. Jin, J. Kim, M.I.B. Utama, E.C. Regan, H. Kleemann et al., Imaging of pure spin-valley diffusion current in  $WS_2$ - $WSe_2$  heterostructures. *Science* **360**(6391), 893–896 (2018). <https://doi.org/10.1126/science.aao3503>
  - Y. Pang, Z. Yang, Y. Yang, T.L. Ren, Wearable electronics based on 2D materials for human physiological information detection. *Small* **16**(15), 1901124 (2020). <https://doi.org/10.1002/smll.201901124>
  - A.V. Agrawal, N. Kumar, M. Kumar, Strategy and future prospects to develop room-temperature-recoverable  $NO_2$  gas sensor based on two-dimensional molybdenum disulfide. *Nano-Micro Lett.* **13**(1), 38 (2021). <https://doi.org/10.1007/s40820-020-00558-3>
  - N.E. Holden, T.B. Coplen, J.K. Böhlke, L.V. Tarbox, J. Benfield et al., IUPAC periodic table of the elements and isotopes (IPTEI) for the education community (IUPAC Technical Report). *Pure Appl. Chem.* **90**(12), 1833–2092 (2018). <https://doi.org/10.1515/pac-2015-0703>
  - K.F. Mak, J. Shan, Photonics and optoelectronics of 2D semiconductor transition metal dichalcogenides. *Nat. Photon.* **10**(4), 216–226 (2016). <https://doi.org/10.1038/nphoton.2015.282>
  - L. Zeng, S. Lin, Z. Lou, H. Yuan, H. Long et al., Ultrafast and sensitive photodetector based on a  $PtSe_2$ /silicon nanowire array heterojunction with a multiband spectral response from 200 to 1550 nm. *NPG Asia Mater.* **10**(4), 352–362 (2018). <https://doi.org/10.1038/s41427-018-0035-4>
  - R. Kempt, A. Kuc, T. Heine, Two-dimensional noble-metal chalcogenides and phosphochalcogenides. *Angew. Chem. Int. Ed.* **59**(24), 9242–9254 (2020). <https://doi.org/10.1002/anie.201914886>
  - S. Ahmad, Strain dependent tuning electronic properties of noble metal di chalcogenides  $PdX_2$  ( $X = S, Se$ ) mono-layer. *Mater. Chem. Phys.* **198**(1), 162–166 (2017). <https://doi.org/10.1016/j.matchemphys.2017.05.060>
  - L. Zeng, D. Wu, J. Jie, X. Ren, X. Hu et al., Van der Waals epitaxial growth of mosaic-like 2D platinum ditelluride layers for room-temperature mid-infrared photodetection up to 10.6 microm. *Adv. Mater.* **32**(52), 2004412 (2020). <https://doi.org/10.1002/adma.202004412>
  - Y. Zhao, J. Qiao, Z. Yu, P. Yu, K. Xu et al., High-electron-mobility and air-stable 2D layered  $PtSe_2$  FETs. *Adv. Mater.* **29**(5), 1604230 (2017). <https://doi.org/10.1002/adma.201604230>
  - H. Yang, Y. Li, Z. Yang, X. Shi, Z. Lin et al., First-principles calculations of the electronic properties of two-dimensional pentagonal structure  $XS_2$  ( $X=Ni, Pd, Pt$ ). *Vacuum* **174**(1), 109176 (2020). <https://doi.org/10.1016/j.vacuum.2020.109176>
  - D. Saraf, S. Chakraborty, A. Kshirsagar, R. Ahuja, In pursuit of bifunctional catalytic activity in  $PdS_2$  pseudo-monolayer through reaction coordinate mapping. *Nano Energy* **49**(4), 283–289 (2018). <https://doi.org/10.1016/j.nanoen.2018.04.019>
  - M. Ghorbani-Asl, A. Kuc, P. Miro, T. Heine, A single-material logical junction based on 2D Crystal  $PdS_2$ . *Adv. Mater.* **28**(5), 853–856 (2016). <https://doi.org/10.1002/adma.201504274>
  - A.D. Oyedele, S. Yang, L. Liang, A.A. Puzetzy, K. Wang et al.,  $PdSe_2$ : pentagonal two-dimensional layers with high air stability for electronics. *J. Am. Chem. Soc.* **139**(40), 14090–14097 (2017). <https://doi.org/10.1021/jacs.7b04865>
  - Y. Gu, H. Cai, J. Dong, Y. Yu, A.N. Hoffman et al., Two-dimensional palladium diselenide with strong in-plane optical anisotropy and high mobility grown by chemical vapor deposition. *Adv. Mater.* **32**(19), 1906238 (2020). <https://doi.org/10.1002/adma.201906238>
  - W.L. Chow, P. Yu, F. Liu, J. Hong, X. Wang et al., High mobility 2D palladium diselenide field-effect transistors with tunable ambipolar characteristics. *Adv. Mater.* **29**(21), 1602969 (2017). <https://doi.org/10.1002/adma.201602969>
  - A.A. Puzetzy, A.D. Oyedele, K. Xiao, A.V. Haglund, B.G. Sumpter et al., Anomalous interlayer vibrations in strongly coupled layered  $PdSe_2$ . *2D Mater.* **5**(3), 35016 (2018). <https://doi.org/10.1088/2053-1583/aabe4d>
  - Q. Liang, Q. Wang, Q. Zhang, J. Wei, S.X. Lim et al., High-performance, room temperature, ultra-broadband photodetectors based on air-stable  $PdSe_2$ . *Adv. Mater.* **31**(24), 1807609 (2019). <https://doi.org/10.1002/adma.201807609>
  - H. Yang, S.W. Kim, M. Chhowalla, Y.H. Lee, Structural and quantum-state phase transitions in van der Waals layered materials. *Nat. Phys.* **13**(10), 931–937 (2017). <https://doi.org/10.1038/nphys4188>
  - D. Wu, J. Guo, J. Du, C. Xia, L. Zeng et al., Highly polarization-sensitive, broadband, self-powered photodetector based on graphene/ $PdSe_2$ /germanium heterojunction. *ACS Nano* **13**(9), 9907–9917 (2019). <https://doi.org/10.1021/acsnano.9b03994>
  - K.L. Tai, J. Chen, Y. Wen, H. Park, Q. Zhang et al., Phase variations and layer epitaxy of 2D  $PdSe_2$  Grown on 2D monolayers by direct selenization of molecular Pd precursors. *ACS Nano* **14**(9), 11677–11690 (2020). <https://doi.org/10.1021/acsnano.0c04230>
  - M. Jakhar, J. Singh, A. Kumar, K. Tankeshwar, Pressure and electric field tuning of Schottky contacts in  $PdSe_2$ /ZT-MoSe<sub>2</sub> van der Waals heterostructure. *Nanotechnology* **31**(14), 145710 (2020). <https://doi.org/10.1088/1361-6528/ab5de1>
  - A.M. Afzal, M.Z. Iqbal, S. Mumtaz, I. Akhtar, Multifunctional and high-performance  $GeSe/PdSe_2$  heterostructure device with a fast photoresponse. *J. Mater. Chem. C* **8**(14), 4743–4753 (2020). <https://doi.org/10.1039/d0tc00004c>
  - D. Wu, C. Jia, F. Shi, L. Zeng, P. Lin et al., Mixed-dimensional  $PdSe_2$ /SiNWA heterostructure based photovoltaic detectors for self-driven, broadband photodetection, infrared imaging and humidity sensing. *J. Mater. Chem. A* **8**(7), 3632–3642 (2020). <https://doi.org/10.1039/c9ta13611h>



26. L.H. Zeng, Q.M. Chen, Z.X. Zhang, D. Wu, H. Yuan et al., Multilayered PdSe<sub>2</sub>/perovskite schottky junction for fast, self-powered, polarization-sensitive, broadband photodetectors, and image sensor application. *Adv. Sci.* **6**(19), 1901134 (2019). <https://doi.org/10.1002/advs.201901134>
27. J. Sun, H. Shi, T. Siegrist, D.J. Singh, Electronic, transport, and optical properties of bulk and mono-layer PdSe<sub>2</sub>. *Appl. Phys. Lett.* **107**(15), 153902 (2015). <https://doi.org/10.1063/1.4933302>
28. F. Grønvdal, E. Røst, The crystal structure of PdSe<sub>2</sub> and PdS<sub>2</sub>. *Acta Crystallogr.* **10**(4), 329–331 (1957). <https://doi.org/10.1107/s0365110x57000948>
29. J. Zhong, J. Yu, L. Cao, C. Zeng, J. Ding et al., High-performance polarization-sensitive photodetector based on a few-layered PdSe<sub>2</sub> nanosheet. *Nano Res.* **13**(6), 1780–1786 (2020). <https://doi.org/10.1007/s12274-020-2804-y>
30. Y. Zhao, J. Qiao, P. Yu, Z. Hu, Z. Lin et al., Extraordinarily strong interlayer interaction in 2D layered PtS<sub>2</sub>. *Adv. Mater.* **28**(12), 2399–2407 (2016). <https://doi.org/10.1002/adma.201504572>
31. A.V. Kuklin, H. Ågren, Quasiparticle electronic structure and optical spectra of single-layer and bilayer PdSe<sub>2</sub>: Proximity and defect-induced band gap renormalization. *Phys. Rev. B* **99**(24), 2469–9950 (2019). <https://doi.org/10.1103/PhysRevB.99.245114>
32. X. Zhao, Q. Zhao, B. Zhao, X. Dai, S. Wei et al., Electronic and optical properties of PdSe<sub>2</sub> from monolayer to trilayer. *Superlattices Microstr.* **142**(4), 106514 (2020). <https://doi.org/10.1016/j.spmi.2020.106514>
33. W. Lei, B. Cai, H. Zhou, G. Heymann, X. Tang et al., Ferroelastic lattice rotation and band-gap engineering in quasi 2D layered-structure PdSe<sub>2</sub> under uniaxial stress. *Nanoscale* **11**(25), 12317–12325 (2019). <https://doi.org/10.1039/c9nr03101d>
34. X. Zhao, B. Qiu, G. Hu, W. Yue, J. Ren et al., Spin polarization properties of pentagonal PdSe(2) induced by 3D transition-metal doping: first-principles calculations. *Materials* **11**(11), 2339 (2018). <https://doi.org/10.3390/ma11112339>
35. S.-H. Zhang, B.-G. Liu, Hole-doping-induced half-metallic ferromagnetism in a highly-air-stable PdSe<sub>2</sub> monolayer under uniaxial stress. *J. Mater. Chem. C* **6**(25), 6792–6798 (2018). <https://doi.org/10.1039/c8tc01450g>
36. S. Deng, L. Li, Y. Zhang, Strain modulated electronic, mechanical, and optical properties of the monolayer PdS<sub>2</sub>, PdSe<sub>2</sub>, and PtSe<sub>2</sub> for tunable devices. *ACS Appl. Nano Mater.* **1**(4), 1932–1939 (2018). <https://doi.org/10.1021/acsnm.8b00363>
37. G. Liu, Q.M. Zeng, P.F. Zhu, R.G. Quhe, P.F. Lu, Negative Poisson's ratio in monolayer PdSe<sub>2</sub>. *Comput. Mater. Sci.* **160**(1), 309–314 (2019). <https://doi.org/10.1016/j.commsci.2019.01.024>
38. M.A. ElGhazali, P.G. Naumov, H. Mirhosseini, V. Suss, L. Muchler et al., Pressure-induced superconductivity up to 13.1 K in the pyrite phase of palladium diselenide PdSe<sub>2</sub>. *Phys. Rev. B* **96**(6), 060509 (2017). <https://doi.org/10.1103/PhysRevB.96.060509>
39. J. Yu, X. Kuang, Y. Gao, Y. Wang, K. Chen et al., Direct observation of the linear dichroism transition in two-dimensional palladium diselenide. *Nano Lett.* **20**(2), 1172–1182 (2020). <https://doi.org/10.1021/acs.nanolett.9b04598>
40. W. Lei, S. Zhang, G. Heymann, X. Tang, J. Wen et al., A new 2D high-pressure phase of PdSe<sub>2</sub> with high-mobility transport anisotropy for photovoltaic applications. *J. Mater. Chem. C* **7**(7), 2096–2105 (2019). <https://doi.org/10.1039/c8tc06050a>
41. T.S. Walmsley, K. Andrews, T. Wang, A. Haglund, U. Rijal et al., Near-infrared optical transitions in PdSe<sub>2</sub> phototransistors. *Nanoscale* **11**(30), 14410–14416 (2019). <https://doi.org/10.1039/c9nr03505b>
42. M. Sun, J.P. Chou, L. Shi, J. Gao, A. Hu et al., Few-Layer PdSe<sub>2</sub> sheets: promising thermoelectric materials driven by high valley convergence. *ACS Omega* **3**(6), 5971–5979 (2018). <https://doi.org/10.1021/acsomega.8b00485>
43. Y. Cai, G. Zhang, Y.W. Zhang, Polarity-reversed robust carrier mobility in monolayer MoS(2) nanoribbons. *J. Am. Chem. Soc.* **136**(17), 6269–6275 (2014). <https://doi.org/10.1021/ja4109787>
44. X.-J. Ge, D. Qin, K.-L. Yao, J.-T. Lü, First-principles study of thermoelectric transport properties of monolayer gallium chalcogenides. *J. Phys. D-Appl. Phys.* **50**(40), 405301 (2017). <https://doi.org/10.1088/1361-6463/aa85b4>
45. G.D. Nguyen, L. Liang, Q. Zou, M. Fu, A.D. Oyedele et al., 3D imaging and manipulation of subsurface selenium vacancies in PdSe<sub>2</sub>. *Phys. Rev. Lett.* **121**(8), 086101 (2018). <https://doi.org/10.1103/PhysRevLett.121.086101>
46. J. Lin, S. Zuluaga, P. Yu, Z. Liu, S.T. Pantelides et al., Novel Pd<sub>2</sub>Se<sub>3</sub> two-dimensional phase driven by interlayer fusion in layered PdSe<sub>2</sub>. *Phys. Rev. Lett.* **119**(1), 016101 (2017). <https://doi.org/10.1103/PhysRevLett.119.016101>
47. J. Chen, G.H. Ryu, S. Sinha, J.H. Warner, Atomic structure and dynamics of defects and grain boundaries in 2D Pd<sub>2</sub>Se<sub>3</sub> Monolayers. *ACS Nano* **13**(7), 8256–8264 (2019). <https://doi.org/10.1021/acsnano.9b03645>
48. S. Zuluaga, J. Lin, K. Suenaga, S.T. Pantelides, Two-dimensional PdSe<sub>2</sub>-Pd<sub>2</sub>Se<sub>3</sub> junctions can serve as nanowires. *2D Mater.* **5**(3), 035025 (2018). <https://doi.org/10.1088/2053-1583/aac34c>
49. G.H. Ryu, T. Zhu, J. Chen, S. Sinha, V. Shautsova, Striated 2D lattice with sub-nm 1D etch channels by controlled thermally induced phase transformations of PdSe<sub>2</sub>. *Adv. Mater.* **31**(46), 1904251 (2019). <https://doi.org/10.1002/adma.201904251>
50. V. Shautsova, S. Sinha, L. Hou, Q. Zhang, M. Tweedie et al., Direct laser patterning and phase transformation of 2D PdSe<sub>2</sub> films for on-demand device fabrication. *ACS Nano* **13**(12), 14162–14171 (2019). <https://doi.org/10.1021/acsnano.9b06892>
51. T. Takabatake, M. Ishikawa, J.L. Jorda, Superconductivity and phase relations in the Pd-Se system. *J. Less Common Met.* **134**(1), 79–89 (1987). [https://doi.org/10.1016/0022-5088\(87\)90444-9](https://doi.org/10.1016/0022-5088(87)90444-9)
52. A.D. Oyedele, S. Yang, T. Feng, A.V. Haglund, Y. Gu et al., Defect-mediated phase transformation in anisotropic

- two-dimensional PdSe<sub>2</sub> crystals for seamless electrical contacts. *J. Am. Chem. Soc.* **141**(22), 8928–8936 (2019). <https://doi.org/10.1021/jacs.9b02593>
53. D. Wang, F. Luo, M. Lu, X. Xie, L. Huang et al., Chemical vapor transport reactions for synthesizing layered materials and their 2D counterparts. *Small* **15**(40), 1804404 (2019). <https://doi.org/10.1002/sml.201804404>
54. M. Long, Y. Wang, P. Wang, X. Zhou, H. Xia et al., Palladium diselenide long-wavelength infrared photodetector with high sensitivity and stability. *ACS Nano* **13**(2), 2511–2519 (2019). <https://doi.org/10.1021/acsnano.8b09476>
55. M. Velicky, G.E. Donnelly, W.R. Hendren, S. McFarland, D. Scullion et al., Mechanism of gold-assisted exfoliation of centimeter-sized transition-metal dichalcogenide monolayers. *ACS Nano* **12**(10), 10463–10472 (2018). <https://doi.org/10.1021/acsnano.8b06101>
56. M. Heyl, D. Burmeister, T. Schultz, S. Pallasch, G. Ligorio et al., Thermally activated gold-mediated transition metal dichalcogenide exfoliation and a unique gold-mediated transfer. *Phys. Status Solidi (RRL)* **14**(11), 2000408 (2020). <https://doi.org/10.1002/pssr.202000408>
57. S.B. Desai, S.R. Madhupathy, M. Amani, D. Kiriya, M. Hettick et al., Gold-mediated exfoliation of ultralarge optoelectronically-perfect monolayers. *Adv. Mater.* **28**(21), 4053–4058 (2016). <https://doi.org/10.1002/adma.201506171>
58. Y. Huang, Y.H. Pan, R. Yang, L.H. Bao, L. Meng et al., Universal mechanical exfoliation of large-area 2D crystals. *Nat. Commun.* **11**(1), 2453 (2020). <https://doi.org/10.1038/s41467-020-16266-w>
59. D. Zhao, S. Xie, Y. Wang, H. Zhu, L. Chen et al., Synthesis of large-scale few-layer PtS<sub>2</sub> films by chemical vapor deposition. *AIP Adv.* **9**(2), 025225 (2019). <https://doi.org/10.1063/1.5086447>
60. L. Jia, J. Wu, T. Yang, B. Jia, D.J. Moss, Large third-order optical kerr nonlinearity in nanometer-thick PdSe<sub>2</sub> 2D dichalcogenide films: implications for nonlinear photonic devices. *ACS Appl. Nano Mater.* **3**(7), 6876–6883 (2020). <https://doi.org/10.1021/acsnm.0c01239>
61. J. Zhou, J. Lin, X. Huang, Y. Zhou, Y. Chen et al., A library of atomically thin metal chalcogenides. *Nature* **556**(7701), 355–359 (2018). <https://doi.org/10.1038/s41586-018-0008-3>
62. L.H. Zeng, D. Wu, S.H. Lin, C. Xie, H.Y. Yuan et al., Controlled synthesis of 2D palladium diselenide for sensitive photodetector applications. *Adv. Funct. Mater.* **29**(1), 1806878 (2019). <https://doi.org/10.1002/adfm.201806878>
63. L.S. Lu, G.H. Chen, H.Y. Cheng, C.P. Chuu, K.C. Lu et al., Layer-dependent and in-plane anisotropic properties of low-temperature synthesized few-layer PdSe<sub>2</sub> single crystals. *ACS Nano* **14**(4), 4963–4972 (2020). <https://doi.org/10.1021/acsnano.0c01139>
64. G.D. Nguyen, A.D. Oyedele, A. Haglund, W. Ko, L. Liang et al., Atomically precise PdSe<sub>2</sub> pentagonal nanoribbons. *ACS Nano* **14**(2), 1951–1957 (2020). <https://doi.org/10.1021/acsnano.9b08390>
65. L.H. Zeng, S.H. Lin, Z.J. Li, Z.X. Zhang, T.F. Zhang et al., Fast, self-driven, air-stable, and broadband photodetector based on vertically aligned PtSe<sub>2</sub>/GaAs heterojunction. *Adv. Funct. Mater.* **28**(16), 1705970 (2018). <https://doi.org/10.1002/adfm.201705970>
66. A.N. Hoffman, Y. Gu, J. Tokash, J. Woodward, K. Xiao et al., Layer-by-layer thinning of pdse2 flakes via plasma induced oxidation and sublimation. *ACS Appl. Mater. Interfaces* **12**(6), 7345–7350 (2020). <https://doi.org/10.1021/acsnano.9b21287>
67. Q. Liang, Q. Zhang, J. Gou, T. Song, Arramel et al., Performance improvement by ozone treatment of 2D PdSe<sub>2</sub>. *ACS Nano* **14**(5), 5668–5677 (2020). <https://doi.org/10.1021/acsnano.0c00180>
68. A. Di. Bartolomeo, F. Urban, A. Pelella, A. Grillo, M. Passacantando et al., Electron irradiation of multilayer PdSe<sub>2</sub> field effect transistors. *Nanotechnology* **31**(37), 375204 (2020). <https://doi.org/10.1088/1361-6528/ab9472>
69. A. Hassan, Y. Guo, Q. Wang, Performance of the pentagonal PdSe<sub>2</sub> sheet as a channel material in contact with metal surfaces and graphene. *ACS Appl. Electron. Mater.* **2**(8), 2535–2542 (2020). <https://doi.org/10.1021/acsaelm.0c00438>
70. A. Di. Bartolomeo, A. Pelella, X. Liu, F. Miao, M. Passacantando et al., Pressure-tunable ambipolar conduction and hysteresis in thin palladium diselenide field effect transistors. *Adv. Funct. Mater.* **29**(29), 1902483 (2019). <https://doi.org/10.1002/adfm.201902483>
71. J. Gao, Y. Gao, Y. Han, J. Pang, C. Wang et al., Ultrasensitive label-free MiRNA sensing based on a flexible graphene field-effect transistor without functionalization. *ACS Appl. Electron. Mater.* **2**(4), 1090–1098 (2020). <https://doi.org/10.1021/acsaelm.0c00095>
72. A. Tankut, M. Karaman, I. Yildiz, S. Canli, R. Turan, Effect of Al vacuum annealing prior to a-Si deposition on aluminum-induced crystallization. *Phys. Status Solidi A Appl. Mater. Sci.* **212**(12), 2702–2707 (2015). <https://doi.org/10.1002/pssa.201532857>
73. T. Takenobu, T. Kanbara, N. Akima, T. Takahashi, M. Shiraishi et al., Control of carrier density by a solution method in carbon-nanotube devices. *Adv. Mater.* **17**(20), 2430–2434 (2005). <https://doi.org/10.1002/adma.200500759>
74. F. Giubileo, A. Grillo, L. Iemmo, G. Luongo, F. Urban et al., Environmental effects on transport properties of PdSe<sub>2</sub> field effect transistors. *Mater. Today Proc.* **20**(1), 50–53 (2020). <https://doi.org/10.1016/j.matpr.2019.08.226>
75. G.T. Xia, Y.N. Huang, F.J. Li, L.C. Wang, J.B. Pang et al., A thermally flexible and multi-site tactile sensor for remote 3D dynamic sensing imaging. *Front. Chem. Sci. Eng.* **14**(6), 1039–1051 (2020). <https://doi.org/10.1007/s11705-019-1901-5>
76. D. Chen, Z. Liu, Y. Li, D. Sun, X. Liu et al., Unsymmetrical alveolate PMMA/MWCNT film as a piezoresistive E-skin with four-dimensional resolution and application for detecting motion direction and airflow rate. *ACS Appl. Mater. Interfaces* **12**(27), 30896–30904 (2020). <https://doi.org/10.1021/acsnano.0c02640>
77. Y. Zhou, Y. Wang, K. Wang, L. Kang, F. Peng et al., Hybrid genetic algorithm method for efficient and robust evaluation



- of remaining useful life of supercapacitors. *Appl. Energy* **260**(1), 114169 (2020). <https://doi.org/10.1016/j.apenergy.2019.114169>
78. X. Shang, S. Li, K. Wang, X. Teng, X. Wang et al., MnSe<sub>2</sub>/Se composite nanobelts as an improved performance anode for lithium storage. *Int. J. Electrochem. Sci.* **14**(1), 6000–6008 (2019). <https://doi.org/10.20964/2019.07.37>
79. C. Bu, F. Li, K. Yin, J. Pang, L. Wang et al., Research progress and prospect of triboelectric nanogenerators as self-powered human body sensors. *ACS Appl. Electron. Mater.* **2**(4), 863–878 (2020). <https://doi.org/10.1021/acsaem.0c00022>
80. S.C. Dhanabalan, J.S. Ponraj, H. Zhang, Q. Bao, Present perspectives of broadband photodetectors based on nanobelts, nanoribbons, nanosheets and the emerging 2D materials. *Nanoscale* **8**(12), 6410–6434 (2016). <https://doi.org/10.1039/c5nr09111j>
81. A. Di. Bartolomeo, A. Pelella, F. Urban, A. Grillo, L. Lemmo et al., Field emission in ultrathin PdSe<sub>2</sub> back-gated transistors. *Adv. Electron. Mater.* **6**(7), 2000094 (2020). <https://doi.org/10.1002/aelm.202000094>
82. R. Zhuo, L. Zeng, H. Yuan, D. Wu, Y. Wang et al., In-situ fabrication of PtSe<sub>2</sub>/GaN heterojunction for self-powered deep ultraviolet photodetector with ultrahigh current on/off ratio and detectivity. *Nano Res.* **12**(1), 183–189 (2018). <https://doi.org/10.1007/s12274-018-2200-z>
83. M. Buscema, D.J. Groenendijk, S.I. Blanter, G.A. Steele, H.S. van der Zant et al., Fast and broadband photoresponse of few-layer black phosphorus field-effect transistors. *Nano Lett.* **14**(6), 3347–3352 (2014). <https://doi.org/10.1021/nl5008085>
84. X. Wan, Y. Xu, H. Guo, K. Shehzad, A. Ali et al., A self-powered high-performance graphene/silicon ultraviolet photodetector with ultra-shallow junction: breaking the limit of silicon? *NPJ 2D Mater. Appl.* **1**(1), 2397–7132 (2017). <https://doi.org/10.1038/s41699-017-0008-4>
85. R. Zhuo, Y. Wang, D. Wu, Z. Lou, Z. Shi et al., High-performance self-powered deep ultraviolet photodetector based on MoS<sub>2</sub>/GaN p–n heterojunction. *J. Mater. Chem. C* **6**(2), 299–303 (2018). <https://doi.org/10.1039/c7tc04754a>
86. E.P. Mukhokosi, S.B. Krupanidhi, K.K. Nanda, Band gap engineering of hexagonal SnSe<sub>2</sub> nanostructured thin films for infra-red photodetection. *Sci. Rep.* **7**(1), 15215 (2017). <https://doi.org/10.1038/s41598-017-15519-x>
87. L.B. Luo, D. Wang, C. Xie, J.G. Hu, X.Y. Zhao et al., PdSe<sub>2</sub> multilayer on germanium nanocones array with light trapping effect for sensitive infrared photodetector and image sensing application. *Adv. Funct. Mater.* **29**(22), 1900849 (2019). <https://doi.org/10.1002/adfm.201900849>
88. Y. Yang, S.C. Liu, X. Wang, Z. Li, Y. Zhang et al., Polarization-sensitive ultraviolet photodetection of anisotropic 2D GeSe<sub>2</sub>. *Adv. Funct. Mater.* **29**(16), 1900411 (2019). <https://doi.org/10.1002/adfm.201900411>
89. F. Chu, M. Chen, Y. Wang, Y. Xie, B. Liu et al., A highly polarization sensitive antimonene photodetector with a broadband photoresponse and strong anisotropy. *J. Mater. Chem. C* **6**(10), 2509–2514 (2018). <https://doi.org/10.1039/c7tc05488b>
90. P.K. Venuthurumilli, P.D. Ye, X. Xu, Plasmonic Resonance enhanced polarization-sensitive photodetection by black phosphorus in near infrared. *ACS Nano* **12**(5), 4861–4867 (2018). <https://doi.org/10.1021/acsnano.8b01660>
91. Y. Yang, S.C. Liu, W. Yang, Z. Li, Y. Wang et al., Air-stable in-plane anisotropic GeSe<sub>2</sub> for highly polarization-sensitive photodetection in short wave region. *J. Am. Chem. Soc.* **140**(11), 4150–4156 (2018). <https://doi.org/10.1021/jacs.8b01234>
92. J. Bullock, M. Amani, J. Cho, Y.-Z. Chen, G.H. Ahn et al., Polarization-resolved black phosphorus/molybdenum disulfide mid-wave infrared photodiodes with high detectivity at room temperature. *Nat. Photon.* **12**(10), 601–607 (2018). <https://doi.org/10.1038/s41566-018-0239-8>
93. J. Du, M. Zhang, Z. Guo, J. Chen, X. Zhu et al., Phosphorene quantum dot saturable absorbers for ultrafast fiber lasers. *Sci. Rep.* **7**(1), 42357 (2017). <https://doi.org/10.1038/srep42357>
94. Y.F. Ma, S.C. Zhang, S.J. Din, X.X. Liu, X. Yu et al., Passively Q-switched Nd:GdLaNbO<sub>4</sub> laser based on 2D PdSe<sub>2</sub> nanosheet. *Opt. Laser Technol.* **124**(1), 105959 (2020). <https://doi.org/10.1016/j.optlastec.2019.105959>
95. Y.F. Ma, Z.F. Peng, S.J. Ding, H.Y. Sun, F. Peng et al., Two-dimensional WS<sub>2</sub> nanosheet based passively Q-switched Nd:GdLaNbO<sub>4</sub> laser. *Opt. Laser Technol.* **115**(1), 104–108 (2019). <https://doi.org/10.1016/j.optlastec.2019.02.015>
96. P.K. Cheng, C.Y. Tang, S. Ahmed, J. Qiao, L.H. Zeng et al., Utilization of group 10 2D TMDs-PdSe<sub>2</sub> as a nonlinear optical material for obtaining switchable laser pulse generation modes. *Nanotechnology* **32**(5), 055201 (2021). <https://doi.org/10.1088/1361-6528/abc1a2>
97. J. Pang, A. Bachmatiuk, Y. Yin, B. Trzebicka, L. Zhao et al., Applications of phosphorene and black phosphorus in energy conversion and storage devices. *Adv. Energy Mater.* **8**(8), 1702093 (2018). <https://doi.org/10.1002/aenm.201702093>
98. J. Pang, R.G. Mendes, A. Bachmatiuk, L. Zhao, H.Q. Ta et al., Applications of 2D MXenes in energy conversion and storage systems. *Chem. Soc. Rev.* **48**(1), 72–133 (2019). <https://doi.org/10.1039/c8cs00324f>
99. K. Olszowska, J. Pang, P.S. Wrobel, L. Zhao, H.Q. Ta et al., Three-dimensional nanostructured graphene: synthesis and energy, environmental and biomedical applications. *Synth. Met.* **234**(1), 53–85 (2017). <https://doi.org/10.1016/j.synthmet.2017.10.014>
100. J. Zhou, H. Chen, X. Zhang, K. Chi, Y. Cai et al., Substrate dependence on (Sb<sub>4</sub>Se<sub>6</sub>)<sub>n</sub> ribbon orientations of antimony selenide thin films: morphology, carrier transport and photovoltaic performance. *J. Alloys Compd.* **862**(1), 158703 (2021). <https://doi.org/10.1016/j.jallcom.2021.158703>
101. F. Shu, M. Wang, J. Pang, P. Yu, A free-standing superhydrophobic film for highly efficient removal of water from turbine oil. *Front. Chem. Sci. Eng.* **13**(2), 393–399 (2019). <https://doi.org/10.1007/s11705-018-1754-3>



102. K. Wang, J. Pang, L. Li, S. Zhou, Y. Li et al., Synthesis of hydrophobic carbon nanotubes/reduced graphene oxide composite films by flash light irradiation. *Front. Chem. Sci. Eng.* **12**(3), 376–382 (2018). <https://doi.org/10.1007/s11705-018-1705-z>
103. Y. Yin, J. Pang, J. Wang, X. Lu, Q. Hao et al., Graphene-activated optoplasmonic nanomembrane cavities for photo-degradation detection. *ACS Appl. Mater. Interfaces* **11**(17), 15891–15897 (2019). <https://doi.org/10.1021/acsami.9b00733>
104. F.-X. Liang, J.-Z. Wang, Z.-X. Zhang, Y.-Y. Wang, Y. Gao et al., Broadband, ultrafast, self-driven photodetector based on Cs-doped FAPbI<sub>3</sub> perovskite thin film. *Adv. Opt. Mater.* **5**(22), 1700654 (2017). <https://doi.org/10.1002/adom.20170654>
105. M. Long, A. Gao, P. Wang, H. Xia, C. Ott et al., Room temperature high-detectivity mid-infrared photodetectors based on black arsenic phosphorus. *Sci. Adv.* **3**(6), e1700589 (2017). <https://doi.org/10.1126/sciadv.1700589>
106. X. Yu, P. Yu, D. Wu, B. Singh, Q. Zeng et al., Atomically thin noble metal dichalcogenide: a broadband mid-infrared semiconductor. *Nat. Commun.* **9**(1), 1545 (2018). <https://doi.org/10.1038/s41467-018-03935-0>
107. A.L. Hsu, P.K. Herring, N.M. Gabor, S. Ha, Y.C. Shin et al., Graphene-based thermopile for thermal imaging applications. *Nano Lett.* **15**(11), 7211–7216 (2015). <https://doi.org/10.1021/acs.nanolett.5b01755>
108. J. Piotrowski, A. Rogalski, Uncooled long wavelength infrared photon detectors. *Infrared Phys. Technol.* **46**(1–2), 115–131 (2004). <https://doi.org/10.1016/j.infrared.2004.03.016>
109. Y. Cao, X. Zhu, H. Chen, X. Zhang, J. Zhou et al., Towards high efficiency inverted Sb<sub>2</sub>Se<sub>3</sub> thin film solar cells. *Sol. Energy Mater. Sol. Cells* **200**(1), 109945 (2019). <https://doi.org/10.1016/j.solmat.2019.109945>
110. Y. Cao, X. Zhu, J. Jiang, C. Liu, J. Zhou et al., Rotational design of charge carrier transport layers for optimal antimony trisulfide solar cells and its integration in tandem devices. *Sol. Energy Mater. Sol. Cells* **206**(1), 110279 (2020). <https://doi.org/10.1016/j.solmat.2019.110279>
111. J. Jiang, F. Meng, Q. Cheng, A. Wang, Y. Chen et al., Low lattice mismatch InSe–Se vertical van der Waals heterostructure for high-performance transistors via strong fermi-level depinning. *Small Methods* **4**(8), 2000238 (2020). <https://doi.org/10.1002/smt.202000238>
112. J. Jiang, F. Meng, Q. Cheng, A. Wang, Y. Chen et al., Low lattice mismatch InSe–Se vertical van der Waals heterostructure for high-performance transistors via strong fermi-level depinning (Small Methods 8/2020). *Small Methods* **4**(8), 2070032 (2020). <https://doi.org/10.1002/smt.202070032>
113. C.-C. Wu, D. Jariwala, V.K. Sangwan, T.J. Marks, M.C. Hersam et al., Elucidating the photoresponse of ultrathin MoS<sub>2</sub> field-effect transistors by scanning photocurrent microscopy. *J. Phys. Chem. Lett.* **4**(15), 2508–2513 (2013). <https://doi.org/10.1021/jz401199x>
114. F. Xue, L. Chen, J. Chen, J. Liu, L. Wang et al., p-Type MoS<sub>2</sub> and n-type ZnO diode and its performance enhancement by the piezophototronic effect. *Adv. Mater.* **28**(17), 3391–3398 (2016). <https://doi.org/10.1002/adma.201506472>
115. D. Li, M. Chen, Z. Sun, P. Yu, Z. Liu et al., Two-dimensional non-volatile programmable p–n junctions. *Nat. Nanotechnol.* **12**(9), 901–906 (2017). <https://doi.org/10.1038/nnano.2017.104>
116. X. Zhang, J. Grajal, J.L. Vazquez-Roy, U. Radhakrishna, X. Wang et al., Two-dimensional MoS<sub>2</sub>-enabled flexible rectenna for Wi-Fi-band wireless energy harvesting. *Nature* **566**(7744), 368–372 (2019). <https://doi.org/10.1038/s41586-019-0892-1>
117. A.M. Afzal, G. Dastgeer, M.Z. Iqbal, P. Gautam, M.M. Faisal, High-performance p-BP/n-PdSe<sub>2</sub> near-infrared photodiodes with a fast and gate-tunable photoresponse. *ACS Appl. Mater. Interfaces* **12**(17), 19625–19634 (2020). <https://doi.org/10.1021/acsami.9b22898>
118. J.A. Leñero-Bardallo, R. Carmona-Galán, A. Rodríguez-Vázquez, Applications of event-based image sensors—review and analysis. *Int. J. Circ. Theor. Appl.* **46**(9), 1620–1630 (2018). <https://doi.org/10.1002/cta.2546>
119. F.X. Liang, X.Y. Zhao, J.J. Jiang, J.G. Hu, W.Q. Xie et al., Light confinement effect induced highly sensitive, self-driven near-infrared photodetector and image sensor based on multilayer PdSe<sub>2</sub>/pyramid Si heterojunction. *Small* **15**(44), 1903831 (2019). <https://doi.org/10.1002/sml.201903831>
120. I. Ibrahim, J. Kalbacova, V. Engemaier, J.B. Pang, R.D. Rodriguez et al., Confirming the dual role of etchants during the enrichment of semiconducting single wall carbon nanotubes by chemical vapor deposition. *Chem. Mater.* **27**(17), 5964–5973 (2015). <https://doi.org/10.1021/acs.chemmater.5b02037>
121. J. Pang, R.G. Mendes, P.S. Wrobel, M.D. Wlodarski, H.Q. Ta et al., Self-terminating confinement approach for large-area uniform monolayer graphene directly over Si/SiO<sub>x</sub> by chemical vapor deposition. *ACS Nano* **11**(2), 1946–1956 (2017). <https://doi.org/10.1021/acs.nano.6b08069>
122. J. Pang, A. Bachmatiuk, I. Ibrahim, L. Fu, D. Placha et al., CVD growth of 1D and 2D sp<sup>2</sup> carbon nanomaterials. *J. Mater. Sci.* **51**(2), 640–667 (2015). <https://doi.org/10.1007/s10853-015-9440-z>
123. A. Soni, L. Zhao, H.Q. Ta, Q. Shi, J. Pang et al., Facile graphitization of silicon nano-particles with ethanol based chemical vapor deposition. *Nano-Struct. Nano-Objects* **16**(1), 38–44 (2018). <https://doi.org/10.1016/j.nanoso.2018.04.001>
124. B. Sun, J. Pang, Q. Cheng, S. Zhang, C. Zhang et al., Synthesis of wafer-scale graphene with chemical vapor deposition for electronic device applications. *Adv. Mater. Technol.* **1**, 2000744 (2021). <https://doi.org/10.1002/admt.202000744>
125. G.S. Martynkova, F. Becerik, D. Placha, J. Pang, H. Akbulut et al., Effect of milling and annealing on carbon-silver system. *J. Nanosci. Nanotechnol.* **19**(5), 2770–2774 (2019). <https://doi.org/10.1166/jnn.2019.15869>
126. M.H. Rummeli, S. Gorantla, A. Bachmatiuk, J. Phieler, N. Geissler et al., On the role of vapor trapping for chemical vapor deposition (CVD) grown graphene over copper. *Chem. Mater.* **25**(24), 4861–4866 (2013). <https://doi.org/10.1021/cm401669k>



127. J.B. Pang, A. Bachmatiuk, L. Fu, C.L. Yan, M.Q. Zeng et al., Oxidation as a means to remove surface contaminants on Cu foil prior to graphene growth by chemical vapor deposition. *J. Phys. Chem. C* **119**(23), 13363–13368 (2015). <https://doi.org/10.1021/acs.jpcc.5b03911>
128. J.B. Pang, A. Bachmatiuk, L. Fu, R.G. Mendes, M. Libera et al., Direct synthesis of graphene from adsorbed organic solvent molecules over copper. *RSC Adv.* **5**(75), 60884–60891 (2015). <https://doi.org/10.1039/c5ra09405d>
129. N.M. Santhosh, G. Filipič, E. Kovacevic, A. Jagodar, J. Berndt et al., N-graphene nanowalls via plasma nitrogen incorporation and substitution: the experimental evidence. *Nano-Micro Lett.* **12**(1), 53 (2020). <https://doi.org/10.1007/s40820-020-0395-5>
130. R.G. Mendes, J. Pang, A. Bachmatiuk, H.Q. Ta, L. Zhao et al., Electron-driven in situ transmission electron microscopy of 2D transition metal dichalcogenides and their 2D heterostructures. *ACS Nano* **13**(2), 978–995 (2019). <https://doi.org/10.1021/acsnano.8b08079>
131. D. Zhang, T. Liu, J. Cheng, Q. Cao, G. Zheng et al., Lightweight and high-performance microwave absorber based on 2D WS<sub>2</sub>-RGO heterostructures. *Nano-Micro Lett.* **11**(1), 38 (2019). <https://doi.org/10.1007/s40820-019-0270-4>
132. K. Persson, Materials Data on PdSe<sub>2</sub> (SG:61) by Materials Project. <https://doi.org/10.17188/1199960>
133. L.-Y. Feng, R.A.B. Villaos, Z.-Q. Huang, C.-H. Hsu, F.-C. Chuang, Layer-dependent band engineering of Pd dichalcogenides: a first-principles study. *New J. Phys.* **22**(5), 053010 (2020). <https://doi.org/10.1088/1367-2630/ab7d7a>
134. K. Persson, Materials Data on PdS<sub>2</sub> (SG:61) by Materials Project. <https://doi.org/10.17188/1189716>
135. K. Persson, Materials Data on Te<sub>2</sub>Pd (SG:164) by Materials Project. <https://doi.org/10.17188/1307608>
136. G. Anemone, P. Casado Aguilar, M. Garnica, F. Calleja, A. Al Taleb et al., Electron-phonon coupling in superconducting 1T-PdTe<sub>2</sub>. *NPJ 2D Mater. Appl.* **5**(1), 25 (2021). <https://doi.org/10.1038/s41699-021-00204-5>
137. R.N. Madhu, Singh, Palladium selenides as active methanol tolerant cathode materials for direct methanol fuel cell. *Int. J. Hydrogen Energy* **36**(16), 10006–10012 (2011). <https://doi.org/10.1016/j.ijhydene.2011.05.069>
138. D. Qin, P. Yan, G. Ding, X. Ge, H. Song et al., Monolayer PdSe<sub>2</sub>: a promising two-dimensional thermoelectric material. *Sci. Rep.* **8**(1), 2764 (2018). <https://doi.org/10.1038/s41598-018-20918-9>
139. G. Zhang, M. Amani, A. Chaturvedi, C. Tan, J. Bullock et al., Optical and electrical properties of two-dimensional palladium diselenide. *Appl. Phys. Lett.* **114**(25), 253102 (2019). <https://doi.org/10.1063/1.5097825>
140. A.N. Hoffman, Y. Gu, L. Liang, J.D. Fowlkes, K. Xiao et al., Exploring the air stability of PdSe<sub>2</sub> via electrical transport measurements and defect calculations. *NPJ 2D Mater. Appl.* **3**(1), 50 (2019). <https://doi.org/10.1038/s41699-019-0132-4>
141. H. Fang, W. Hu, Photogating in low dimensional photodetectors. *Adv. Sci.* **4**(12), 1700323 (2017). <https://doi.org/10.1002/adv.201700323>
142. P. Miro, M. Ghorbani-Asl, T. Heine, Two dimensional materials beyond MoS<sub>2</sub>: noble-transition-metal dichalcogenides. *Angew. Chem. Int. Ed.* **53**(11), 3015–3018 (2014). <https://doi.org/10.1002/anie.201309280>
143. L. Li, W. Wang, Y. Chai, H. Li, M. Tian et al., Few-layered PtS<sub>2</sub> phototransistor on h-BN with high gain. *Adv. Funct. Mater.* **27**(27), 1701011 (2017). <https://doi.org/10.1002/adfm.201701011>
144. H. Xu, H.P. Huang, H. Fei, J. Feng, H.R. Fuh et al., Strategy for fabricating wafer-scale platinum disulfide. *ACS Appl. Mater. Interfaces* **11**(8), 8202–8209 (2019). <https://doi.org/10.1021/acsmi.8b19218>
145. E. Zhang, Y. Jin, X. Yuan, W. Wang, C. Zhang et al., ReS<sub>2</sub>-based field-effect transistors and photodetectors. *Adv. Funct. Mater.* **25**(26), 4076–4082 (2015). <https://doi.org/10.1002/adfm.201500969>
146. J. Shim, A. Oh, D.H. Kang, S. Oh, S.K. Jang et al., High-performance 2D rhenium disulfide (ReS<sub>2</sub>) transistors and photodetectors by oxygen plasma treatment. *Adv. Mater.* **28**(32), 6985–6992 (2016). <https://doi.org/10.1002/adma.201601002>
147. E. Zhang, P. Wang, Z. Li, H. Wang, C. Song et al., Tunable ambipolar polarization-sensitive photodetectors based on high-anisotropy ReSe<sub>2</sub> nanosheets. *ACS Nano* **10**(8), 8067–8077 (2016). <https://doi.org/10.1021/acsnano.6b04165>
148. M. Hafeez, L. Gan, H. Li, Y. Ma, T. Zhai, Chemical vapor deposition synthesis of ultrathin hexagonal ReSe<sub>2</sub> flakes for anisotropic raman property and optoelectronic application. *Adv. Mater.* **28**(37), 8296–8301 (2016). <https://doi.org/10.1002/adma.201601977>
149. W. Feng, J.-B. Wu, X. Li, W. Zheng, X. Zhou et al., Ultra-high photo-responsivity and detectivity in multilayer InSe nanosheets phototransistors with broadband response. *J. Mater. Chem. C* **3**(27), 7022–7028 (2015). <https://doi.org/10.1039/c5tc01208b>
150. M. Dai, H. Chen, R. Feng, W. Feng, Y. Hu et al., A dual-band multilayer InSe self-powered photodetector with high performance induced by surface plasmon resonance and asymmetric Schottky junction. *ACS Nano* **12**(8), 8739–8747 (2018). <https://doi.org/10.1021/acsnano.8b04931>
151. J. Ye, S. Soeda, Y. Nakamura, O. Nittono, Crystal structures and phase transformation in In<sub>2</sub>Se<sub>3</sub> compound semiconductor. *Jpn. J. Appl. Phys.* **37**, 4264–4271 (1998). <https://doi.org/10.1143/jjap.37.4264>
152. W. Feng, F. Gao, Y. Hu, M. Dai, H. Liu et al., Phase-engineering-driven enhanced electronic and optoelectronic performance of multilayer In<sub>2</sub>Se<sub>3</sub> nanosheets. *ACS Appl. Mater. Interfaces* **10**(33), 27584–27588 (2018). <https://doi.org/10.1021/acsmi.8b10194>
153. R.B. Jacobs-Gedrim, M. Shanmugam, N. Jain, C.A. Durcan, M.T. Murphy et al., Extraordinary photoresponse in two-dimensional In(2)Se(3) nanosheets. *ACS Nano* **8**(1), 514–521 (2014). <https://doi.org/10.1021/nn405037s>

154. M. Amani, E. Regan, J. Bullock, G.H. Ahn, A. Javey, Mid-wave infrared photoconductors based on black phosphorus-arsenic alloys. *ACS Nano* **11**(11), 11724–11731 (2017). <https://doi.org/10.1021/acsnano.7b07028>
155. D. Zheng, H. Fang, M. Long, F. Wu, P. Wang et al., High-performance near-infrared photodetectors based on p-type SnX (X = S, Se) nanowires grown via chemical vapor deposition. *ACS Nano* **12**(7), 7239–7245 (2018). <https://doi.org/10.1021/acsnano.8b03291>
156. G. Su, V.G. Hadjiev, P.E. Loya, J. Zhang, S. Lei et al., Chemical vapor deposition of thin crystals of layered semiconductor SnS<sub>2</sub> for fast photodetection application. *Nano Lett.* **15**(1), 506–513 (2015). <https://doi.org/10.1021/nl503857r>
157. F. Xia, T. Mueller, Y.M. Lin, A. Valdes-Garcia, P. Avouris, Ultrafast graphene photodetector. *Nat. Nanotechnol.* **4**(12), 839–843 (2009). <https://doi.org/10.1038/nnano.2009.292>
158. B.J. Kim, H. Jang, S.K. Lee, B.H. Hong, J.H. Ahn et al., High-performance flexible graphene field effect transistors with ion gel gate dielectrics. *Nano Lett.* **10**(9), 3464–3466 (2010). <https://doi.org/10.1021/nl101559n>
159. E.O. Polat, G. Mercier, I. Nikitskiy, E. Puma, T. Galan et al., Flexible graphene photodetectors for wearable fitness monitoring. *Sci. Adv.* **5**(9), eaaw7846 (2019). <https://doi.org/10.1126/sciadv.aaw7846>
160. X. Yu, Z. Dong, Y. Liu, T. Liu, J. Tao et al., A high performance, visible to mid-infrared photodetector based on graphene nanoribbons passivated with HfO<sub>2</sub>. *Nanoscale* **8**(1), 327–332 (2016). <https://doi.org/10.1039/c5nr06869j>
161. L. Zeng, L. Tao, C. Tang, B. Zhou, H. Long et al., High-responsivity UV-Vis photodetector based on transferable WS<sub>2</sub> film deposited by magnetron sputtering. *Sci. Rep.* **6**(1), 20343 (2016). <https://doi.org/10.1038/srep20343>
162. J. Jiang, Q. Zhang, A. Wang, Y. Zhang, F. Meng, C. Zhang, X. Feng, Y. Feng, L. Gu, H. Liu, L. Han, A facile and effective method for patching sulfur vacancies of WS<sub>2</sub> via nitrogen plasma treatment. *Small* **15**(36), 1901791 (2019). <https://doi.org/10.1002/sml.201901791>
163. Q. Wang, Q. Zhang, X. Zhao, Y.J. Zheng, J. Wang et al., High-energy gain upconversion in monolayer tungsten disulfide photodetectors. *Nano Lett.* **19**(8), 5595–5603 (2019). <https://doi.org/10.1021/acsnanolett.9b02136>
164. W. Zhang, M.H. Chiu, C.H. Chen, W. Chen, L.J. Li et al., Role of metal contacts in high-performance phototransistors based on WSe<sub>2</sub> monolayers. *ACS Nano* **8**(8), 8653–8661 (2014). <https://doi.org/10.1021/nn503521c>
165. H. Zhou, C. Wang, J.C. Shaw, R. Cheng, Y. Chen et al., Large area growth and electrical properties of p-type WSe<sub>2</sub> atomic layers. *Nano Lett.* **15**(1), 709–713 (2015). <https://doi.org/10.1021/nl504256y>
166. J. Chen, Q. Wang, Y. Sheng, G. Cao, P. Yang et al., High-performance WSe<sub>2</sub> photodetector based on a laser-induced p–n junction. *ACS Appl. Mater. Interfaces* **11**(46), 43330–43336 (2019). <https://doi.org/10.1021/acsnanolett.9b13948>
167. H.S. Lee, S.W. Min, Y.G. Chang, M.K. Park, T. Nam et al., MoS(2) nanosheet phototransistors with thickness-modulated optical energy gap. *Nano Lett.* **12**(7), 3695–3700 (2012). <https://doi.org/10.1021/nl301485q>
168. Y.H. Zhou, H.N. An, C. Gao, Z.Q. Zheng, B. Wang, UV–Vis–NIR photodetector based on monolayer MoS<sub>2</sub>. *Mater. Lett.* **237**(1), 298–302 (2019). <https://doi.org/10.1016/j.matlet.2018.11.112>
169. W. Wang, A. Klots, D. Prasai, Y. Yang, K.I. Bolotin et al., Hot electron-based near-infrared photodetection using bilayer MoS<sub>2</sub>. *Nano Lett.* **15**(11), 7440–7444 (2015). <https://doi.org/10.1021/acsnanolett.5b02866>
170. C. Jung, S.M. Kim, H. Moon, G. Han, J. Kwon et al., Highly crystalline CVD-grown multilayer MoSe<sub>2</sub> thin film transistor for fast photodetector. *Sci. Rep.* **5**(1), 15313 (2015). <https://doi.org/10.1038/srep15313>
171. R. Coehoorn, C. Haas, R.A. de Groot, Electronic structure of MoSe<sub>2</sub>, MoS<sub>2</sub>, and WSe<sub>2</sub>. II. The nature of the optical band gaps. *Phys. Rev. B* **35**(12), 6203–6206 (1987). <https://doi.org/10.1103/physrevb.35.6203>
172. P.J. Ko, A. Abderrahmane, N.H. Kim, A. Sandhu, High-performance near-infrared photodetector based on nano-layered MoSe<sub>2</sub>. *Semicond. Sci. Technol.* **32**(6), 065015 (2017). <https://doi.org/10.1088/1361-6641/aa6819>
173. V. Tran, R. Soklaski, Y. Liang, L. Yang, Layer-controlled band gap and anisotropic excitons in few-layer black phosphorus. *Phys. Rev. B* **89**(23), 235319 (2014). <https://doi.org/10.1103/PhysRevB.89.235319>
174. Q. Guo, A. Pospischil, M. Bhuiyan, H. Jiang, H. Tian et al., Black phosphorus mid-infrared photodetectors with high gain. *Nano Lett.* **16**(7), 4648–4655 (2016). <https://doi.org/10.1021/acsnanolett.6b01977>
175. J. Qiao, X. Kong, Z.X. Hu, F. Yang, W. Ji, High-mobility transport anisotropy and linear dichroism in few-layer black phosphorus. *Nat. Commun.* **5**(1), 4475 (2014). <https://doi.org/10.1038/ncomms5475>
176. J. Wang, A. Rousseau, E. Eizner, A.-L. Phaneuf-L'Heureux, L. Schue et al., Spectral responsivity and photoconductive gain in thin film black phosphorus photodetectors. *ACS Photon.* **6**(12), 3092–3099 (2019). <https://doi.org/10.1021/acsphtonic.9b00951>
177. X. Zhou, X. Hu, B. Jin, J. Yu, K. Liu et al., Highly anisotropic GeSe nanosheets for phototransistors with ultrahigh photoresponsivity. *Adv. Sci.* **5**(8), 1800478 (2018). <https://doi.org/10.1002/adv.201800478>
178. C. Jia, D. Wu, E.P. Wu, J.W. Guo, Z.H. Zhao et al., A self-powered high-performance photodetector based on a MoS<sub>2</sub>/GaAs heterojunction with high polarization sensitivity. *J. Mater. Chem. C* **7**(13), 3817–3821 (2019). <https://doi.org/10.1039/c8tc06398b>
179. R. Chai, Y. Chen, M. Zhong, H. Yang, F. Yan et al., Non-layered ZnSb nanoplates for room temperature infrared polarized photodetectors. *J. Mater. Chem. C* **8**(19), 6388–6395 (2020). <https://doi.org/10.1039/d0tc00755b>
180. S. Deng, M.L. Tao, J. Mei, M. Li, Y. Zhang et al., Optical and piezoelectric properties of strained orthorhombic PdS<sub>2</sub>. *IEEE Trans. Nanotechnol.* **18**(1), 358–364 (2019). <https://doi.org/10.1109/Tnano.2019.2908221>

181. Y. Deng, Z. Luo, N.J. Conrad, H. Liu, Y. Gong et al., Black phosphorus-monolayer MoS<sub>2</sub> van der Waals heterojunction p–n diode. *ACS Nano* **8**(8), 8292–8299 (2014). <https://doi.org/10.1021/nn5027388>
182. F. Yan, L. Zhao, A. Patane, P. Hu, X. Wei et al., Fast, multicolor photodetection with graphene-contacted p–GaSe/n–InSe van der Waals heterostructures. *Nanotechnology* **28**(27), 27LT01 (2017). <https://doi.org/10.1088/1361-6528/aa749e>
183. X. Chen, H. Chen, Z. Wang, Y. Shan, D.W. Zhang et al., Analysis of the relationship between the contact barrier and rectification ratio in a two-dimensional P–N heterojunction. *Semicond. Sci. Technol.* **33**(11), 114012 (2018). <https://doi.org/10.1088/1361-6641/aae3aa>
184. K. Murali, M. Dandu, S. Das, K. Majumdar, Gate-tunable WSe<sub>2</sub>/SnSe<sub>2</sub> backward diode with ultrahigh-reverse rectification ratio. *ACS Appl. Mater. Interfaces* **10**(6), 5657–5664 (2018). <https://doi.org/10.1021/acsami.7b18242>
185. M.A. Khan, S. Rathi, D. Lim, S.J. Yun, D.-H. Youn et al., Gate tunable self-biased diode based on few layered MoS<sub>2</sub> and WSe<sub>2</sub>. *Chem. Mater.* **30**(3), 1011–1016 (2018). <https://doi.org/10.1021/acs.chemmater.7b04865>
186. Z. Yang, L. Liao, F. Gong, F. Wang, Z. Wang et al., WSe<sub>2</sub>/GeSe heterojunction photodiode with giant gate tunability. *Nano Energy* **49**(1), 103–108 (2018). <https://doi.org/10.1016/j.nanoen.2018.04.034>
187. C. Lan, C. Li, S. Wang, T. He, T. Jiao et al., Zener tunneling and photoresponse of a WS<sub>2</sub>/Si van der Waals heterojunction. *ACS Appl. Mater. Interfaces* **8**(28), 18375–18382 (2016). <https://doi.org/10.1021/acsami.6b05109>
188. J. Chu, F. Wang, L. Yin, L. Lei, C. Yan et al., High-performance ultraviolet photodetector based on a few-layered 2D NiPS<sub>3</sub> nanosheet. *Adv. Funct. Mater.* **27**(32), 1701342 (2017). <https://doi.org/10.1002/adfm.201701342>
189. L. Ye, H. Li, Z. Chen, J. Xu, Near-infrared photodetector based on MoS<sub>2</sub>/black phosphorus heterojunction. *ACS Photon.* **3**(4), 692–699 (2016). <https://doi.org/10.1021/acsp Photonics.6b00079>
190. Y. Zhang, Y. Yu, L. Mi, H. Wang, Z. Zhu et al., In situ fabrication of vertical multilayered MoS<sub>2</sub>/Si homotype heterojunction for high-speed visible-near-infrared photodetectors. *Small* **12**(8), 1062–1071 (2016). <https://doi.org/10.1002/sml.201502923>
191. Q. Liu, B. Cook, M. Gong, Y. Gong, D. Ewing et al., Printable transfer-free and wafer-size MoS<sub>2</sub>/graphene van der Waals heterostructures for high-performance photodetection. *ACS Appl. Mater. Interfaces* **9**(14), 12728–12733 (2017). <https://doi.org/10.1021/acsami.7b00912>
192. A. Gundimeda, S. Krishna, N. Aggarwal, A. Sharma, N.D. Sharma et al., Fabrication of non-polar GaN based highly responsive and fast UV photodetector. *Appl. Phys. Lett.* **110**(10), 103507 (2017). <https://doi.org/10.1063/1.4978427>
193. P. Wang, S. Liu, W. Luo, H. Fang, F. Gong et al., Arrayed van der Waals broadband detectors for dual-band detection. *Adv. Mater.* **29**(16), 1521–4095 (2017). <https://doi.org/10.1002/adma.201604439>
194. D.S. Um, Y. Lee, S. Lim, J. Park, W.C. Yen et al., InGaAs nanomembrane/si van der waals heterojunction photodiodes with broadband and high photoresponsivity. *ACS Appl. Mater. Interfaces* **8**(39), 26105–26111 (2016). <https://doi.org/10.1021/acsami.6b06580>
195. W. Zheng, R. Lin, Y. Zhu, Z. Zhang, X. Ji et al., Vacuum ultraviolet photodetection in two-dimensional oxides. *ACS Appl. Mater. Interfaces* **10**(24), 20696–20702 (2018). <https://doi.org/10.1021/acsami.8b04866>
196. L.H. Zeng, M.Z. Wang, H. Hu, B. Nie, Y.Q. Yu et al., Monolayer graphene/germanium Schottky junction as high-performance self-driven infrared light photodetector. *ACS Appl. Mater. Interfaces* **5**(19), 9362–9366 (2013). <https://doi.org/10.1021/am4026505>
197. X. Li, M. Zhu, M. Du, Z. Lv, L. Zhang et al., High detectivity graphene-silicon heterojunction photodetector. *Small* **12**(5), 595–601 (2016). <https://doi.org/10.1002/sml.201502336>
198. K. Zhang, X. Fang, Y. Wang, Y. Wan, Q. Song et al., Ultra-sensitive near-infrared photodetectors based on a graphene–MoTe<sub>2</sub>–graphene vertical van der Waals heterostructure. *ACS Appl. Mater. Interfaces* **9**(6), 5392–5398 (2017). <https://doi.org/10.1021/acsami.6b14483>
199. Y.-S. Lan, X.-R. Chen, C.-E. Hu, Y. Cheng, Q.-F. Chen, Penta-PdX<sub>2</sub> (X = S, Se, Te) monolayers: promising anisotropic thermoelectric materials. *J. Mater. Chem. A* **7**(18), 11134–11142 (2019). <https://doi.org/10.1039/c9ta02138h>